Università degli Studi *Roma Tre*
Facoltà di Scienze Matematiche Fisiche e Naturali

Dottorato di Ricerca in Fisica XVI Ciclo

High Resolution Hypernuclear Spectroscopy at Jefferson Lab, Hall A

Francesco Cusanno

Coordinator

Prof. Orlando Ragnisco

Supervisor

Dr. Mauro Iodice

Tutor

Prof. Franco Garibaldi

Contents

Abstract

Experiment E94-107 at Jefferson Lab is designed to perform hypernuclear high resolution spectroscopy by electroproduction of strangeness on four 1p-shell targets: ^{12}C, ^{9}Be, ^{16}O, ^{7}Li. The hypernuclear spectroscopy provides fundamental information to understand the effective Λ-Nucleon interaction.
The first part of the experiment on ^{12}C and ^{9}Be targets has been performed in January and April-May 2004 in the experimental Hall A. The second part of the experiment (^{16}O and ^{7}Li targets) is scheduled on June 2005.
Two septum magnets and a Ring Imaging Cherenkov detector (RICH) are added to the existing apparatus, to have reasonable counting rates and excellent particle identification respectively, as required for the experiment.
A description of the apparatus, particularly of the RICH detector, and the preliminary analysis results, showing interesting information respect to the theoretical models for the studied hypernuclei, are presented here.

Chapter 1

Introduction

Hypernuclear physics is an important and exciting part of intermediate energy nuclear physics. The strange quark is an impurity in the system and the study of its propagation can reveal configurations or states not seen in other ways. The study also gives interesting important insight into the structure of ordinary nuclear matter. Just as in solid state physics, inserting a known impurity into a system allows measuring the system response to the stress imposed by that impurity. More generally, hypernuclear physics accesses information on the nature of the force between nucleons and strange baryons such as the Λ bound in the nucleus, i.e. the $\Lambda - N$ interaction.
The nucleus provides a unique laboratory for studying the $\Lambda - N$ interaction. In the past, the interaction has been partially studied by means of $\Lambda - p$ low energy scattering. Such studies yielded information only on the central part of the potential. Moreover, there is growing evidence of the hyperon importance in cosmology. Hyperons appear to be the first of strange hadrons in neutron stars, occurring at around the normal nuclear density. The onset of hyperon formation is controlled by the attractive hyperon-nucleon interaction. Most of the information on the interaction is contained in the spin dependent part, which generates doublets. These doublets are spaced apart in energy by a few keV to a few hundred keV. Hypernuclear experimental studies up to now have been carried out by hadron-induced reactions with limited energy resolution (about 2 MeV at the best). Moreover the spin flip transition excitation was limited, so, in practice, doublets have not been detected.
In the electromagnetic case, the spin flip transitions are strong, meaning that both members of doublets are populated. In addition, the reaction takes place on the proton while with hadron probes (K^- and π^-)it takes place on the neutron, so "new" hypernuclei are created. The detection of the doublets is possible provided that very good energy resolution is attained. The disadvantage of smaller electromagnetic cross sections is partially compensated by the high current, continuous, and high energy resolution capabilities of the beam at Jefferson Lab (Newport News, VA, USA).
The aim of the E94-107 experiment in Hall A at Jefferson Lab is the first "complete" study in $1p$ shell nuclei, ^7Li, ^9Be, ^{12}C, ^{16}O. Missing mass resolution as good as 400 keV (FWHM) can be attained, assuming beam energy stability of 2.5×10^{-5} ($\sigma E/E$) and the HRS momentum resolution, $\Delta p/p \simeq 10^{-4}$ (FWHM).

A large effort has been made by the collaboration and Hall A to improve the

experimental apparatus for this specific experiment.
The experimental difficulties include:

1) The cross sections are very small, dramatically decreasing with increasing scattering angles. The normal HRS minimum scattering angle is too large.

2) The states one would like to identify are very close together, requiring the best possible missing mass resolution (a few hundred keV).

3) Very high π^+ and p backgrounds are present at forward angles, implying that unambiguous kaon identification is challenging. The Hall A standard apparatus (TOF and one aerogel) is not sufficient.

To overcome these difficulties:

1,2) A change in the HRS setup was made. Two septum magnets were added enabling the detection of particles scattered at 6 degrees. Calculations and simulations have shown that the septum magnets does not degrade the HRS momentum resolution. The implementation of the septum magnets implied the modification of the optics reconstruction in the spectrometers (optics database).

3) A diffusion box type aerogel detector has been proposed, prototyped and successfully tested. Two aerogel detectors ($n = 1.015$, $n = 1.055$), of diffusion box type, have been built, successfully tested, and used by our collaboration during the E98-108.

4) Because of the very high π and proton background, this PID setup is not sufficient. A proximity focusing C_6F_{14}/CsI Ring Imaging Cherenkov detector (RICH) can provide unambiguous kaon identification. Simulation shows that one can get, in principle, a satisfactorily small p + π^+ contamination on the kaon sample (0.5 and 0.005 depending on which hypernuclear energy level produces the kaon). The detector has been built, successfully tested at CERN, transported to Jlab, and commissioned both with cosmic rays and beam, then successfully used for the hypernuclear experiment.

5) A waterfall target, used previously for other experiments in Hall A has been modified for use in these experiments with the septum magnets.

Therefore, several components are changed respect to previous experiments in Hall A. By chance, even the analysis package of the Hall A is a new tools respect to the past.
This thesis reports the major effort in improving the apparatus so as to overcome the limits described above, and the preliminary results on ^{12}C and ^{9}Be targets.
Chapter 2 introduces the strangeness electroproduction, its physics motivation and the comparison with the strangeness production with hadronic probes. Chapter 3 presents, in the framework of the strangeness electroproduction, the project of the experiment E94-107 at Jefferson Lab. Chapter 4 describes the experimental apparatus. Chapter 5 details the specific particle identification requirements of the E94-107 experiment and the improvement in the standard Hall A setup to match these requirements. Chapter 6 describes the data analysis.

In the first part of my PhD work I contributed to the project of the particle identification and particularly of the RICH project and analysis code [21].
Later I contributed to the RICH commissioning and fine tuning of electronics and Multi Wire Proportional Chamber operational setup [22].
Furthermore, I participated to design and to build, in collaboration with Dr. Herbert

Breuer, the Quantum Efficiency measurement system for the RICH photodetector. I tested and used it, for the first time on large area photocathodes, for checking the "quality" of the photodetectors, by mapping out the Quantum-Efficiency just after the CsI deposition, before the installation of the photocathodes into the RICH [20].
After the data taking, I significantly contributed to the analysis of the data.

Chapter 2

Strangeness Electroproduction

2.1 Strangeness Electroproduction

K mesons were 'discovered' in the first half of the 20^{th} century (Rochester and Butler, 1947, claiming the first observation [1]). What was observed initially was a previously unknown particle produced in strong interactions but which showed a rather long lifetime (on the order of 10^{-8} s), characteristic of weak decays. To (partially) explain the properties of these particles, a new quantum number, strangeness, S, was proposed by Gell Mann and Nishijma. Strangeness is conserved in the strong and electromagnetic interations, but not in the weak interactions. Conventionally the K^+ meson (and, for that matter, the Λ hyperon) has strangeness of -1. Later on Gell Mann and Zweig proposed the quark model, in what turned out to be an important contribution to the advance of nuclear/particle physics.
In the quarks and gluons language of QCD one can describe the K meson as the lightest quark-antiquark system in which a strange quark, s, is paired with an up, u, or down, d, quark.
After the discovery in the forties, strangeness physics was a very active field of study for about two decades. Despite some early successes, the field of electromagnetic production of strangeness was gradually abandoned in the mid-late 1970s, mainly due to a lack of adequate experimental facilities and an apparently complicated reaction mechanism [2]. As a direct consequence of this lack of activity in the field, the experimental data until the end of the 1990s was very scarce and, for the most part, plagued by large statistical and systematic uncertainties.
In recent years, a new plethora of theoretical studies of electroproduction (and photoproduction as well) emerged, fuelled by the promise of understanding hadrons in terms of QCD and the construction of new accelerators capable of providing continuous wave, high-current, electron beams in the few GeV range.
As Jefferson Lab (CEBAF at that time) became operational in 1994 and started its physics program in late 1995, this promise of a new generation of electron accelerators turned into palpable reality. Among the first experiments to take data at this new facility were two kaon electroproduction experiments, E91-016 and E93-018. In 2001 and 2002 another kaon electroproduction experiment, E98-108, has taken data [3].

2.2 Elementary electroproduction of strangeness

The elementary process in the electroproduction of strangeness is $e+p \longrightarrow e'+K^{+}+\Lambda$. The exclusive cross section of the process is

$$\frac{d^5\sigma}{dE'_e d\Omega_e d\Omega_K} = \Gamma \frac{d\sigma}{d\Omega_K} \tag{2.1}$$

where $d\sigma/d\Omega_K$ is the cross section of the virtual photoproduction $\gamma_v + p \longrightarrow K + \Lambda$ and Γ is the virtual photon flux:

$$\Gamma = \frac{\alpha}{2\pi^2}\frac{E'}{E}\frac{E_\gamma}{Q^2}\frac{1}{1-\varepsilon} \tag{2.2}$$

where $Q^2 = -(e-e')^2 = -(\omega, \overrightarrow{q})^2$ is the momentum transfer. The transverse polarization of the virtual photon ε is:

$$\varepsilon = \frac{1}{1+\frac{2|\vec{q}|^2}{Q^2}\tan^2\frac{\theta_e}{2}} \tag{2.3}$$

and the longitudinal polarization is:

$$\varepsilon_{_L} = \frac{Q^2}{\omega^2}\varepsilon \tag{2.4}$$

It is possible to write the cross section as function of Φ, the angle between the diffusion plane and the reaction one.

$$\frac{d\sigma}{d\Omega_K} = \frac{d\sigma_{_T}}{d\Omega_K} + \varepsilon_{_L}\frac{d\sigma_{_L}}{d\Omega_K} + \varepsilon\frac{d\sigma_{_{TT}}}{d\Omega_K}cos(2\Phi) + \sqrt{2\varepsilon_{_L}(1+\varepsilon)}\frac{d\sigma_{_{LT}}}{d\Omega_K}cos\Phi \tag{2.5}$$

With some algebra is possible to write:

$$\begin{aligned}\frac{d^5\sigma}{dE'_e d\Omega_e d\Omega_K} &= \Gamma\left[\frac{d\sigma_{_T}}{d\Omega_K} + \varepsilon_L\frac{d\sigma_{_L}}{d\Omega_K} + \varepsilon\frac{d\sigma_{_{TT}}}{d\Omega_K}cos(2\Phi)\right] + \\ &+\Gamma\left[\sqrt{2\varepsilon_L(1+\varepsilon)}\frac{d\sigma_{_{LT}}}{d\Omega_K}cos\Phi\right]\end{aligned} \tag{2.6}$$

The explicit expression of each terms depends on the physics models describing the process.
There are several approaches for treating elementary process of electromagnetic production (photo- or electroproduction) of strangeness [4]:[10]. Some of them are appropriate for higher energies (photon energy greater then 4 GeV): the Regge model or, for threshold region, the chiral perturbation theory. However, for use in a more complex calculation, such as the photoproduction or electroproduction of hypernuclei, the so-called isobaric models, utilizing only the hadronic degrees of freedom, are the most suitable. Such models are based on the effective hadronic Lagrangian and the amplitude of the process contains the contribution of simple Born terms and from the exchange of different nucleon resonance (s-channel contributions), meson resonances

(t-channel) and hyperon resonances (u-channel). Unfortunately, the case of the electromagnetic production of kaons is much more complicated than the electromagnetic production of pions. In the pion case one knows that the Δ_{33} resonance plays a dominant role at least at small and intermediate energies and one can build on effective theory starting from simple model with only one nucleon resonance - just Δ_{33}. In the kaon case there is no such dominant resonance and one has to include from the very beginning a large number of nucleon, meson and hyperon resonances with mass as large as 2 GeV. This means that it is possible to construct many different models of this type with different content of such resonances. Main coupling constants of the model can be constrained adopting SU(3) symmetry but many other couplings have to be simply fitted to obtain good agreement with available experimental data.

Due to this situation many models of this type were constructed and published starting from 70's with different sets of resonances and different values of coupling constants. As a rule these models include only nucleon spin 1/2 resonances. However, SAPHIR data collected a few years ago show clear resonant behaviour of the photoproduction cross section at photon energy ~ 1.5 GeV and none of these older models were able to explain this phenomenon. Bennhold and collaborators then suggested that to explain this resonant behaviour one has to include into the model "missing" D_{13} resonance with a mass of ~ 1700 MeV, predicted by some quark models but not yet discovered in hadron reactions. The presence of this resonance is the main difference of their K-MAID model from other models. The necessity to include this resonance into the model was shown also by P. Bydzovsky [17] based on very recent (2004) SAPHIR and CLAS data. It seems, that the inclusion of this resonance has rather strong influence on the behaviour of the cross section of the elementary process at very forward kaon scattering angles (the presence of the dip) especially at higher photon energies. Of course this will also influence the predicted hypernuclear production rates.

2.3 Hypernuclei

The hypernucleus is a nucleus composed of nucleons (protons and neutrons) and one or more hyperons bound to its core. Since all hyperons decay via the strong interaction except the Λ hyperon which decays weakly, only the Λ lives relatively long enough to form a particle-stable system. The Λ is weakly coupled to the nuclear core, and the shell model [24] can be used to describe this system. In this model the Λ resides in the 1s shell in the hypernuclear ground state. Excited states are obtained by promoting a Λ to higher orbits or coupling a Λ in the ground state to an excited nuclear core. The shell model is a precise and predictive tool used to describe nuclear spectra. Based on the experimental knowledge of some light hypernuclei, scattering data of hyperons from nucleons, and flavor SU(3) symmetry, an effective ΛN interaction for the shell model can be constructed [31].
Generally, the two body ΛN interaction can be expressed in terms of five parts [32]:

$$V_{\Lambda N}(r) = V_0(r) + V_\Delta(r)\overrightarrow{s_N}\cdot\overrightarrow{s_\Lambda} + V_\Lambda(r)\overrightarrow{s_\Lambda}\cdot\overrightarrow{l_{N\Lambda}} + V_N(r)\overrightarrow{s_N}\cdot\overrightarrow{l_{N\Lambda}} + V_T(r)S_{12} \qquad (2.7)$$

where, by integration on the radial variable:

$V_0 = \int V_0(r)dr$ is the central radial integral,

$\Delta = \int V_\Delta(r)dr$ is the spin-spin radial integral and $\overrightarrow{s_N}$,$\overrightarrow{s_\Lambda}$ is the spin for Λ and nucleon,

$s_\Lambda = \int V_\Lambda(r)dr$ is the Λ spin orbit radial integral and $l_{N\Lambda}$ is the relative orbital angular momentum,

$s_N = \int V_N(r)dr$ is the N spin orbit radial integral,

$T = \int V_T(r)dr$ is the tensor radial integral and $S_{12} = 3(\widehat{\sigma_N} \cdot \widehat{r})(\widehat{\sigma_\Lambda} \cdot \widehat{r}) - \widehat{\sigma_\Lambda} \cdot \widehat{r}$ with $\widehat{r} = |\widehat{r_N} - \widehat{r_\Lambda}|$ and $\widehat{\sigma_{\Lambda,N}}$ are the Pauli matrices.

When a Λ, as an example, couples to a nuclear state of spin (J) and isospin (T), a doublet of states $J = J^{A-1} \pm 1/2$ is formed. The doublet splitting is determined by the terms: Δ, s_Λ and T, while s_N contributes to the spacing between the doublets. The parameters (Δ, s_Λ, T , and s_N) are determined experimentally from the structure information of Λ hypernuclei.
It is evident that the most important part of the interaction lies in the spin-spin and spin-orbit terms.
Several set of parameters Δ, s_Λ, T , and s_N (model 'Canonical' [36], 'Standard' [32], 'FMZE' [33], 'YNG' [34]) have been used for fitting the data. An example of levels predicted for the hypernucleus ${}^9Li_\Lambda$ by different models is shown in fig. 2.1. The predicted doublet splittings are different. One model ('YNG', effective interaction with gaussian parametrizations) predicts a doublet splitting detectable, in principle, provided an energy resolution of few hundreds keV.
The ΛN interaction is much weaker than the NN interaction. Unlike the NN interaction, an isovector boson (π) exchange is not allowed in the ΛN interaction because the Λ has an isospin I=0 and cannot exchange, for example, a π (I=1) with a nucleon (I= 1/2), because this violates isospin conservation. Thus, to first order the ΛN interaction is mediated by two-pion exchange or kaon exchange.
The central ΛN interaction has no strong spin-spin and tensor contribution to its long range component, but it has a hard core comparable to that in the NN interaction.
In contrast to the nucleon spin-orbit splitting, Λ spin-orbit splitting is assumed to be very small. This small value can be explained by the quark model, in which u and d quarks in the Λ couple to zero spin so they do not contribute to the spin-orbit force. However, a larger value for Λ spin-orbit splitting is predicted by other models like the one-boson-exchange model.
Generally, several experiments are still required to completely define the ΛN interaction. The E94-107 experiment in Hall A at Jefferson Lab plan to realize a first 'systematics' of $1p$ shell hypernuclei by electroproduction of strangeness.

2.3.1 Hypernucleus Production

A variety of reactions can be used to produce hypernuclei. Each of these reactions has its own characteristics, which selectively populate Λ hypernuclear states. They can be divided into two categories: strangeness exchange and associated production. Most hypernuclear information has been obtained from (K^-, π^-) and (π^+, K^+) reactions.

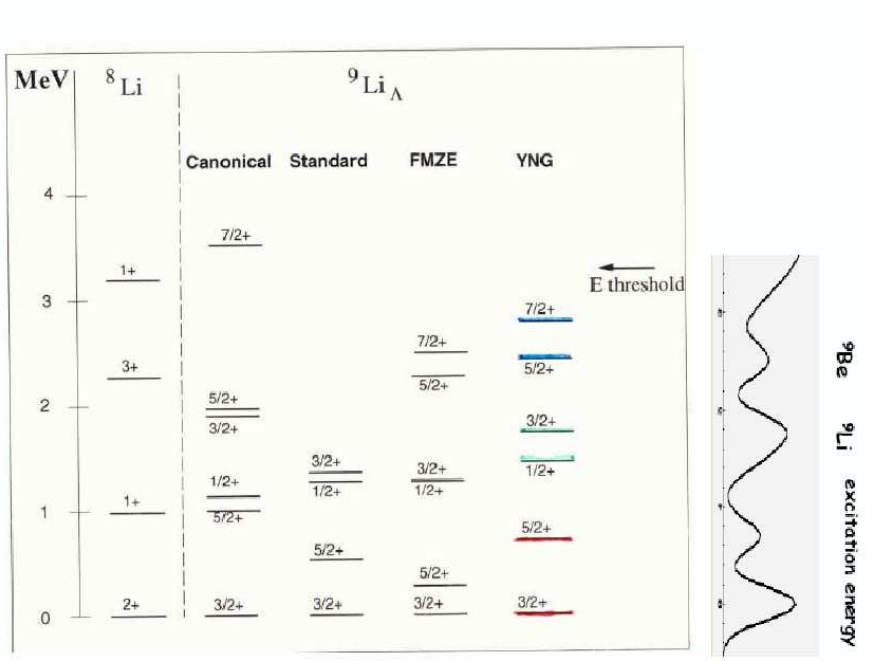

Figure 2.1: Predicted energy levels for ${}^{9}Li_{\Lambda}$ using different models for ΛN interaction.

Both (K^-, π^-) and (π^+, K^+) involve the elementary transition $n \rightarrow \Lambda$ and excite only natural parity states. The (K^-, π^-) excites low spin states at forward angles due to the small momentum transfer while the (π^+, K^+) excites high spin states due to high momentum transfer [11].
In contrast to the previous two reactions, the reaction $(e, e'K^+)$ involves the elementary transition $p \rightarrow \Lambda$ and can excite both natural and unnatural parity (spin-flip) hypernuclear states with comparable strength. Similar to the (π^+, K^+) reaction, $(e, e'K^+)$ excites high-spin, bound hypernuclear states. Contrary to the other two hadronic interactions which use a secondary beam, a primary beam with extremely good beam emittance is used in the $(e, e'K^+)$ reaction which can provide much better energy resolution. Also, electron beams are very clean and well controlled.
In the reaction (K^-, π^-), both the K^- and π^- particles are strongly absorbed (the $\overline{u}$-quark in both $K^-(\overline{u}s)$ and $\pi^-(\overline{u}d)$ can easily annihilate with a valence quark u in the nucleon (udd or uud) to form a three quark resonance) in the nuclear medium which complicates the reaction mechanism. Also, the initial state particle π^+, in the reaction (π^+, K^+), is strongly absorbed (the $\overline{d}$-quark in $\pi^+(u\overline{d})$ can also easily annihilate with a valance quark d in the nucleon to form three quark resonance) in the nucleus. On the other hand, both electron and K^+ interact weakly (the u quark in the K^+ can only annihilate with a sea quark) in the nucleus, which leads to only a small distortion in the process $(e, e'K^+)$, making the theoretical analysis less complicated and more reliable. Due to the weak interaction of the electron and K^+ in the nucleus, the possibility of deeply bound hypernuclear states increases.
The disadvantage of the $(e, e'K^+)$ reaction is that it has a smaller cross section.

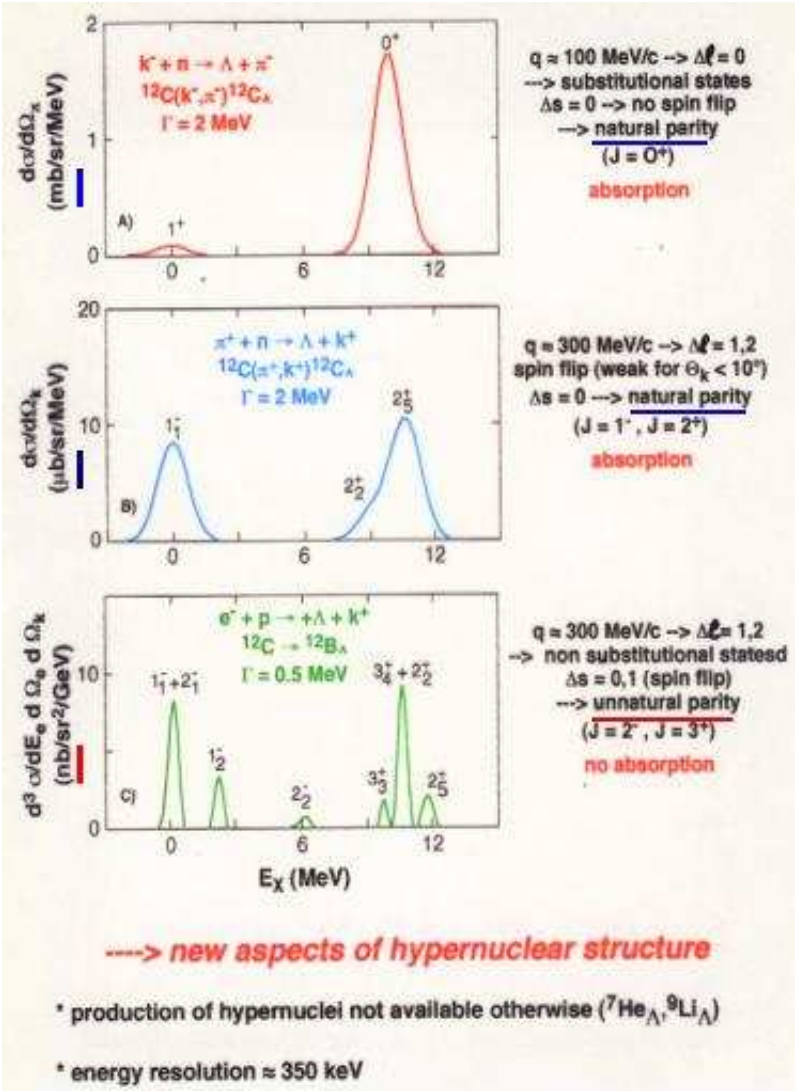

Figure 2.2: Comparison between hadronic probes and electromagnetic probes.

In the (K^-, π^-) reaction, which is exothermic, it is possible to reach zero momentum transfer, whereas this is not the case in the $(e, e'K^+)$ reaction.
The reaction $(e, e'K^+)$ includes the elementary process,

$$\gamma p \rightarrow K^+ \Lambda \tag{2.8}$$

where the photon is produced virtually by the (e,e') reaction. The photon is virtual in the sense that its 3-momentum, $\overline{q}$, and energy, ω, are independent and are absorbed by the same nucleus.
The $(e, e'K^+)$ reaction gives minimal momentum transfers to the hypernucleus when the angle between the virtual photon and the K^+ is zero. The minimum momentum transfer can be obtained at forward angles.
Fig. 2.2 shows the complementarity of different probes: different states are excited, different energy resolutions can be obtained. The advantages of the electromagnetic probe is evident: much better energy resolution. Fig. 2.3 shows the effect of energy resolution on $^9Li_\Lambda$ missing energy spectrum: only with an energy resolution of 500 keV

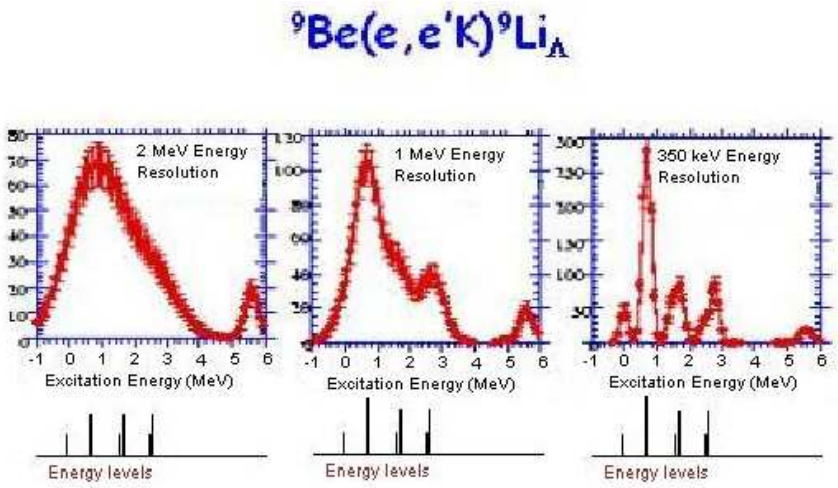

Figure 2.3: Simulated spectrum of the $^9Li_\Lambda$ for different values of of the resolution. With a resolution ¡ 500 keV doublet splitting should be detected.

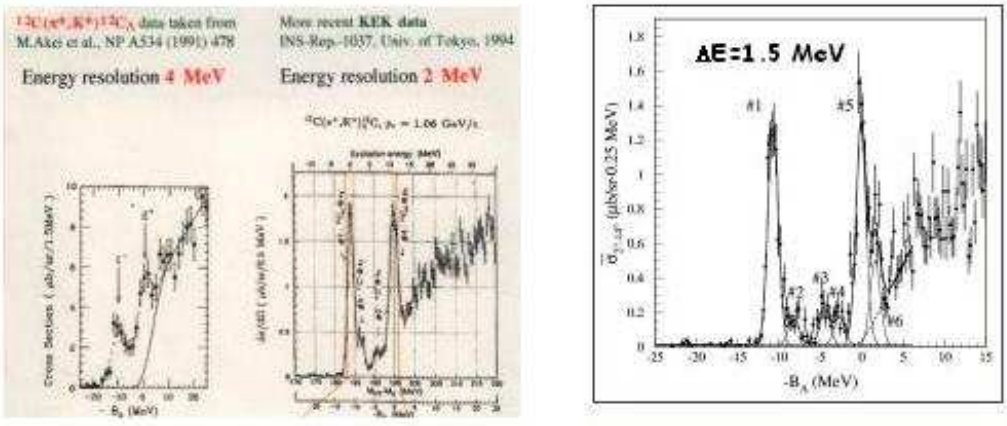

Figure 2.4: The $^{12}C_\Lambda$ spectrum at different values of the resolution.

or less it is possible to identify the first doublet. Fig. 2.4 shows the effect of improved energy resolution on ${}^{12}C_\Lambda$: two, three, or four peaks are detected in the core excited part of the spectrum, when the energy resolution improves from 4 MeV [12] to 2 MeV, to 1.5 MeV [13].

2.3.2 Experimental History

The earliest hypernuclear studies involved K^- absorption at rest in bubble chambers [14]. More systematic studies started with the availability of higher intensity separated kaon beams. The majority of these hypernuclear studies were carried out through the strangeness exchange, (K^-, π^-), and the associated, (π^+, K^+), reactions at CERN, BNL, and KEK. The CERN experiments started in the 1970's and the BNL experiments in early 1980's. The KEK experiments followed a few years later.
In 1972 the existence of a particle-unstable state in the $p_{3/2}$ shell was confirmed and led to the first hypernuclear spectroscopy experiments at CERN in 1973. In an experiment at the BNL Alternating Gradient Synchrotron (AGS), transitions in both ${}^{7}_{\Lambda}Li$ and ${}^{9}_{\Lambda}Be$ were established for the first time in hypernuclei produced by the (K^-, π^-) reaction. In 1984 at BNL, the (π^+, K^+) reaction succeeded in exciting non-substitutional, stretched states of ${}^{12}_{\Lambda}C$.
This work stimulated scientists at BNL to extend the (π^+, K^+) studies up to the mass systems $A \simeq 9 - 89$, ${}^{89}Y$, to determine the binding energies of the single particle states of a Λ in a nucleus. In 1987 scientists at KEK, were able to use a 650 MeV/c Kaon beam to study the $(K^-_{stopped}, \pi^-)$ reaction. The KEK experiments also extended the (π^+, K^+) studies in E336 which provided high-quality excitation spectra with $1.9 - 2.5$ MeV (FWHM) resolution and high statistics for ${}^{7}_{\Lambda}Li$, ${}^{9}_{\Lambda}Be$, ${}^{12}_{\Lambda}C$, ${}^{13}_{\Lambda}C$, and ${}^{16}_{\Lambda}O$.
E336 was followed by E369. The E369 experiment measured the spectra of ${}^{89}_{\Lambda}Y$ and ${}^{51}_{\Lambda}V$, as well as ${}^{12}_{\Lambda}C$ with high statistics and improved resolutions of 1.4 - 1.7 MeV/c (FWHM). The energy resolution of 1.5 MeV (FWHM) for ${}^{12}_{\Lambda}C$ is shown in Fig. 2.4.
Another experiment at KEK studied the (π^+, K^+) reaction, E419. This experiment used a germanium (Ge) detector, Hyperball, for studying spectroscopy. From these ray energies and their yields, several ${}^{7}_{\Lambda}Li$ levels were determined with high precision.
In a 1997 experiment, E907 at BNL AGS, carried out a study of the reaction ${}^{12}C(K^-_{stopped}, \pi^0){}^{12}_{\Lambda}B$, where a K^- was stopped in a ${}^{12}C$ target. This is a strangeness and charge exchange reaction, and the Λ particle was produced from a proton instead of neutron. This reaction produces, in the case of a zero isospin nucleus, mirror hypernuclei to the (π^-, K^-) reaction.
The Hyperball detector, E930, aimed to determine all the ΛN interaction terms using spectroscopy in 2000-2001. It ran in 1998 and 2001.
Experiment E89-009 ran at Jefferson Lab, Hall C, in the spring of 2000, using the $(e, e'K^+)$ reaction [52]. This experiment showed the feasibility of hypernuclear spectroscopy with electron beam.

Chapter 3

E94-107 Experiment in Hall A at Jefferson Lab

The Experiment E94-107 is designed to perform high resolution hypernuclear spectroscopy on four $1p$-shell target with the electron beam at Jefferson Lab, Hall A [37]. With the previously stated advantages of the $(e, e'K^+)$ reaction, new physics can be explored. These include the following.

- A study of high resolution hypernuclear spectroscopy.
- Energy position of high-spin states of the Λ spin doublets can be determined to obtain information, in principle, on the effective ΛN interaction.
- The absolute cross section for any individual excited state can be measured providing valuable structural hypernuclear information.

We have done calculation of cross-sections for the four hypernuclei in collaboration with Miloslav Sotona (Institute of Particle and Nuclear Physics, Prague). Numerical estimates of the electroproduction cross-sections are based on the following assumptions [25]:

1- DWIA: kaon distortion is calculated in the eikonal approximation ($p_k \approx 1\ GeV/c$ kaons are weakly absorbed by nucleus) with lowest order optical potential determined by the target nucleus density and by the appropriately averaged kaon-proton and kaon-neutron forward scattering amplitude. For KN scattering, Martin parametrization [27] is used. The Fermi motion of the target protons is neglected (frozen nucleon approximation).

2- Many particle wave functions (nuclear and hypernuclear) are calculated in the full $0h\omega + 1h\omega$ shell model basis (no spurious density). The effective NN interaction of Utrecht group [26] is used, fitted to experimental energy levels and electromagnetic momenta of 1p shell nuclei. As an effective ΛN we use the reaction matrix (G matrix) derived in [34] from Nijmegen soft core hyperon-nucleon interaction (YNG residual $\Lambda - N$ interaction). It means that our ΛN residual forces contain no free parameters but Fermi momentum (nuclear density).

3- The electroproduction models based on effective Lagrangian theory with strong coupling constants fitted to available photo/electroproduction data used in DWIA. The crossing and duality constrained model by Williams, Chueng-Ryong Ji and Cotanch [28] is used as a standard choice in our calculations (it is referred to as C4 model). Other models (Bennhold-Mart K-MAID and Saclay-Lyon) are considered for comparison with data.

4 Coplanar geometry, i.e. $\Phi_K = \pi$, p_k in the (e, e') scattering plane and p_k and p_e on the opposite sides of virtual photon momentum.

5 The experimental resolution $\Gamma < 500\ keV$ is supposed for bound-state region $E < E_{thr}$ and $\Gamma = 4\ MeV$ otherwise.

3.1 The expected spectra

In our kinematical conditions virtual photons are "almost real" ($Q^2 = 0.0789\ GeV^2/c^2$).

The $^{12}B_\Lambda$ hypernucleus, produced on ^{12}C target, is extremely stable, $E_{thr} = 11.37\ MeV$. It is supposed, therefore, that some of the positive parity states ($J = 0^+$,1^+,2^+,3^+) at $E_x \sim 10 - 11\ MeV$ with (p^{-1}, p^Λ) structure may be particularly stable. The $p^\Lambda_{3/2}$ $*^{11}$ $C(J = 3/2^-, gr.\ st.)$ $J = 0^+$ state, strongly populated in (K^-, π^-) reaction at $E_x \sim 10.6\ MeV$ is not produced in $(e, e'K^+)$. An unresolved group of $J = 0^+, 2^+$ states in the same energy region was seen in (π^+, K^+) reaction on ^{12}C target. Due to the strong spin-flip, also $J = 1^+$ and especially $J = 3^+$ members of this multiplet may be populated in $(e, e'K^+)$. Taking into account the larger binding energy of the mirror $^{12}B_\Lambda$ hypernucleus, at least some of these states may be particularly stable and, if resolved, they may shed new light on the problem of Λ p-shell spin-orbit splitting.

In $^9Li_\Lambda$, produced on ^9Be target, the low-spin members of all three spin doublets (ground state and doublets built on $J = 1^+$, $E = 0.98\ MeV$ and $J = 3^+$, $E = 2.25\ MeV$ excited states of ^8Li) are rather weakly populated in comparison with the high-spin ones ($E_{thr} = 3.73\ MeV$ for neutron decay of $^9Li_\Lambda$). However, the differential cross sections are at the level of few tenths of nb/sr in all cases and the energy splitting of the first and third doublets is predicted to be reasonably large in all models ($\sim 0.2 - 0.3\ MeV$). Valuable information may also be obtained on the relative position of the different doublets (and consequently on the spin orbit parameter, s_N of ΛN interaction).
A similar situation (only one member of each doublet is strongly populated) is examined in the $^{12}B_\Lambda$ hypernucleus. In addition, the ground state doublet is nearly degenerate in all models and unresolvable with energy resolution of few hundreds keV.

In $^{16}N_\Lambda$ hypernucleus, produced on ^{16}O target and it will be studied in the extension of the E94-107 experiment scheduled on June 2005, both members of ground state (built on $J = 2^-$ ground state of ^{15}N nucleus) as well as excited state ($J = 3/2^-$,$E = 6.32\ MeV$) doublet are populated with sufficient intensity. A careful investigation

of ground state doublet can confirms or questions commonly accepted assumption of nearly degenerate $^{16}N_\Lambda$ ground state doublet. The precise measurement of the splitting of the first excited (1^-,2^-) doublet at $E_x \sim 7\ MeV$ would allow us to extract directly from experimental data extremely valuable information on the tensor component T of the ΛN interaction. It is well known [32, 33] that the tensor force T dominates the doublet splitting in the upper half of 1p-shell. Also, the precise determination of the position of strongly excited $J = 2^+$ state at $E_x \sim 11\ MeV$ may be rather interesting, as mentioned above.

The $J = 1/2^+$ ground state is strongly populated in $^7He_\Lambda$, produced on ^7Li target. The predicted production rates for the $3/2^+$ and $5/2^+$ members of the first excited doublets (built on $J = 2^+$,$E = 1.8\ MeV$ first excited state of ^6He core nucleus) are comparable but expected to be much smaller ($\sim 0.5\ nb/msr^2/GeV$). In addition, the doublet splitting predicted by standard models is much smaller ($\sim 10\ keV$) [32, 33] than in our case (YNG interaction [34]) and could not be distinguished with energy resolution of few hundreds keV. All higher hypernuclear states are unbound (neutron decay threshold $E_{thr} = 2.9\ MeV$). Nevertheless, the doublet of $^7He_\Lambda$ states $J = 3/2^-$,$J = 5/2^-$ at the excitation energy $E_x \sim 15 - 17\ MeV$ may be some interest. The underlying nuclear $J = 2^-$ level of ^6He has mainly $^{33}P_2$[33] structure and corresponding hypernuclear states should be very narrow ($\Gamma \sim 1.5\ MeV$) [35], because they lie just above the threshold of the only opened strong decay channel ($^4He^*_\Lambda + t$). The low spin partner of this doublet have been clearly seen in (K^-, π^-) as well as in (π^+, K^+) reaction.

3.2 The choice of kinematics

In order to get reasonable counting rates we have to consider the following facts:

- the electron scattering angle has to be small, to get high virtual photon flux and the kaon angle has to be close to the virtual photon direction to minimize momentum transfer (see Fig. 3.1),
- the momentum transfer to the hypernucleus in electroproduction is rather large and decreases steadily with increasing energy of the virtual photon. High energies are preferable,
- cross sections depend strongly on Q^2, measurements at low Q^2 have to be done,
- to keep reasonable kaon survival fraction the kaon momenta have to be fairly high.

The kinematics chosen is described in the Table 3.1. The cross sections and counting rates for the four nuclei are reported in Table 3.2 and 3.3. The C4 model [28] of the elementary process is used in the calculation.

The luminosity, obtained with constant beam current of 100 μA and target thickness of 100 mg/cm^2, ranges from 2.4×10^{36} to 5.4×10^{36}. The single and accidental coincidence counting rates are about constant for all the investigated nuclei and the

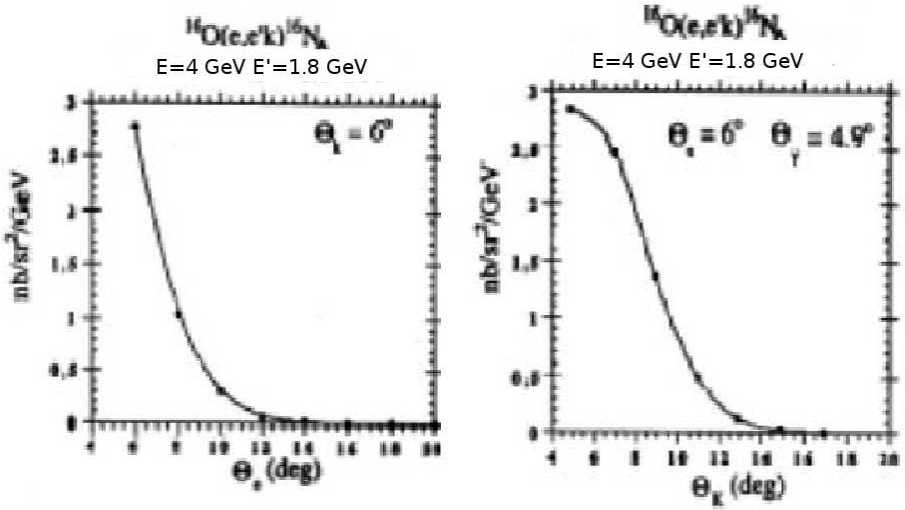

Figure 3.1: Triple differential cross section as a function of the electron scattering angles θ_e and of the kaon angle θ_K.

Incident Electron Energy	4. GeV[1].
Virtual photon energy	$\sim$ 2.2 GeV
Q^2	0.0789 GeV^2/c^2
Electron scattering angle θ_e	6°
Kaon scattering angle θ_K	6°
Kaon momentum $\|\vec{p}_K\|$	1.96 GeV/c
Electron momentum	1.86, 1.56 GeV/c

Table 3.1: The kinematics of the E94-107 Experiment.

Background	(Hz)	$^{16}O(e,e'K)^{16}N_\Lambda$			$^{9}Be(e,e'K)^{9}Li_\Lambda$		
(e,e')	$1.5 \cdot 10^5$	E	J	counts	E	J	counts
(e,π)	$2.0 \cdot 10^5$	(MeV)		(h^{-1})	(MeV)		(h^{-1})
(e,K)	$3.6 \cdot 10^3$	0	1^-	20.7	0	$3/2^+$	1.78
(e,p)	$1.8 \cdot 10^5$	0.44	0^-	1.91	0.69	$5/2^+$	9.7
(e,e'π)	$\sim 1.0 \cdot 10^2$	6.89	1^-	15	1.42	$1/2^+$	1.95
(e,e'K) (QF)	$\sim 0.1 \cdot 10^1$	7.03	2^-	39.4	1.71	$3/2^+$	2.8
(e,e'p)	$\sim 5.0 \cdot 10^1$	9.18	2^+		2.43	$5/2^+$	1.07
		10.81	2^+		2.78	$7/2^+$	3.04

Table 3.2: Expected single and random coincidence rates compared to the $^{16}O(e,e'K)^{16}N_\Lambda$ and $^{9}Be(e,e'K)^{9}Li_\Lambda$ events.

$^{12}C(e,e'K)^{12}B_\Lambda$			$^{7}Li(e,e'K)^{7}He_\Lambda$		
E (MeV)	J	counts (h^{-1})	E (MeV)	J	counts (h^{-1})
0	1^-	5.9	0	$1/2^+$	10.2
0.03	2^-	34.6	1.59	$5/2^+$	2.3
2.54	1^-	14.9	1.94	$3/2^+$	1.7
5.46	2^-	4.5	15.46	$3/2^-$	4.3
6.04	1^-	1.0	17.67	$3/2^-$	14.6
10.03	3^+	5.8			
10.63	3^+	27.1			

Table 3.3: Expected rates in the hypernuclear levels of the $^{12}C(e,e'K)^{12}B_\Lambda$ and $^{7}Li(e,e'K)^{7}He_\Lambda$ reactions.

numbers reported in Table 3.2 represent upper limits for our conditions. The single electron arm counting rates are computed with the QFS code of Lightbody and O'Connel [18] with the added contribution of the elastic radiative tail which gives electrons elastically scattered into the spectrometer after having lost the incoming energy through bremsstrahlung emission of real photons in the target. This contribution has been estimated by means of the approximated formula C.11 of [37].

Chapter 4

Experimental Setup

4.1 Overview

Jefferson Laboratory (formerly called Thomas Jefferson National Accelerator Facility, TJNAF) is located in Newport News, Virginia, USA (Fig. 4.1). The accelerator was designed to produce high current, 100% duty factor beams of up to 4 GeV to three independent and complementary experimental halls (A, B, and C). Presently the accelerator can provide a beam of up to 6 GeV and a further upgrade to 12 GeV is designed.
In Hall A, two basically identical 4 GeV/c high resolution spectrometers are used to detect scattered electrons and knocked-out hadrons [39]. The detector packages are installed on the focal plane of each spectrometer.

4.2 The Jefferson Laboratory

The electron beam is accelerated to 45 MeV in the injector before passing through a linac consisting of superconducting RF cavities where it acquires additional 400 MeV. After undergoing a 180° bend in the recirculation arc, the beam passes through another linac to gain 400 MeV more. At this point, the beam can be either extracted and directed into any of the three halls, or sent back for additional accelerations in the linacs. A total of five passes are available to each electron. In standard operation, the final beam energy is thus 45 MeV plus 800 MeV times the number of passes, up to 4045 MeV. The machine can also deliver non-standard beam with energy per pass lower than 800 MeV up to $\simeq$ 1100 MeV, reaching a final beam energy of 5645 MeV. energies (the energy per pass is different from 800 MeV).
There are five different arcs for recirculation on one end of the machine, and on the other end, there are four different arcs. The bending field of each arc is set to bend the beam of a different pass, that is, beam of different energy. The beam is separated at the end of each linac, sent to the corresponding arc, and then recombined before entering the next linac. At the end of the acceleration process, the beam is extracted and then delivered to the experimental halls.
The beam has a microstructure that consists of short pulses at a frequency of 1497 MHz.

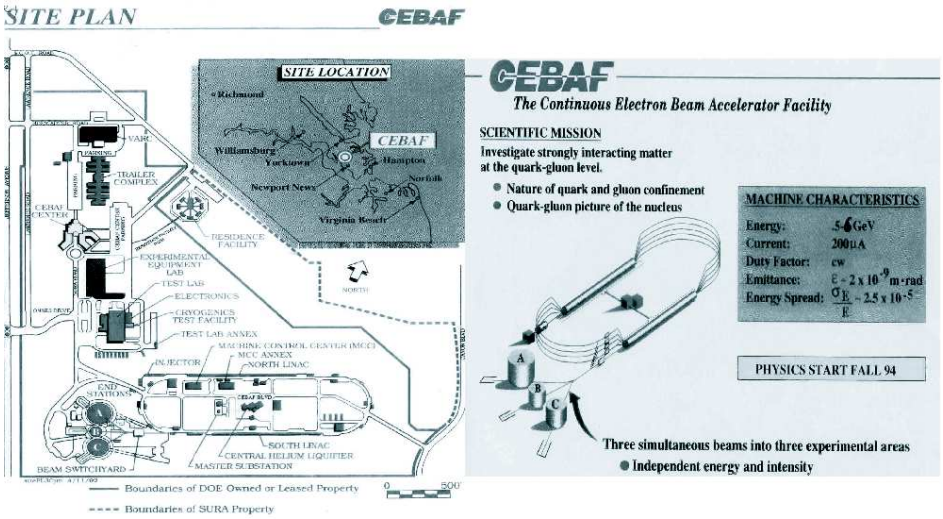

Figure 4.1: Overview of Jefferson Lab.

Generally, each hall receives one third of the pulses, resulting in a quasi-continuous train of pulses at a frequency of 499 MHz in each Hall. Beams with different energies and currents (intensities) can be delivered into the halls simultaneously.
In this experiment the two central beam energies employed are 3.96 GeV (on January 2004) and 3.77 GeV (on April-May 2004).

4.3 The Hall A

After being extracted for use in Hall A (Fig. 4.2), the electron beam is transported into the hall along the beamline, and onto the scattering chamber where the target is sitting. Along the beamline, there are two Beam Current Monitors (BMCs) and two Beam Position Monitors (BPMs) which provide precise measurements of beam current and position. The majority of the electrons incident upon the target pass through without interacting and are transported to a well-shielded beam dump. Two spectrometers are used to perform physics experiments. The electron spectrometer measures the momentum and direction of the scattered electron and similary, the hadron spectrometer detects the knocked-out particle. The two spectrometers are essentially identical in terms of the magnetic components and optics. By changing the polarities of the magnets, their roles can be interchanged. At the exit of each spectrometer, on the platform, a shielding house (detector hut) has been built to prevent detector packages and associated electronics from radiation damage, and to minimize the rates in the detectors caused by particles not passing through the spectrometer.

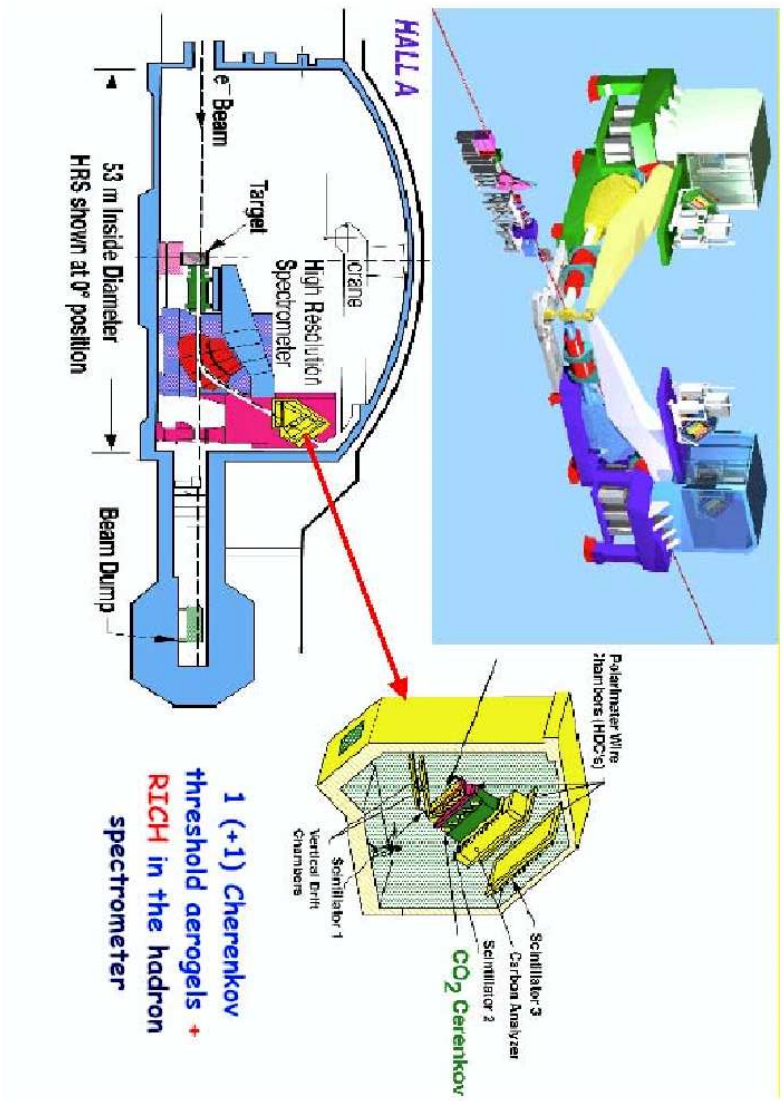

Figure 4.2: Schematics of the Hall A. The beam line, the High Resolution Spectrometers with the detector equipment.

4.4 The Beam

The beam current delivered to Hall A is measured by four Beam Current Monitors (BCMs) placed in the beamline about 24.5 m upstream of the target. A BCM is simply a cylindrical resonant cavity made out of stainless steel, 15.18 cm in diameter and 15.24 cm in length. The resonant frequency of each cavity is adjusted to 1497 MHz, which matches the frequency of the beam. Inside each cavity there are two loop antennas coaxial to the cavity. The large one has a radius that couples it to the one of the resonant mode of the cavity and is located where the H field is largest. This antenna is used to periodically test the response of the cavity by sending through it a 1497 MHz calibration signal from a current source and detecting the induced current in the large antenna. When the electron beam passes through the cavity, it excites the resonant transverse electromagnetic modes TM_{010} at 1497 MHz. The large area probe loop provides an output signal that is proportional to the current.

Two devices are used for checking the beam energy spread: the Optical Transition Radiation (OTR) Monitor and the Synchrotron Light Interferometer (SLI) Monitor [50]. The OTR Monitor consists in a 0.3 μm thin carbon foil where the transverse beam size is measured by imaging the Optical Transition Radiation on a camera and analyzing the horizontal and the vertical projections.
The Synchrotron Light Interferometer Monitor uses the Synchrotron Light Interferometer pattern to measure the transverse beam size (see [51]).

4.4.1 Raster

When a intense beam, with small spot size, hits the target, there is risk to damage the target itself, therefore a system called raster is used to move the beam on the target in a controlled way. Essentially it increases the beam spot size but always monitoring the position.
The raster is a pair of horizontal (X) and vertical (Y) air-core dipoles located 24 m upstream of the target. The raster can operate in two different modes, sinusoidal and amplitude modulated. In the sinusoidal mode both X and Y magnet pairs are driven by pure sine waves with relative 90° phase.
In the amplitude modulated mode both X and Y magnets are driven at 18 kHz with a 90° phase between X and Y, producing a circular pattern. The radius of this pattern is changed by a function generator in order to create a uniform distribution of the area swept out by the beam motion.

4.5 Targets

4.5.1 Solid Targets

There are different configurations allowing the use of solid targets in Hall A.
In the simplest case solid flat targets are mounted in a vertical ladder assembly. The targets mounted on the ladder are selected remotely with a motorized movement sys-

tem. Vertical position is indicated by encoders. Absolute positions have been surveyed and the accuracy of the position relative to the beam line is 0.020 *in*. Repeatability in the vertical positions with respect to the center of the target is 0.006 *in*. The accuracy in the absolute angular position of the target normal relative to the beam line is 0.1 *mm*. The repeatability of obtaining the angular position is 0.1°.
In a second configuration the vertical ladder assembly is mounted below a cryogenic target chamber (typically used for Hydrogen and Deuterium targets). The ladder can be retracted into an inverted hat which protrude through a hole in a flange in the base of the target chamber. The inverted hat contain the vertical ladder, solid target cooling tubes, and drive assembly for the ladder. When the cryotarget is retracted into its highest position, the distance between the beam position and the bottom of the cryoloop is expected to be about 20 *cm*. This is sufficient space to permit vertical mounting of seven target foils on frames that are centered 2.5 *cm* apart. Two types of target ladders and frames are currently available. One target ladder contains provision for water cooling. The second type of ladder and target frame does not have water cooling and was used during the first commissioning runs with low beam currents.
A similar movement system is installed below the waterfall target system.

4.5.2 Waterfall Target

The waterfall target system provides a target for experiments on ^{16}O. The conceptual design of the waterfall target system for Hall A is very similar to the one used at Saclay is extensively descrived in [38]. On January 2004 the waterfall has been commissioned and set for the $^{16}O(e,e'K^+)^{16}N_\Lambda$ reaction study. Few calibration data have been taken. For technical reasons the real data taking was not possible at that time and the waterfall target was not present during the April-May data taking. It will be used in the extension of the experiment scheduled on June 2005.
In the waterfall target, water forced through slits forms one or more films which are stable as a result of surface tension and adherence to stainless poles. Each waterfall foil is produced in a cell mounted in the standard scattering chamber. The water, continuously pumped from a reservoir, goes through a heat exchanger into the target zone and then back into the reservoir. All parts in contact with the water are made of stainless steel. A gear pump, magnetically coupled to a DC motor, is used to produce a stable film. Once the target is formed, it is possible to modulate, slightly, the thickness of the waterfall target, by changing the pump speed; this adds flexibility to the system and allows the user to choose the best value according to the wanted resolution and luminosity. A cooler can be used to keep the water at a constant temperature.
Elastic scattering from the hydrogen in the target is used to measure the target thickness. For continuous monitoring of the target thickness, one 'calibrates' the raw counting rate of the hadron spectrometer by the elastic peak measurements; thus it is possible to convert the proton rate seen during the measurement to an average target thickness. The waterfall target can be single foil or three-foils according to the needs of the particular experiment. The three foils are identical, 12 mm wide, and guided by poles which are 2 $mm \times 2$ mm with a matching tolerance of less than 0.15 mm.
Care is taken to optimize the foil configuration with respect to the spectrometer ac-

ceptance and ejectile trajectory, so that the scattered particles do not go through a second water foil for any of the kinematics settings of the experiment.
The target is designed to stay at a fixed angular position: the waterfall target container is a box $630 \times 68 \times 8\ mm^3$. Because it is intended to employ beam currents exceeding $50\mu A$, care must be taken in choosing the window material because of the risk of melting.
The entrance and the exit windows are circular (30 mm in diameter) and made of Be(75 μm thick). Because Be is hightly toxic, it has been plated with 13 μm of Ni and a monolayer of Au (which also serves to improve heat conductivity).
The lateral windows, which the scattered electrons and hadrons must be traverse, are made of stainless steel, $25\mu m$ thick.
Under the cell a target frame holds up to five solid targets. A target position can be selected remotely by a mechanism system driven by stepping motors and controlled by absolute encoders whose precision is 0.1 mm and 0.1°.

4.6 High Resolution Spectrometers

The vertical bending design of the High Resolution Spectrometers (HRSs) includes a pair of super-conducting quadrupoles followed by a 6.6 m long dipole magnet with focusing entrance and exit faces. Further focusing is achieved through the use of a field gradient in the dipole. Subsequent to the dipole is another super-conducting quadrupole to complete the QQDQ configuration. The performance and the optics of the spectrometers will be discussed in the following.
Two septum magnets have been added to the HRS spectrometer to allow experiments using scattering angles smaller than the minimum angle of 12.5°. This is of crucial importance for the hypernuclear experiment, since the cross sections for this experiment go down sharply with the increasing scattering angle, as previously showed (fig. 3.1).
The general characteristics of HRS are reported in Table 4.1.

4.6.1 Septum Magnets

Performance Requirements

The angular acceptance of the septum magnet (Fig. 4.3) has been designed to be ~ 4.5 mrad to keep the solid angle of the spectrometer reasonable. Good resolution in missing mass is needed, therefore the septum magnets should not modify the HRS momentum resolution. Moreover, the aim is to have a general purpose device, so particles scattered at the new minimum angle should also reach momenta as high as the maximum central momentum analyzable by the HRS2 (4 GeV/c). The angular range of use for the septum magnets should also cover the full range from 6° to 12.5°, where it overlaps the "normal" HRS setup minimum angle (again, for all momenta up to 4 GeV/c).

Momentum range p	$0.3 \sim 4.0\ GeV/c$
Configuration	QQDQ
Bend Angle	45°
Optical Length	23.4 m
Momentum Acceptance	±4.5%
Dispersion (D)	12.4 cm/%
Radial Linear Magnification (M)	2.5
D/M	5
Momentum Resolution (FWHM) $\delta p/p$	1×10^{-4}
Angular Acceptance Horizontal	$\pm 28\ mrad$
Solid Angle $\Delta\Omega$	$\pm 60\ mrad$
Angular Resolution (FWHM) Horizontal ϕ	$\sim 6.7\ msr$
Vertical θ	2.0 mrad
Transverse Length Acceptance	$\pm 5\ cm$
Transverse Position Resolution (FWHM)	1.5 mm
Spectrometer Angle Determination Accurancy	0.1 mrad

Table 4.1: The general characteristics of HRS.

Figure 4.3: Picture of a septum magnet.

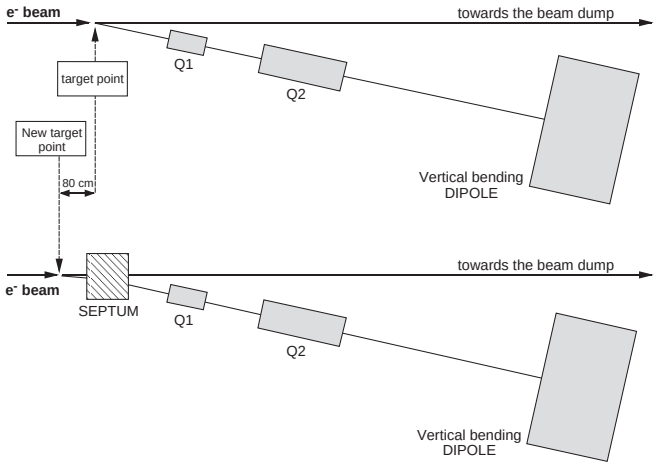

Figure 4.4: Layout of the modifications to the HRS setup

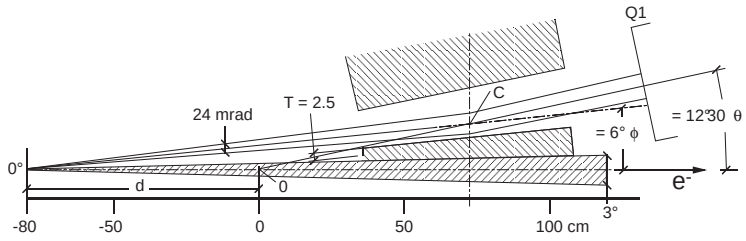

Figure 4.5: Layout of the septum insertion.

Design Criteria

Physically, the first quadrupole ($Q1$) of the spectrometers cannot be moved closer than 12.5° to the beam without hitting the beam pipe. The idea is to move the target upstream a suitable distance and to insert a horizontal-bending septum magnet before the point element in the spectrometers in such a way that the target seems to be situated on the optical axis of the two spectrometers (Fig. 4.4). This is precisely true only for the central momentum of the spectrometer, for other momenta the target appears to be shifted sideways.

The septum has to be designed in such a way that the trajectory of the particle scattered at the acceptance central angle ϕ would overlap, after being bent, the line originating from O (old target position) and making an angle θ ($\geq 12.5°$) with the beam line. In addition the septum gap has to be designed to accept all particles scattered in the acceptance cone (see Fig. 4.5 for the case $\phi = 6°$; $\theta = 12.5°$ and acceptance in the midplane plane = 24 mrad).

It has been shown therefore that the septum design is almost completely determined by two parameters: the distance d between the old and new position of the target (80 cm) and the magnet thickness T (the distance between the septum gap and the beam pipe) (Fig. 4.5). A choice of d = 80 cm and T = 2.5 cm was made. Using these values we can get a geometrical acceptance of 4.5 msr. Moreover, with a reasonable field

integral, particles of momentum up to 4 GeV/c can be analyzed for angles from 6° to 12.5°.

The mechanical design of the septum is determined more by the Hall A geometrical layout and the maximum current density available in superconducting coils than by optic considerations. The septum, because of the short length and small bend angle, can be treated as a perturbation to the optical properties of HRS. On the other hand, the limited room available, the required geometrical acceptance and the difficulty of obtaining highly homogenous magnetic fields with thin coils have set severe constraints on the septum design.

In Table 4.2 we summarize the dimensions of the septum. In Table 4.3 we report the

Length *	88. cm
Heigth of the gap	25. cm
Width of gap entrance edge	10.4 cm
Width of gap exit edge	18.4 cm
Angular acceptance	4.7 msr
Magnetic length	84. cm

(* length includes length of the coils outside the yoke)

Table 4.2: The dimensions of the septum magnets.

septum parameters that depend on momentum and scattering angle of the detected particles. P is the scattered particle momentum, θ is the scattering angle, β is the horizontal bending angle of the septum magnet, the magnetic field (in the region of constant field) and field integral over the path are B_0 and $B \cdot dl$. R is the horizontal radius of curvature for the septum magnet.

P	θ	β	R	$B \cdot dl$	B_0
GeV/c	degrees	degrees	cm	Tesla-m	Tesla
2	6	6.5	740.8	0.76	0.9
4	12.5	11.9	404.6	1.39	1.65
4	6	6.5	740.8	1.51	1.8
4	12.5	11.9	404.6	2.77	3.3

Table 4.3: The parameters of the septum magnets.

Expected Performances

Standard techniques and modelling shows that the perturbation of the septum to the HRS spectrometer features is small. Indeed the momentum and target coordinate resolutions of the system septum + HRS obtained in this way (considering only fixed momentum particles, see appendix) is quite close to the resolutions of the HRS alone.

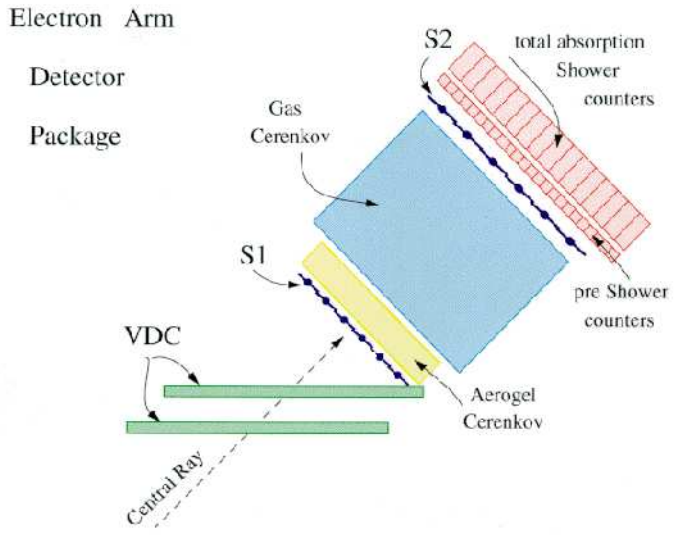

Figure 4.6: Layout of detector package in the electron arm

The calculations mentioned in the previous paragraph and described in Appendix, give the following results: the momentum resolution is expected to be 1.2×10^{-4} using kapton for the spectrometer exit window, and 1.35×10^{-4} for the Ti one. The resolution in θ is 0.96 mr and 1.26 mr respectively. The effect of the multiple scattering from the target and the target window (waterfall target) is very small. In fact resolution in θ remains 0.96 mrad if we take into account the multiple scattering from the target. The influence of the target window is of the same order. The resolution in y is equal to 0.365 mm for the kapton window and 0.435 mm for the Ti one. The resolution in ϕ is respectively, 0.38 mr and 0.50 mr.
A Monte Carlo simulation has been performed in order to evaluate that the missing energy resolution for the hypernuclear experiment is not affected by the introduction of the septum magnets. The Monte Carlo confirmed that the insertion of the septum magnets is compatible with a missing energy resolution $\leq 500\ keV$, assuming in the simulation a beam resolution of $\sigma_E/E = 2.5 \times 10^{-5}$, a HRS momentum resolution of $\simeq 1.0 \times 10^{-4}$, and an angular error of 1 mr.

4.7 Detector Package

The detector packages [39] for the left and right spectrometers are almost identical (see fig. 4.6), except for the PID apparatus, The used detector package includes:

- a set of two scintillator planes, to provide the trigger,
- a set of two Vertical Drift Chambers (VDCs) to provide tracking information (position and direction),
- a gas threshold Čerenkov detector in the electron arm, to provide e^-/π^- separa-

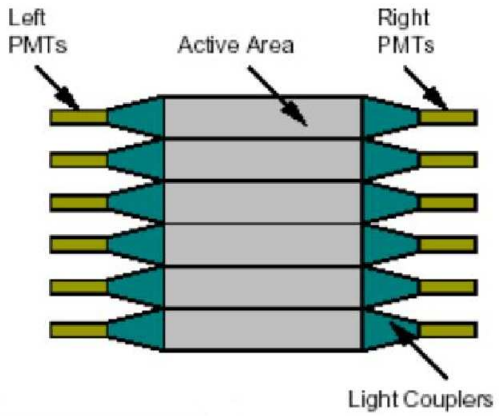

Figure 4.7: Schematic of scintillator plane.

tion (electron PID),

- two aerogel threshold Čerenkov detectors in the hadronic arm, to provide $p/K^+/\pi^+$ separation (hadron PID),
- a set of Lead Glass Counter in the electron arm, to provide additional electron PID,
- A RICH detector in the hadronic arm, to provide additional hadron PID.

4.7.1 Scintillators and Trigger Electronics

There are two primary trigger scintillator plans (S1 and S2), separated by a distance of 2 m. Each plane consists of six overlapping paddles (see fig. 4.7) made of thin plastic scintillators to minimize hadron absorption. To each scintillator paddle are attached two photomultipliers tubes (PMT's), called the left and right PMT. The time resolution of each plane is $\sigma = 0.30\ ns$. Triggers are generated by the PMT signals from the scintillator planes and are sent to all other detectors and Data Acquisition (DAQ).
Discussion of the trigger types are presented in the Chapter 6.

4.7.2 Vertical Drift Chambers

Particle tracking of each arm of HRS is provided by the two Vertical Drift Chambers (VDCs) [16, 19] positioned 23 cm away from each other. The position of the first VDC almost coincides with the spectrometer focal plane. Each VDC is composed of two wire planes in a standard U-V configuration, that is the wires of one plane are perpendicular

to that on the other plane, and are oriented at an angle of 45° (−45°) with respect to the dispersive and the not-dispersive directions. Both wire planes lie in the laboratory horizontal plane and the nominal particle trajectory crosses the wire planes at an angle of 45°.
Each VDC has three high-voltage plates at about -4 kV, one between the U and the V planes and two on opposite sides. The spacing between planes is 26 mm.
When a charged particle goes through the chamber, it ionizes the gas inside the chamber and leaves behind a track of electrons and ions along its trajectory. The gas supplied to the VDCs is 62/38 Ar/C_2H_6 mixture, with a flow rate of 10 l/h. the ionization electrons accelerate towards the wires along the path of least time. This time is measured by Time-to-Digital Converter (TDC), which is started by the triggered wire and stopped by the event trigger supervisor, the electronic device which manage the trigger in the Hall A Data Acquisition system. The basic idea of particle tracking is the following: since the drift velocity of ionization electrons in the operating gas is known to be $50\mu m/ns$, the drift distance from the trajectory to each fired wire can then be extracted from the corresponding TDC output. Combining the drift distance of all fired wires together gives the trajectory of the charged particle. A charged particle with a track at the nominal angle of 45° with respect to the lab horizontal plane typically triggers five wires, while those at the extreme angle of 52° triggers three wires. The position resolution in each direction is 225 μm FWHM. Therefore the two VDC separated by 50 cm are capable of measuring the two angles of the particle with a resolution of ~ 0.3 $mrad$ FWHM.

4.7.3 Gas Threshold Čerenkov Detector

The task of the Gas threshold Čerenkov detector is the separation of the scattered electrons from the background particles. The Gas Čerenkov detector for HRS (Fig. 4.8), designed and built by the collaboration with the INFN and Saclay groups, is operated with CO_2 at atmospheric pressure. The length of the particle path in the gas radiator of the used gas Čerenkov detector is 130 cm. The refractive index is 1.00041 which gives a threshold of nearly 17 MeV/c for electrons and nearly 4.8 GeV/c for pions. So within a momentum range of $0.02 \sim 4.8$ GeV/c, which is larger than the HRS designed momentum range $0.30 \sim 4.0$ GeV/c, only electrons and not pions can emit Čerenkov light and trigger an ADC signal.
There are two gas Čerenkov detectors in the Hall A equipment, one on each arm. In E94-107 experiment only the electron-arm one has been used. The structure of the gas Čerenkov detectors on the two HRSs is very similar. Each one is made with a steel frame with thin entry and exit windows made of tedlar. Ten spherical mirrors positioned as a 2 $(horizontal)$ × 5 $(vertical)$ array are used in each detector to collect Čerenkov light. These mirrors are specially built to be light weight resulting in a very small total thickness (0.23 g/cm^2) traversed by the particles. The position and orientation of these mirrors are designed in a way such that the Cerenkov light emitted by the scattered electrons can be efficiently collected. Each mirror is coupled to a photo-multiplier tube (BURLE 8854 PMT). The mirrors have radius of curvature of 90 cm, the PMTs are placed at a distance of $90\ cm/2 = 45\ cm$ from the mirrors, where

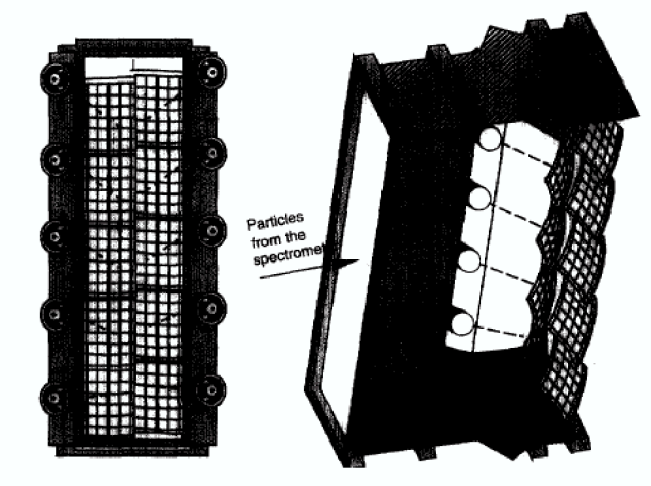

Figure 4.8: Schematic of Gas Čerenkov detector.

the parallel rays of incident light on the mirrors are approximatively focussed.
The light is converted to electronic signals by PMTs and sent to ADCs. The summed signal of all ten ADCs gives information about the total light emitted by the particle and has a different shape for electron and pion events. In principle pions should not produce any signal in the Čerenkov detector. However they can interact with the matter they pass through and extract knock-out electrons (Δ rays) from atoms. The Δ rays will produce Čerenkov light and trigger the ADCs. Since atomic electrons are in general not moving in the same direction as the primary electrons coming from the target, the Čerenkov light emitted by Δ rays will not be efficiently collected by the mirrors, hence the correspondent summed ADC signals are mostly due to single photo-electron pulse height. On the other hand, almost all the Čerenkov light emitted by the primary electrons is collected by the mirrors, therefore the signals generated are mainly correspondent to multiple photo-electron pulse height. The position and the width of the correspondent peak in the ADC distribution depend on the average number of photo-electrons, which is determined by the PMT performance and whether all the Čerenkov light is collected by the mirrors. The number of photo-electrons determines how well one can separate the single photo-electron peak from the multiple photo-electron one, which subsequently determines the PID quality of Čerenkov detector. The average number of photoelectrons $N_{p.e.}$ for each PMT can be extracted from detailed mirror-by-mirror analysis for the Čerenkov detector. A total number of ($\simeq 14$ $p.e.$) has been obtained since 1997 [40]. The mirrors were designed and built by INFN group in Rome [23].
In the Chapt. 6 its good performance will be confirmed.

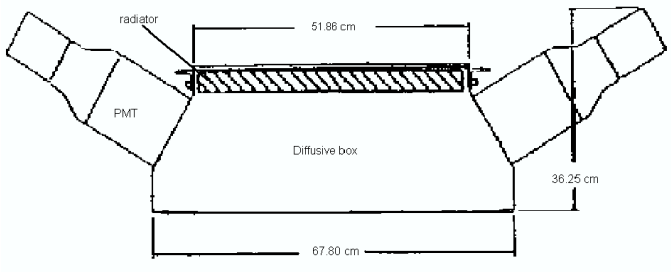

Figure 4.9: Schematic of aerogel Čerenkov detector.

4.7.4 Lead Glass Counters

Lead glass counters provide an additional system for e^-/π^- separation. The signal detected by lead glass counters is linearly proportional to the energy deposited by the incoming particle. Electromagnetic showers develop in the counters, whereas hadronic showers do not due to the longer hadronic mean free path. Therefore the longitudinal distribution of the energy deposited in the counter can be used to identify the incident particles. In the case of Hall A there are two distributions of energy: low ADC signal for hadrons and high ADC signal for electrons. the limitation on PID efficiency of the lead glass counter (also called shower) come from separating the tail of the two distributions and hence depends on the energy resolution. At higher energy the relative resolution of a lead glass counter improves and leads to better separation between the two distribution. A double-layered lead glass counter can provide better separation because the second layer can further separate the hadrons which are contaminated with electrons in the first layer.
The two lead glass counters installed in the electron arm for the experiment are called 'preshower' and 'shower' respectively. The preshower has $2 \times 24 = 48$ blocks of lead glass oriented transversely with respect to the direction of scattered electrons. the shower has 5×20 blocks of lead glass oriented parallelly to the scattered electrons.

4.7.5 Aerogel Threshold Čerenkov Detectors

The Hadron Arm of HRS is equipped with two aerogel threshold Čerenkov detectors (fig. 4.9 and fig. 4.10). These detectors were designed and built with the collaboration between Jefferson Lab, the INFN (Sezione di Bari and Gruppo Collegato Sanità), University of Regina, and Florida International University. They are diffusion-type aerogel counters, called AERO1 and AERO2. AERO1 has 24 PMTs (Burle 8854). The 9 cm thick aerogel used in AERO1 has a refraction index of 1.015, giving a threshold of 2.84 (0.803) GeV/c for kaons (pions). The average number of photoelectrons for relativistic electrons in AERO1 is $\simeq 8$. The AERO2 counter has 26 PMTs (XP3372B1). The aerogel in AERO2 has a refraction index of 1.055, giving a threshold of 2.8 (0.415) GeV/c for protons (pions). The thickness of the radiator in AERO2 is 5 cm, producing an average number of ≈ 30 photoelectrons for relativistic electrons.
Since the Čerenkov detectors play a critical role on the particle identification needed

Figure 4.10: Aerogel Čerenkov detector in the Hall A

for the E94-107 experiment, the work in the design and construction of these detectors by INFN group has been very strong [42]. We have shown that diffusion-box detectors had to be build for their better performances with respect to reflective-box detectors used previously [41].

4.7.6 RICH Detector

The kaon identification provided by the Time of Flight and the Aerogel Čerenkov detectors is not sufficient for very-forward-angle experiments as the E94-107 Experiment, where the very high p/π^+ background gives a large contamination in the $(e, e'K^+)$ missing energy spectrum.
To improve the particle identification (PID) in the Hadron Arm, a proximity focusing Ring Imaging Cherenkov Detector (RICH) has been implemented (Fig. 4.11).
A RICH detector detects the Čerenkov light on a photosensitive plane and reconstructs the Čerenkov angle of the light emitted by the incident particle (Fig. 4.12). Since its development and implementation has been an important part of the current PhD work, it will be described extensively in the next chapter.

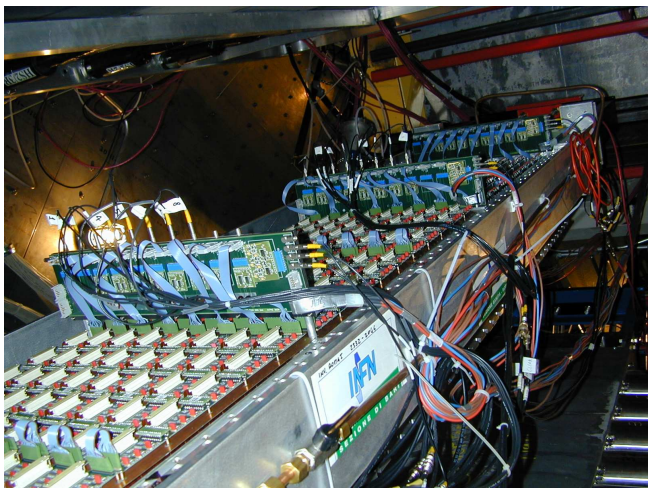

Figure 4.11: The RICH detector installed in Hall A.

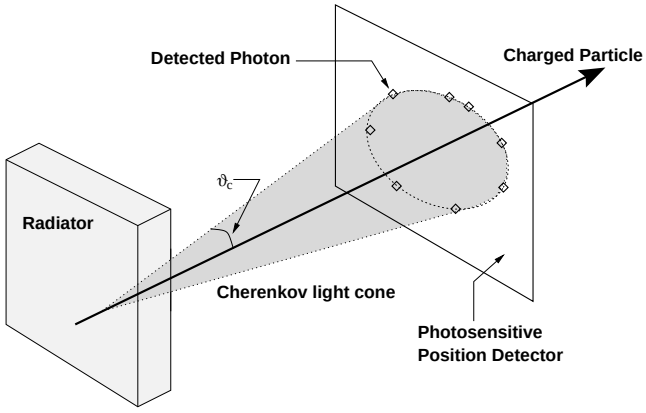

Figure 4.12: Working principle of proximity focusing RICH detector.

Chapter 5

The Particle Identification and the RICH detector

5.1 The Particle Identification

As emphasized in the previous chapters the main goal of the experiment is obtaining clean, high resolution, missing energy spectra. The high energy resolution depends essentially on the beam energy stability and on the spectrometers momentum resolution. Neverthless, as it will be shown in this chapter, a powerful Particle Identification (PID) system is needed in order to obtain "clean" missing mass spectra. The PID is a very difficult task in this experiment. In fact the scattered and produced particles are detected at very forward angles, so very high background of protons and pions are expected. This makes very difficult the unambiguous kaon identification needed for "background free" missing mass spectra. A Monte Carlo simulation was performed for evaluating the particle identification requirements.
Table 3.2 and 3.3 show the expected single and coincidence rates of the $^{16}O(e,e'K^+)$ $^{16}N_\Lambda$, $^{9}Be(e,e'K^+)^{9}Li_\Lambda$, $^{12}C(e,e'K^+)^{12}B_\Lambda$ and $^{7}Li(e,e'K^+)^{7}He_\Lambda$ reactions.
The accidental coincidence rates coming from singles $(e,e')\otimes(e,\pi^+)$ $(e,e')\otimes(e,p)$ are much higher than the expected hypernuclear production which is at the level of tens counts per hour in the case of the oxygen target, dropping to few counts per hour for the beryllium case. More levels for the hypernuclear $^{16}N_\Lambda$ spectrum are predicted to have a reasonably high counting rates close to the $K^+ - \Lambda$ production threshold and above (about 10 MeV). These are not considered in the simulation. The results obtained with different assumption on the rejection power of background events will be shown and discussed. We start discussing the performances of the "standard Hall A" PID equipments.

5.1.1 Monte Carlo simulation

Besides the reconstruction of usual phase space variables, the simulation is based on the reconstruction of the coincidence time spectra and the Missing Energy spectra as they are built in the analysis, when data come from different sources. In this case we have taken into account seven 'event types':

1) $(e, e'\pi^+)$ RANDOM COINCIDENCES from singles $(e, e') \otimes (e, \pi^+)$

2) $(e, e'K^+)$ RANDOM COINCIDENCES from singles $(e, e') \otimes (e, K^+)$

3) $(e, e'p)$ RANDOM COINCIDENCES from singles $(e, e') \otimes (e, p)$

4) $(e, e'\pi^+)$ TRUE COINCIDENCES in the continuum of the Missing Energy spectra

5) $(e, e'K^+)$ TRUE COINCIDENCES in the continuum of the Missing Energy spectra

6) $(e, e'p)$ TRUE COINCIDENCES in the continuum of the Missing Energy spectra

7) $(e, e'K^+)$ TRUE COINCIDENCES with a bound state residuum (hypernuclear formation).

Different sources of background are therefore taken into account, and the code is versatile enough to allow for different selection criteria on the particles.
As an example, a pion can be TOTALLY rejected or rejected only with a given factor (i.e. 95% is a reasonable number with a threshold aerogel Čerenkov counter) or not rejected at all. Events with particles other than electrons in the electron arm are not considered. This is due to the excellent rejection for π^- (and heavier hadrons) that can be reached making use of the CO_2 gas Čerenkov detector and the lead glass counters.
INPUT for the Monte Carlo are : Acquisition Time, the kinematical settings, (e, e') , (e, π^+), (e, K^+), (e, p) single rates, $(e, e'\pi^+)$, $(e, e'K^+)$, $(e, e'p)$ coincidence rates in the continuum, $(e, e'K^+)$ TRUE coincidence rates in bound states and the Missing Energy positions, acceptances of the spectrometers, resolutions (beam, momenta, angles, coincidence time).
The main assumption under which the simulation has been performed are:

- 120 hours data taking at the luminosity of the experiment,

- TOTAL COINCIDENCE TIME = 50 ns,

- Resolution of the COINCIDENCE TIME = 1 ns FWHM,

- Electron beam resolution = 6.0×10^{-5} FWHM,

- Electron and hadron momentum HRS resolutions = $1.5 \times 10^{-4}(FWHM)$,

- Angles resolution = 2 mr,
  Path Length from target to timing defining detector assumed = 25 m.

Rates for REAL COINCIDENCES $(e, e'\pi^+)$, $(e, e'K^+)$ and $(e, e'p)$ in the continuum (of the Missing Energy spectrum) were just estimates, since we did not compute the cross sections for all the participating processes. Moreover, in these cases the events are treated to fill the Missing Energy spectra as if they were random coincidences. Such assumption is generally acceptable ("smooth" missing energy distribution, for example coming from quasi-elastic regions) Anyway, the main sources of background are the

random coincidences $(e,e')\otimes(e;\pi^+)$ and $(e,e')\otimes(e,p)$, which are, of course, distributed randomly according to the phase space probability and have to be subtracted.
The case of the oxygen target has been considered as one of the "easiest" case (^{12}C as well), in the sense that the signal to noise ratio is predicted to be higher than in the other nuclei (see rates in Table 3.2). The counting rates have been reduced conservatively by a factor 2 since the theoretical models have large uncertainties.
Let us define the PID rejection as the percentage of proton or pion misidentified as kaon (sometimes it has used the rejection power as the inverse of the rejection). The rejection has to not affect the detection efficiency of kaons (to not misidentify kaon as pions or protons). In Fig. 5.1 the coincidence timing spectra of the reaction $^{16}O(e,eK^+)^{16}N_\Lambda$ is obtained under different hypothesis:

a) no particle selection applied: the $(e,e'K^+)$ peak is "hidden" in the background of random coincidences (flat in coincidence time) ;

b) a selection based on a PID rejection of protons and pions of 95% (which means misidentify one proton or pion as a kaon in 5 out of 100 cases) and a 95% detection efficiency for kaons has been assumed;

c) a selection based on a very powerful PID rejection of protons and pions of 1×10^4, which could be obtained with a Ring Imaging CHerenkov (RICH) detector, with a kaon efficiency of 90% has been assumed;

d) the identification of different contributions of the real coincidences of kaons into the two channels: the hypernuclear bound states production and the unbound $K^+-\Lambda$ (quasi-free) production.

Interesting events for this experiment are only a small fraction of the total $(e,e'K^+)$ events. However, it has to be noted that these events do not affect the interesting region of the hypernuclear missing energy excitation spectra. In these spectra such a contribution starts above the $K^+-\Lambda$ production threshold and in the following plots has been neglected. Further analysis has been carried out considering a "standard PID" equipment (see below) with a 95% p,π^+ rejection power (i.e. 5% p,π contamination) and a 95% kaon detection efficiency.

In Fig. 5.2 the missing energy spectra are reported, without any timing cut (plot b) and by selecting true kaon coincidences (plot c). In this last case, in the region close to the bound states hypernuclear production (0 MeV) two peaks become visible. In Fig. 5.3 (plot a) this region has been expanded and the background (plot b) subtracted (plot c). The "ideal" background free spectrum (plot d) is also reported for comparison.

Fig. 5.4 shows again the subtracted spectra in comparison with the "infinite resolution" oxygen hypernuclear levels. The experiment clearly cannot distinguish the doublet components. The experimental missing energy resolution from the assumed detector performances (considered to be conservative) comes out to be about 450 keV FWHM. The same simulation has been carried out for the beryllium target case, to explore the viability of the study of the reaction $^9Be(e,e'K^+)^9Li_\Lambda$. Fig. 5.5 shows the results of such a simulation. It can be clearly seen how the low signal to noise ratio makes the spectroscopic measurements particularly hard. A clear assignment can

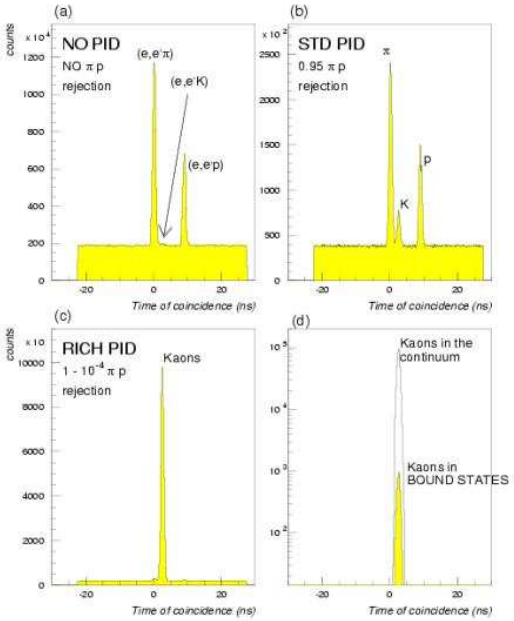

Figure 5.1: Monte Carlo simulation for the $^{16}O(e,e'K^+)^{16}N_\Lambda$ reaction. Random coincidence event reduction for splitted target already included. Timing spectra: (a) no particle selection applied. The $(e,e'K^+)$ peak is "hidden" in the background of random coincidences (flat in coincidence time); (b) selection based on a PID rejection of protons and pions of 95 % and the same efficiency detection for kaons; (c) selection based on a very powerful PID rejection of protons and pions of 10^{-4} and 95% detection efficiency for kaons; (d) different contribution of the real coincidences of kaons into the two channels: the hypernuclear bound-state production and the unbound $K^+ - \Lambda$ (quasi-free) production.

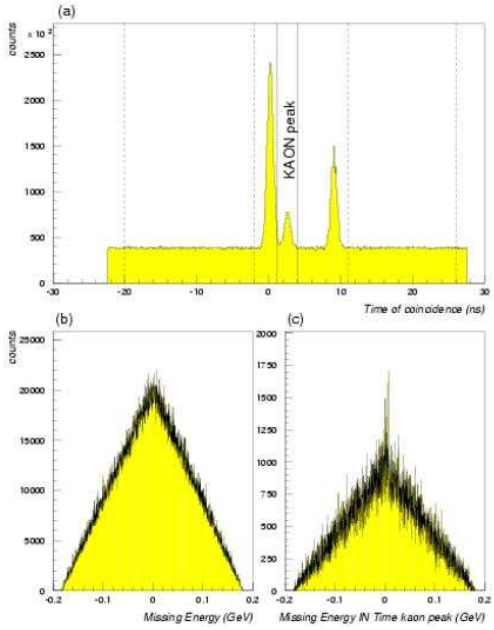

Figure 5.2: $^{16}O(e,e'K^+)^{16}N_\Lambda$ reaction. (a) Timing spectrum: solid lines select a cut for events "in the kaon peak", dashed lines select events "off the kaon peak" used for subtraction. (b) Missing energy spectrum for all the events entering in the spectrum (a). (c) Missing energy spectrum for events "in the kaon peak".

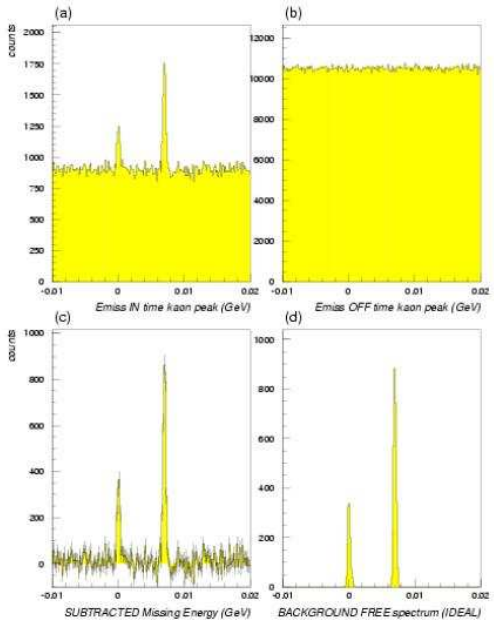

Figure 5.3: $^{16}O(e,e'K^+)^{16}N_\Lambda$ missing energy spectra. (a) Hypernuclear bound-state region "in the kaon peak"; (b) same region "off the kaon peak"; (c) the subtracted spectrum; (d) the "ideal" background-free spectrum.

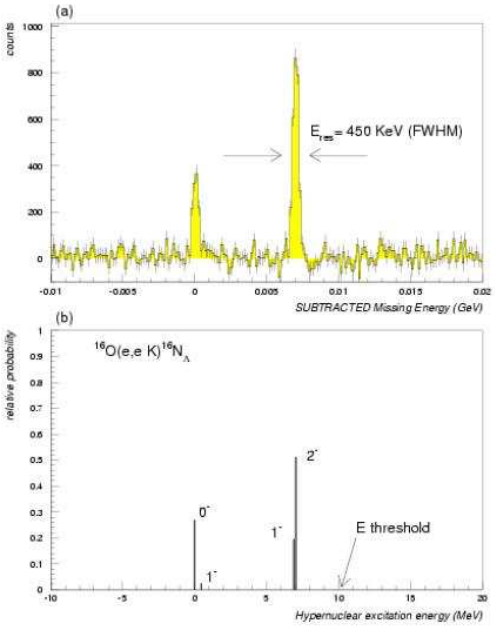

Figure 5.4: $^{16}O(e,e'K^+)^{16}N_\Lambda$ missing energy subtracted spectrum in comparison with the "infinite resolution" oxygen hypernuclear spectrum.

be only given to the second component of the first doublet, loosing any (important) information on the position of the first component. In this case it should be realized that a standard PID system capable to reject pions and protons only at a 95% level is probably not enough to extract outstanding physical information.

A clear improvement can be achieved with a more "powerful" detector, like the Ring CHerenkov Imaging (RICH) detector. A self-explaining comparison of the quality of the measurements obtained with or without the use of a RICH detector is reported in Fig. 5.6. In simulating the "RICH data" a total rejection of 10^4 for pions and kaons has been assumed, or, speaking in term of efficiency, a total $\pi - p$ efficiency of 10^{-4}. This number is a very conservative one if the PID system is composed of both the threshold aerogel counters (which can be used as a hardware trigger limiting rates) AND the RICH detector. In this case such an assumption is accomplished considering a 5% efficiency from the threshold counters (a very reasonable number as reported below) coupled to a 0.2% π efficiency for the RICH, a number very much conservative compared to the actual RICH capabilities.

Gas Čerenkov Detector and Lead Glass counters in the electron arm

Negative-pion single rates were evaluated to be at the level of $\sim 1.5 \times 10^5\ Hz$, the same as the electron single rates. Operated in the threshold mode, the Čerenkov counter were expected to give pion rejection ratios up to 10^3. The dominant background (knock-on electrons) can be reduced another 2 orders of magnitude by the lead glass shower counters, giving a total pion rejection ratio $\geq 10^5$. Since the experiment can be safely carried out with a pion rejection of 10^2, the predicted contamination of π^- in the electron arm is well below the limit of the experiment. Contamination of negative pions

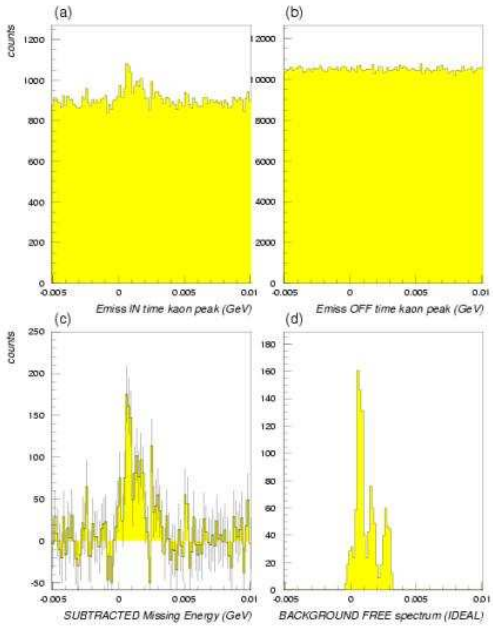

Figure 5.5: Same as Fig. 5.3 for $^{9}Be(e,e'K^{+})^{9}Li_{\Lambda}$ reaction.

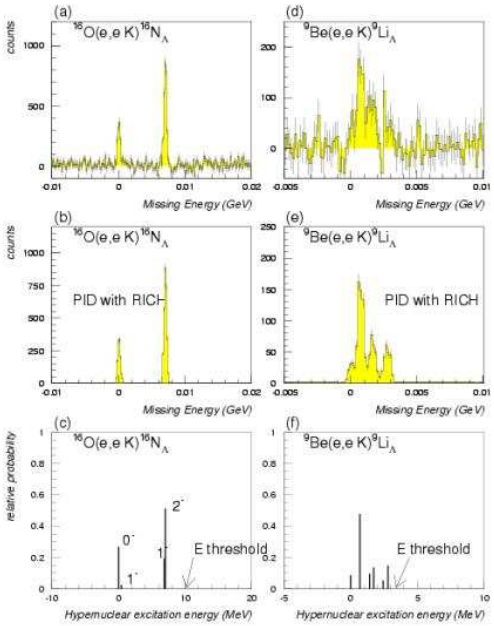

Figure 5.6: High counting $^{16}O(e,e'K^{+})^{16}N_{\Lambda}$ vs low counting $^{9}Be(e,e'K^{+})^{9}Li_{\Lambda}$.

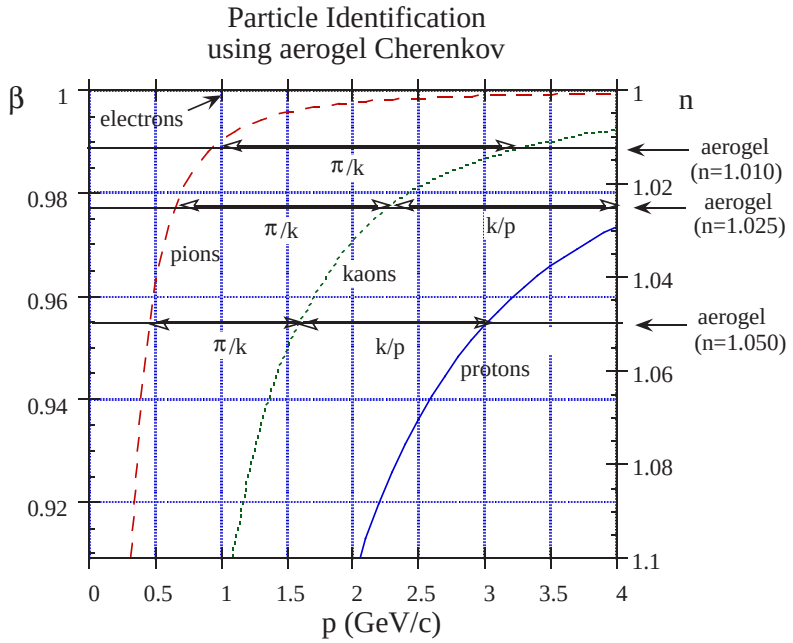

Figure 5.7: PID with Threshold aerogel Čerenkov counters.

in the electron arm is not an issue for this experiment.

Aerogel Čerenkov counters

Two aerogel Čerenkov counters with $n = 1.015$ and $n = 1.055$ (previously described) have been used. In fig. 5.7 the velocity β vs the momentum of pions, kaons and protons is reported. In the axis on the right $n = 1/\beta$ is shown which represent the index of refraction at threshold for a given momentum. The figure shows that with the choice of $n = 1.05$ it is possible to separate kaons (above threshold) from protons (below threshold) in the range 1.6 - 3.0 GeV/c. This range was needed for another experiment (E98-108).
The separation between pions and kaons can be achieved using n = 1.01, so that the combination of the two counters allows to identify the kaons. Before the experiment, we have performed tests with suitable extrapolation from the electron, pion and proton case to the kaon case, showing that the use of two aerogel Čerenkov counters with index of refraction n = 1.055 and n = 1.015 (diffusion box) provides the assumed performances of a 95% rejection factor for pions and protons. The efficiency for kaon detection being about 98%. On the other hand a rejection factor at the level of 95% for particles below threshold is consistent with what can be found in literature for this type of detectors.

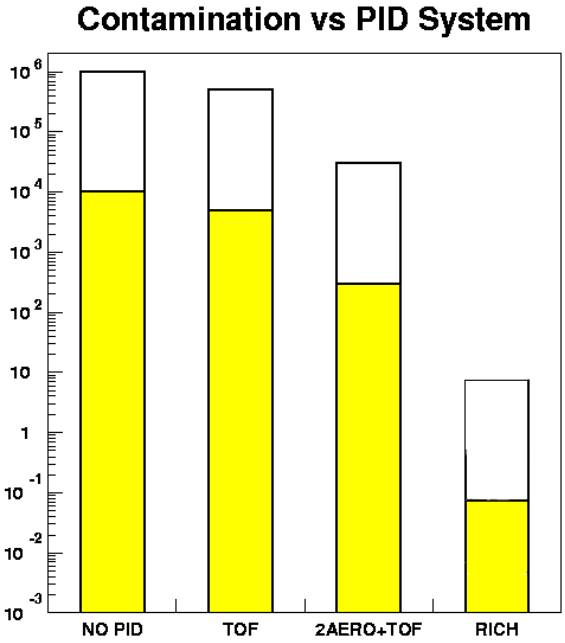

Figure 5.8: Contamination of π and p on the K signal in experiment E94-107 with three PID systems; rates are from table 3.2. The RICH PID is undoubtedly superior.

5.2 Improving the PID: the RICH detector

At the luminosity of the experiment, single rates are $\sim 50\ kHz$ on the Hadron Arm and $\sim 200\ kHz$ on the Electron Arm. This gives rise to high rates of random coincidences, to be compared with the low hypernuclear production which consists of few counts/hour/level. The expected signal and accidentals rates [37] were shown in table 3.2. Since the previously described hypernuclear spectroscopy program detects energy level peaks in the $(e, e'K^+)$ missing energy spectrum, the contamination C (10^4 - 10^6 from table 3.2) of pions and protons in the kaon signal plays an important role.

In fact, assuming the naive criterion that a peak in the missing energy spectrum is a real hypernuclear energy level if the counts under it (S) are at least 4 times the mean background fluctuation ($\sqrt{B}$), the minimization of the contamination ($C \equiv B/S$, i.e. good particle identification) corresponds to a proportional improvement of the experimental sensitivity ($S/C > 16$, where $C \equiv B/S$) or to a proportional decrease of the required experimental time ($t_r > 16\, C/s$, where s is the signal rate).

Therefore, an effective particle identification (PID) system has been designed and built in the INFN-Sanità laboratory in Rome; it is based on a RICH detector with a proximity focusing geometry, a liquid C_6F_{14} radiator and a CsI photon converter.
The freon purification system has been built at Jefferson Lab.
The superior performances of this RICH are outlined in figure 5.8 where they are compared with two PID systems based on a Time Of Flight (TOF) with a path-length base of 3 m (distance between the two plane of scintillators in the detector hut, see chapt. 4) and two aerogel threshold Čerenkov detectors.

5.2.1 Design and expected performances

A research program has been pursued first to investigate potential candidates for a HRS PID upgrade. The single-arm TOF technique and the RICH detectors were the main candidates. The former had to be dismissed due to the prohibitive time resolution[1] needed to obtain the required kaon identication. On the other hand, the RICH technique can provide the needed PID capability. RICH detectors have been succesfully used as particle identification devices for many years.

At least three types of RICH detectors with different geometries and radiators could provide the needed performance for the requested PID: two of them are based on a C_6F_{14} radiator and on a CsI pad photodetector; the other uses an aerogel as radiator and phototubes (or Hybrid Photo Diodes, HPD's) as photodetectors.

The C_6F_{14}/CsI RICHes

We have considered two different geometries, the proximity focused and the mirror focused in partial filling mode. The main difference is the presence of a focusing mirror in the latter option. The radiator is the liquid freon C_6F_{14} (perfluorohexane) with refractive index of 1.277 (at 175 nm) and the photons are converted into electrons by a thin film of CsI deposited on the cathode (pad plane) of a MWPC providing a high Quantum Efficiency (QE) below its photoelectric threshold of 210 nm. In the proximity focused option, a drift electrode grid prevents the collection of the secondary electrons produced by the incoming charge particle, by the pad cathode.

Several concurrent restrictions forced us to choose the C_6F_{14} liquid radiator for the detector:

1. the momentum range of interest: 2 GeV/c, with the optional extension to 4 GeV/c;
2. the particles we want to identify: π, K and p;
3. the energy range of the Čerenkov photon detection; this is limited to the far ultraviolet photons, that is $\lambda < 200$ nm.

As a consequence, all components along the photon trajectories, from the radiator to the cathode pad, must be UV transparent.

The aerogel based RICH

A prototype of the first RICH detector using silica aerogel has been tested at CERN in the 1997 [43], the radiator of the first aerogel RICH has been installed in the HERMES apparatus at the HERA collider (Hamburg) in spring 1998; it is in operation since August 1998. The photons emitted in the radiators are reflected by a spherical mirror to a plane photodetector made of an array of 3/4" PMTs. Almost the same detector could have been installed in the Hall A spectrometer; some changes should have been adopted: minor changes in the geometry, a radiator refractive index of 1.05 and optionally the replacement of the PMTs with HPDs as photon detector.

[1] Using a path of 5 m, and two segmented hodoscopes, the equivalent PMT time resolution must be better than 30 ps!

Comparison

The performance of a RICH can be characterized by the well-known approximated relation:

$$n_\sigma \sim \sqrt{\frac{m_A^2 - m_B^2}{2 \tan\theta_c \, p \, \sigma_\theta^r}} \tag{5.1}$$

where:

- n_σ is the separation between the two particles[2], that is the distance, in sigma unit, between the two particles distributions with width σ;
- m_A and m_B are the particles masses, both with momentum p;
- θ_c is the mean Cherenkov angle (over the detected photon energy spectrum);
- $\sigma_\theta^r = \sigma_\theta^{pe}/\sqrt{N_{pe}}$ is the error in the determination of θ_c in a ring; here σ_θ^{pe} is the single photon angle uncertienty and N_{pe} is the number of detected photoelectrons which contribute to the measurement of θ_c. The detected photoeletrons can be explicity written as $N_{pe} = LN_0 \sin^2\theta_c$; here L is the radiator thickness, N_0 is the figure-of-merit of the detector.

The separation power for particle of masses m_A and m_B can be also written as

$$\theta_A - \theta_B = n_\sigma \sigma_\theta. \tag{5.2}$$

The error on the angle measurement of the single photon depends on several different contributions, the chromaticity of the radiator, the localization of the photon on the photodetector, the optics (geometry) of the detector. This last error is different for the two freon/CsI RICH options; the focusing mirror reduces this error, leaving the other two practically unchanged and therefore increases the separation (that is to reduce the contamination). On the other side, in the partial filling case, the photons have some probability to be absorbed by the radiator after their reflection on the mirror; this correspond to a smaller N_{pe} (of the order of 15% in the proposed geometry) compared to the proximity focused system.

Combining equation 5.1 with the values of table 5.1, it is possible to determine that the aerogel based detector should have offered better performance with respect to the freon/CsI ones. However the performance of the proximity focused system allows a good separation, suitable for the Hall A PID requirements.

The aerogel RICH is much more expensive due to the high prices of the aerogel material and especially of the photodetector. The latter must consist of single-photon, visible-light-sensitive detectors with relatively high position resolution, that is traditional fractional-inch PMT (or Multi-Anode-PMT) or the new HPD which are not yet economically available.

[2]The contamination is directly related to this parameter: in the gaussian approximation, the contamination of particles A in particles B is $C(A/B) \sim P_A/P_B \int_{n_\sigma/2}^{\infty} G(\sigma) / \int_{-n_\sigma/2}^{\infty} G(\sigma)$; P_A (P_B) is the population of the particle A (B) and $G(\sigma)$ is the normalized gaussian distribution, with variance σ. As an example, when $P_A/P_B = 100$ and $n_\sigma/2 = 10$, $C(A/B) \sim 10^{-5}$.

Table 5.1: Typical quantities of the 3 RICH options. The proximity focused data are taken directly from the ALICE report [46] while the partial filling are derived from them. The aerogel RICH data refer to a 3/4"-PMT matrix photodetector.

Quantity	Proximity Focused	Partial Filling	Aerogel
n	1.218	1.218	1.05
σ_θ^{pe} (mrad)	10	6	9
N_0 (cm^{-1})	40	35	30
L (cm)	1.	1.	5.
N_{pe} (derived)	16.	14.	13.
n_σ (at 2 GeV/c)			
$\pi - K$	18	25	40
$K - p$	40	70	100

Table 5.2: Advantages and disadvantages of the 3 options considered.

Feature	Proximity Focused	Partial Filling	Aerogel
n_σ	good	pretty good	very good
geometry	very compact	suitable	suitable
rad. length (X_0)	0.16	0.15	0.11
complexity	low	medium	low
reliability	extensively tested	to be tested	tested
readout	analog	analog	digital
cost	low	medium	high

The proximity focused system is relatively simple. Its geometry is more compact than the other options and a real detector (which have been installed in STAR experiment at Brookhaven) has been successfully and extensively tested at CERN by the RD26 collaboration [46].

In Table 5.2 we summarize the features (positive and negative) of each option. Finally we choose the proximity-focused solution: although it does not have the best performance, it meets our PID requirements. It is fundamental that the system has been extensively investigated and tested by the ALICE-HMPID group at CERN.

The C_6F_{14}/CsI RICH simulation

The Hall A RICH detector is conceptually identical to the ALICE-HMPID RICH detector [46]. In order to tune the various elements of the RICH, the analytical estimation of the angle resolution of ALICE-HMPID has been revised and adapted and a new Monte Carlo program based on GEANT3 has been developed.

The single photon angular resolution (σ_θ) is expected to be affected mainly by the chromatic aberration of both the freon radiator and the quartz window, the uncertainty of the emission point in the radiator and the resolution of the position detector.

The analytical evaluation adopted a few simplifying assumptions: charged particle track perpendicular to the quartz window with speed $\beta = 1$, flat (rectangular) distributions for the dispersion relation $n(\lambda)$, for the emission depth in the radiator and for the position resolution of the detector.

These assumptions led to the expressions [46]:

$$\sigma_\theta^{p.e.} \sim \sqrt{(\sigma_{\rm CHR}^{p.e.})^2 + (\sigma_{\rm EMI}^{p.e.})^2 + (\sigma_{\rm LOC}^{p.e.})^2} \tag{5.3}$$

where

$$\begin{aligned}
\sigma_{\rm CHR}^{p.e.} &= \Delta\lambda \sqrt{0.0317 + \left[\frac{0.47\ w_q + 0.70\ w_g}{0.84\ w_f + 1.02\ w_q + 5.43\ w_g}\right]^2} \\
\sigma_{\rm EMI}^{p.e.} &= \frac{230\ w_f}{0.83\ w_f + 1.22\ w_q + 5.14\ w_g} \\
\sigma_{\rm LOC}^{p.e.} &= 1.72\ \sigma_{\rm EMI}\ \frac{L_{PAD}}{w_f}
\end{aligned}$$

Here the σ's are in mrad, while w_f, w_q and w_g (in mm) are the thicknesses of the radiator, quartz and gap respectively, $\Delta\lambda = 30\ nm$ is the wavelength window of detectable photons (convolution of the CsI Quantum Efficiency, and the freon transmittance) $L_{\rm PAD} = 8.2$ mm is the average linear pad size.

The angular resolution of the whole ring derives from $\sigma_\theta^{p.e.}$ by the relation $\sigma_\theta \sim \sigma_\theta^{p.e.}/\sqrt{N_{PE}}$ where $N_{PE} \sim N_0 w_f \langle \sin^2\theta_c \rangle$, is the number of collected photoelectrons. Here N_0, the quality factor of the detector, is estimated from tests performed by the ALICE-R&D26 group[46].

The previously described Monte Carlo simulates realistic Hall A hadron arm phase space, realistic optical characteristics and CsI Quantum Efficiency while the pad digitization is based on a gaussian charge production in the Multi Wire Proportional Chamber (MWPC in the following) which produces clusters of pads. The background and feedback photons in MWPC are not included in the simulation.

The simulated events are processed by a reconstruction algorithm based on a geometrical back-tracing approach: a transcendental equation relates the Čerenkov emission angle of the photon (θ_c) with the single photon hit position (cluster center of gravity), the track information (direction and momentum given by the other hadron harm detectors), the RICH detector geometry (fixed) and the emission point in the radiator (which must be assumed). This equation can be easily solved numerically giving θ_c for each photon hit; the angle assigned to each charged particle (the angle of the Čerenkov ring θ_c) is assumed to be the average of the $\theta_c^{p.e.}$ of all photon hits associated to the charged particle track.

Fig. 5.9 represents the angle distributions of the Čerenkov ring for π, K^+ and p for a C_6F_{14} thickness of 14 mm. The bottom histogram (the most realistic) shows that the angle resolution for the whole ring coming out from the Monte Carlo and the applied

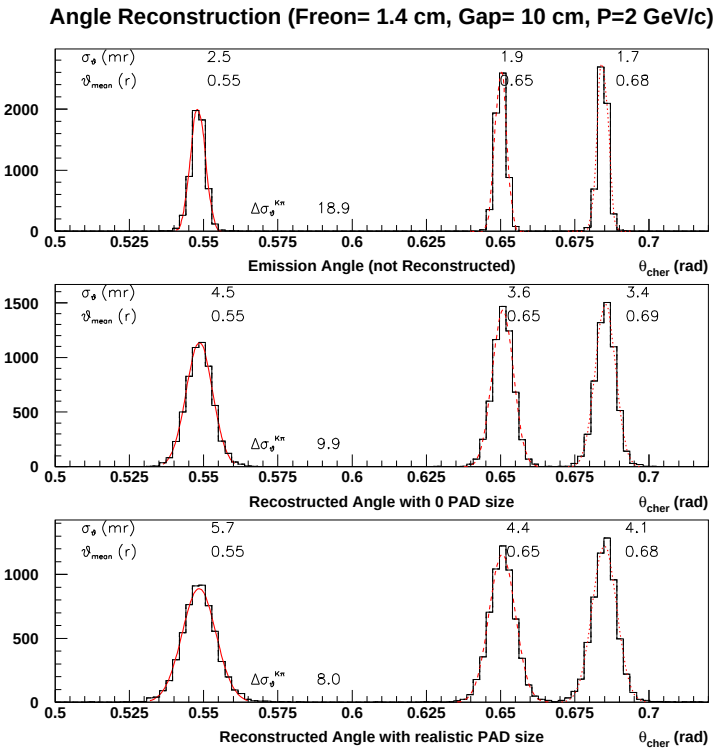

Figure 5.9: The Čerenkov ring angle distributions for protons ($\theta_{\rm cher} \sim 0.55$ rad), kaons ($\theta_{\rm cher} \sim 0.65$ rad) and pions ($\theta_{\rm cher} \sim 0.68$ rad) with equal populations. Top plot: GEANT3 generated angle (it takes into account the radiator chromaticity only); center plot: reconstructed angle with zero size pad (no position detector uncertainty); bottom plot: realistic reconstructed angle (real pad size).

reconstruction algorithm is 4.1 mr (for π).
The corresponding separation power between pions and kaons is $n_\sigma \simeq 7\sigma_\theta$.
Even keeping the conservative value of the Monte Carlo one gets a satisfactory small $\pi + p$ contamination on the kaon sample between 0.5 and 0.005 depending on the hypernuclear energy level, where the K^+ comes from. These values are orders of magnitude less than the present Hall A kaon ID contamination. The enormous work required to successfully bring on a RICH project in such short time (less than three years) should not have been done without the research and development of the ALICE-R&D26 group going on from several years.

5.2.2 Description of the Detector

The RICH has a proximity focusing geometry (no mirrors involved) which makes the detector compact (total thickness less than 50 cm), relatively thin (18% X_0) and unexpensive. Figure 5.10 shows the working principle of the adopted solution.

The Čerenkov effect takes place in the liquid C_6F_{14} when a charged particle crosses it. The liquid radiator, 15 mm thick, is housed in a vessel made of NEOCERAM[3] on all sides but the exit window which is made of pure quarz, 5 mm thick.

The Čerenkov photons, emitted along a cone surface, are refracted by the perfluorohexane (C_6F_{14}) - quartz - methane interfaces and strike a pad plane after travelling a proximity gap of 10 cm filled with pure methane.

The choice of the radiator is imposed by the momentum range ($1 - 3$ GeV/c) of the particles to be identified. A freon recirculating system provides a pure and stable liquid radiator; filtering and refilling stages keep under control the high solubility and volatility of the C_6F_{14} itself. The transparency of this radiator cuts out the photons with wavelength below 160 nm The photon detector is made of a Multi-Wire Proportional Chamber (MWPC), with one cathode plane replaced by a pad plane which allows the 2-dimensional localization of the photon hit. The pad plane is covered by a thin (300 nm) substrate of CsI which acts as photon converter. The emitted photoelectron is accelerated by an electrostatic field (2000 V/2 mm) between the pad plane and an anode wire plane in front of the pads, forming a MWPC.

While the anode wires collect the electron avalanche, the counterpart ions are collected by clusters of pads, each of which is connected to the input channel of a multiplexed sample and hold electronics, housed on the back of the pad plane. A drift electrode at 300 V, close to the quartz window, prevents from reaching the MWPC the electrons produced by ionization in the proximity gap by the charged particle. At the end of this process, the clusters of pads produced by the photons are scattered along a ring (ellipse) while one cluster coming from the charged particle track is located in the central region of the ring.

Table 5.3 presents a detailed list of the RICH components.

This size and Hall A hadron arm phase space constraint the gap length.

The CsI photon converter, coating the pad surface, offers advantages with respect

[3]The NEOCERAM is a glass-ceramic material with mechanical and thermal properties almost identical to the quartz ones.

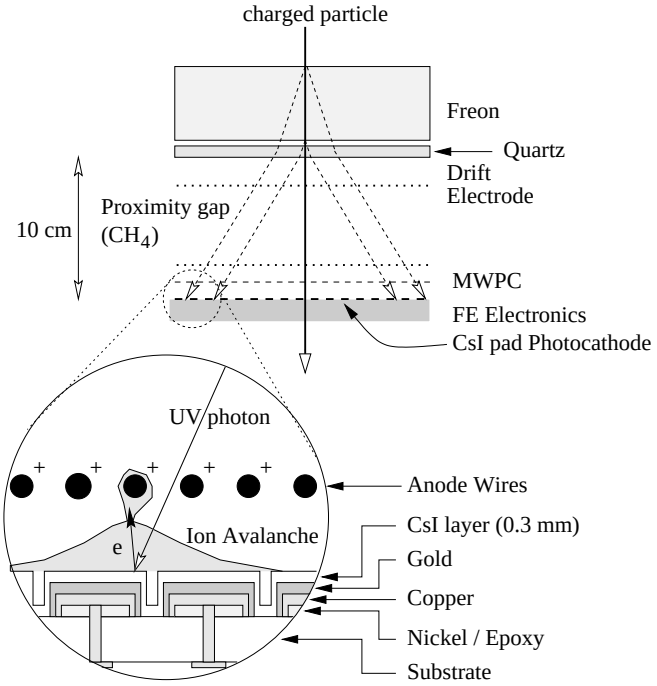

Figure 5.10: Working principle of the freon CsI proximity focusing RICH.

to its traditional competitors TMAE and TEA (room temperature operation, relatively easy handling, no MWPC aging, no expensive gas mixture) and affordable disadvantages (no long term experience and no on-line renewal). Since this part of the detector is crucial for the RICH performances, it is described in detail in the following subsection.

The readout electronics

The readout system of the 11520 pads is based on 720 ASIC CMOS front-end GASSIPLEX chips, each of which has 16 analog channels and one multiplexed analog output, 3 control input signals (T/H, RESET and CLK) and one TEST input signal. Each analog input channel consists of one charge-sensitive, low noise, preamplifier with a long integration time (of the order of 500 ns) and a track and hold (T/H) stage which stores on a capacitor the collected charge providing a charge to voltage convertion. The voltage of each channel is multiplexed in the GASSIPLEX output and presented to a fast ADC running at 2.0 MHz (CAEN CRAM system).
The GASSIPLEXes are combined in group of 3, that is the minimum multiplexed segment is 48 channels (one FE-segment). The RICH readout is equipped with 24 CAEN CRAMS ADC modules and two CAEN CRAM sequencers. One CRAMS module has two ADC inputs, each of which converts the output of 5 FE-segments (that is 240 channels), allowing a total digitization time of $T_d \sim 120$ μs.

The maximum readout rate (from the RICH pads to the DAQ computers, with 100% dead time) is the sum of T_d and the VME transfer time (T_{VME}) from the CRAMS to the DAQ computers; this time is affected by the number of long word (32 bit) to transfer

Table 5.3: Detailed list of the RICH components.

RICH size	$50 \times 210 \times 50$ cm^3
Optics	proximity focusing
Radiator	15 mm of liquid freon (C_6F_{14}) $n = 1.28$
Quartz window	5 mm, $n = 1.56$
Position detector	MWPC, with one cathode of pads, size: 1920×403 mm^2, anode wire pitch: 4.2 mm, anode-cathode gap: 2 mm, amplification gas: CH_4 at STP, operating voltage: 2 kV
Pad surface	3 pad planes, 640×403 mm^2 each; 11520 pads, 8×8.4 mm each
Photon converter	300 nm of CsI coating the pad surface
Electronics	analog, charge sensitive sample and hold, 11520 channels multiplexed in 48 ADCs

and the transfer speed over the VME bus. The CRAMS supports the zero suppression and pedestal subtraction, which reduce the number of long-words to transfer at about 50/event. The CRAMS - VME trasfer rate is 5 Mlong-word/s. In these conditions $T_{VME} \sim 10$ μs, that is about 10% of T_d

Therefore the maximum readout rate is about 1.5 kHz at 20% dead time (7.5 kHz at 100% dead time) and the event size few tens of long-word.

5.2.3 Photodetector, evaporator, QE measurements

A dedicated facility to deposit thin film of CsI on large area planes in vacuum condition, has been built in Rome by the INFN-Sanità group. It has been successfully tested (see 5.2.4) and transported to Jefferson Lab. It consists in a cylindrical stainless steel vessel (110 cm height, 120 cm diameter) equipped with four crucibles containing CsI (Fig. 5.11). The CsI is evaporated on the pad surface by the successful technique established and used by the ALICE-R&D26 group [46]. The prepolished pad plane, a printed circuit with 3 layers of metals (nickel, copper and gold, see Fig. 5.10) glued on the vetronite substrate, is housed in a vacuum chamber (10^{-7} mBar) heated at 60 ^{o}C, at about 1 m from four DC heated tungsten crucibles containing the pondered powder of CsI.

At the crucible temperature of ~ 500 ^{o}C all the CsI powder evaporates and a layer grows at the pad surface at a speed of about 2 nm/s; thus producing the desired CsI layer of 300 nm or so depth in about 150 s.

The obtained photocathode plane is maintained in the vacuum chamber at 60^{o}C for twelve hours of post-treatment (previously one day [46]) which has revealed useful for an enhancement of the photon conversion quantum efficiency (QE).

Since H_2O vapour reduces the performances of the CsI photon conversion, the photocathode must not be exposed to air. For this reason, the assembling of the pad

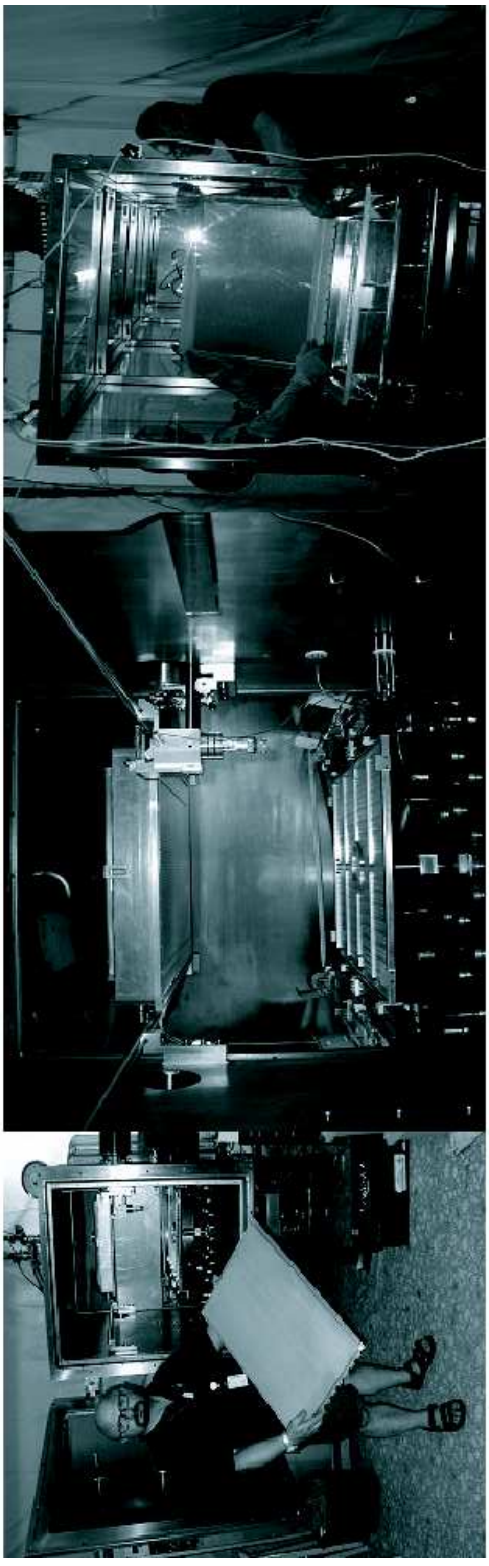

Figure 5.11: The evaporator and a photodetector frame with CsI deposition.

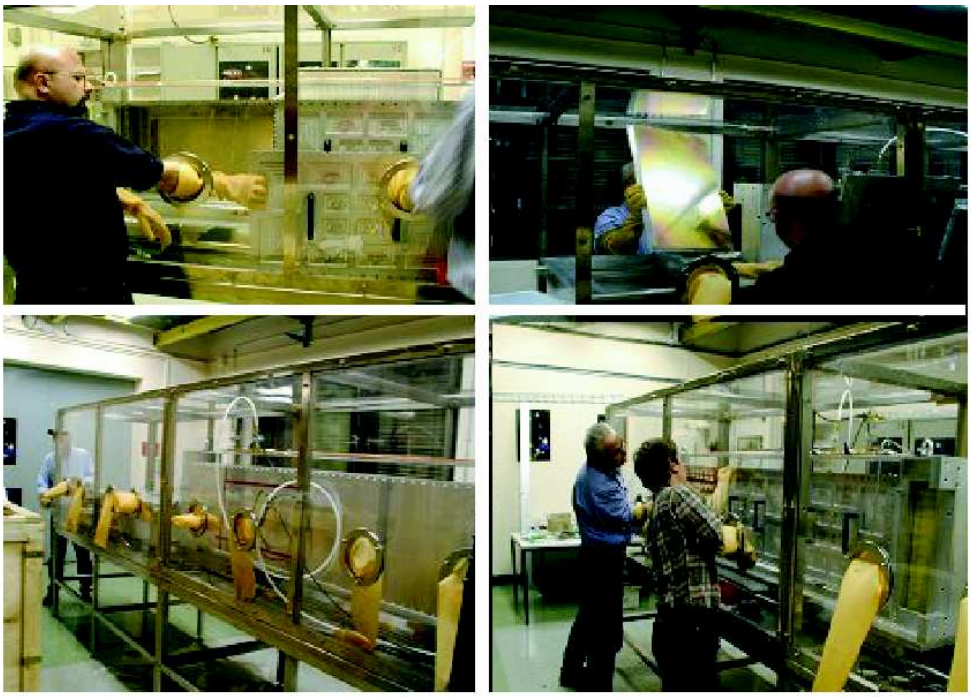

Figure 5.12: The glove box and the assembling of the photocathodes in the RICH.

planes in the RICH structure is done in argon atmosphere inside a large volume glove-box (Fig. 5.12).
Evaporations of CsI thin films have been performed many times since 2001 with performances as good as expected. It has been proven that particular cleaning procedure of the pad surface before the CsI deposition allow better performances [46]. In order to verify the good quality of the evaporation and its uniformity on the large pad surface, an on-line Quantum Efficiency (QE) measuring system has been developed and successfully employed [20] (see Fig. 5.13). A movement system allows to map out the whole photocathode. A deuterium lamp is used as UV light source. The light beam is split using a semitransparent mirror to allow monitoring the lamp emission by measuring the current from a photodiode. Three narrow band filters, selecting three different wavelengths in the region where the CsI is photosensitive (160 nm, 185 nm and 200 nm), are employed. The UV beam is sent, through a rotable mirror, to the photocathode or to a reference PMT. The photocurrent (of the order of nA), generated by electrons extracted from the CsI film, is detected on a small specific wire chamber. Fig. 5.14 shows the typical results of the measurements compared with the extrapolation from the in-beam results.
Starting from June 2001, the CsI deposition has been performed several times, the QE measurements showed that the procedure has a good reliability, only $\sim$ 15% of the depositions showed an average QE lower than 80% of the curve in Fig. 5.14 or with more than one pad with a QE lower that 30 % of the average value (Fig. 5.15).

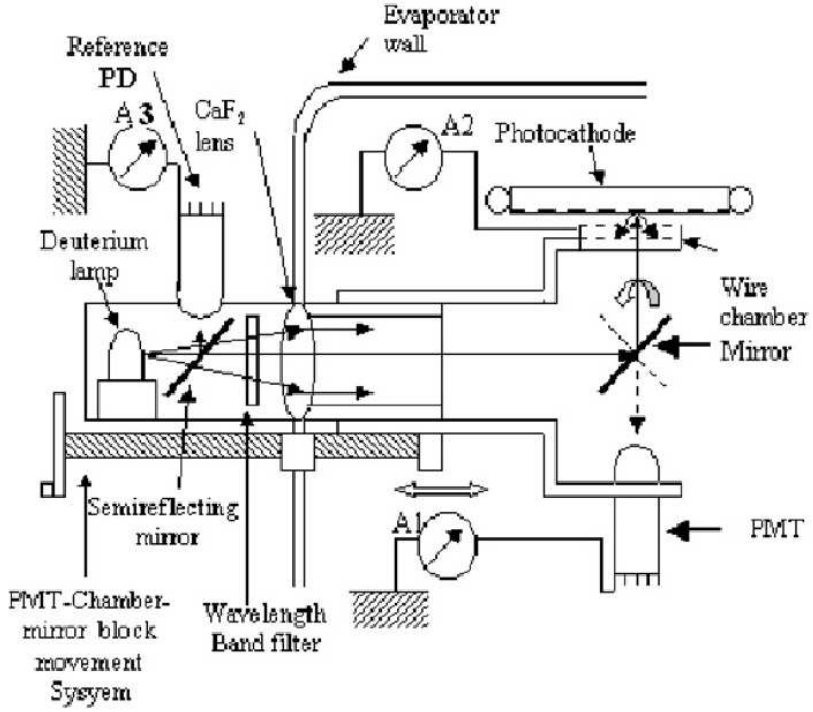

Figure 5.13: The Quantum Efficiency measurement system.

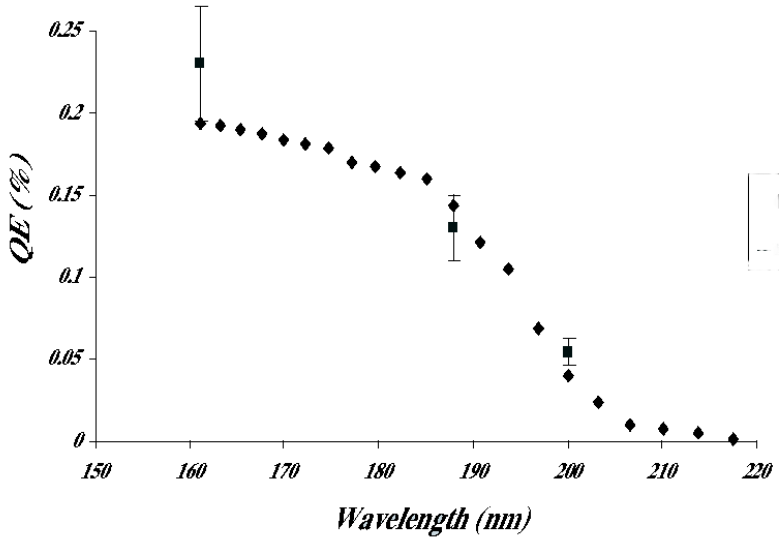

Figure 5.14: The typical results of the QE measurements at three wavelengths (160 nm, 175 nm, 200 nm, points with error bars), compared with the extrapolation from the in-beam results (diamonds).

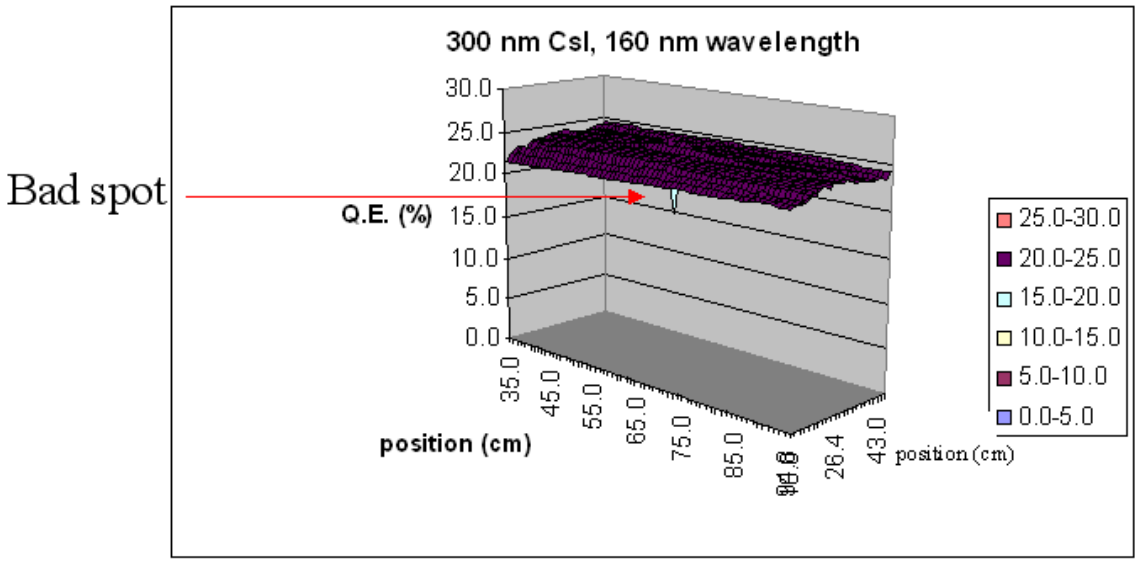

Figure 5.15: Map out of the QE (at 160 nm) on a whole photocathode. In this example a bad-quality pad is detected.

5.2.4 CERN tests

The RICH has been built in Italy. Before the operation in Jefferson Lab, the detector has been tested in T7 PS test beam area at CERN (Fig. 5.2.4). The test has been performed with a 4-GeV π spot beam directed perpendicularly to the detector plane. The results were very satisfactory: an average number of 12.44 photoelectrons were obtained, and an angular resolution of $\sigma_\theta = 3.7\ mrad$ (see Fig. 5.17). A test has been made for the evaporation of the CsI. The CsI deposition (so-called 'evaporation') on one photocathode was performed in Rome, the other two at CERN. We obtained the same results (number of photoelectrons), confirming the good quality of the photodetector prepared in Rome.

5.2.5 Results

The RICH worked successfully during the experiment, providing a big improvement in the particle identification. Detector in-beam commissioning has been performed before starting the real data taking. Fig. 5.18 shows the RICH performance at the operating conditions during the experiment. The top-left plot is the charge distribution of the MIP, the top-right plot is the charge distribution of single photoelectron. One ADC channel corresponds to 0.15 fC charge. The mean value of the MIP signal is determined by fitting the distribution with a Landau function, expected for a Multi-Wire chamber in proportional regime. The lower part of the single-photoelectron signal is removed by the zero-suppression threshold of the ADCs and therefore its digitized distribution, similar to a gaussian tail, has to by fitted with a Furry function (exponential behaviour) in order to extract the mean value [46].

Combining the information of the two fits we determined the gain value of $\sim 5 \times 10^4$

Figure 5.16: The RICH in the T7 PS test beam area at CERN.

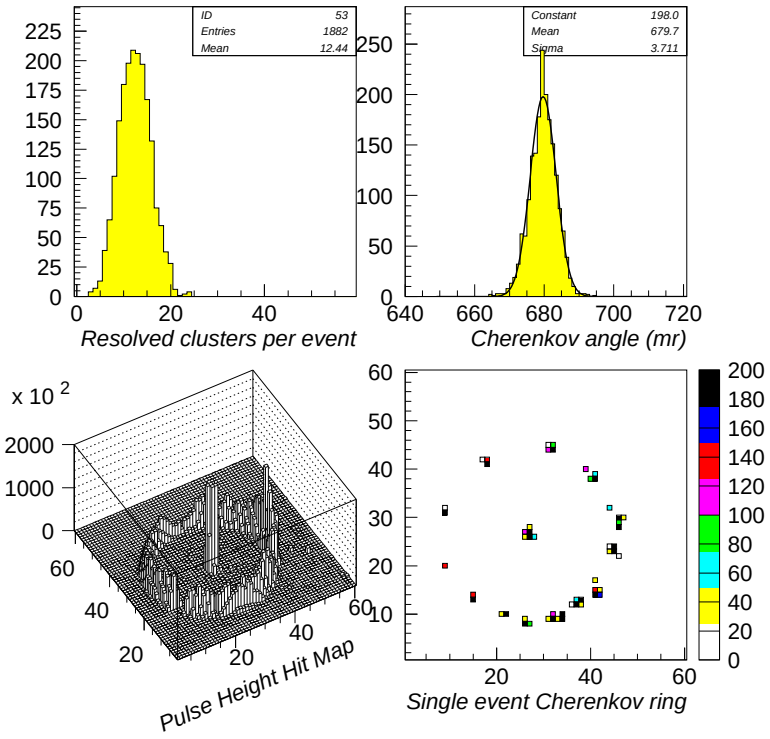

Figure 5.17: The results of the CERN tests: the number of resolved clusters, the angular resolution, the rings.

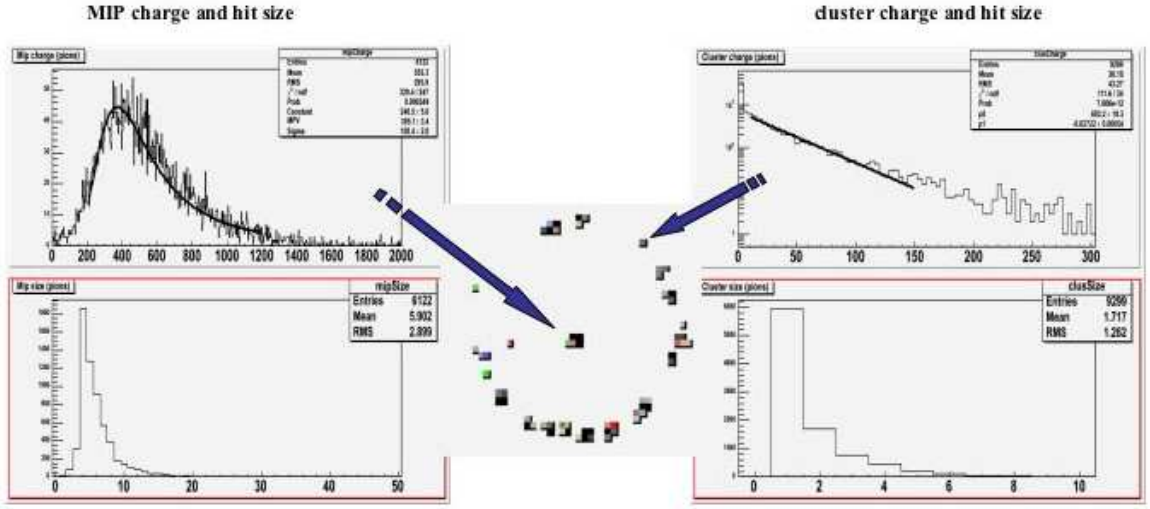

Figure 5.18: RICH basic parameters in the operating conditions (HV=2100 V, grid voltage=250 V).

for the MWPC. The two bottom plots show the size of the charge distribution, as number of pads containing the signal, for the MIP (left) and the single photoelectron (right). In Fig. 5.19 the key parameters are reported: the number of clusters for pions and proton and the pion Čerenkov angle reconstruction. Fig. 5.20 shows the basic performance for two different High-Voltage sets of the MWPC. A full high-voltage scan between the two values in the figure has been performed. The higher High-Voltage gives better performances (the MWPC has higher gain improving the signal. The HV should be high enough to reach the maximum gain (affecting the angular resolution), but still not so high to generate substantial photon-feedback background [21].
The stability of the basic parameters was continuously monitored on-line (number of clusters per event and MIP detection efficiency)
Fig. 5.21 shows the fundamental role of the RICH in identifying the kaons. After the kaon selection (details about the kaon selection are in chapt. 7) on the two aerogel threshold detectors (AERO1 and AERO2 in the following) a significant number of pions is still present. The RICH allows to get rid of this residual contamination.
A number of p.e. equal to 13 has been measured for pions. The angular resolution is $\simeq 5\ mrad$, corresponding to a separation between π and k of $\simeq 6\ \sigma$. This result, compared with the Monte Carlo simulations, is in the expectations.
Fig. 5.22 shows how the RICH cleans up protons and pions in the Time-of-Coincidence spectrum (see chapt. 6). Fig. 5.23 shows that a pion rejection factor as high as 1000 is obtained. One should note that the RICH analysis software can still be optimized.
We can conclude that the RICH detector has performed very well, allowing "unambiguous" kaon identification.

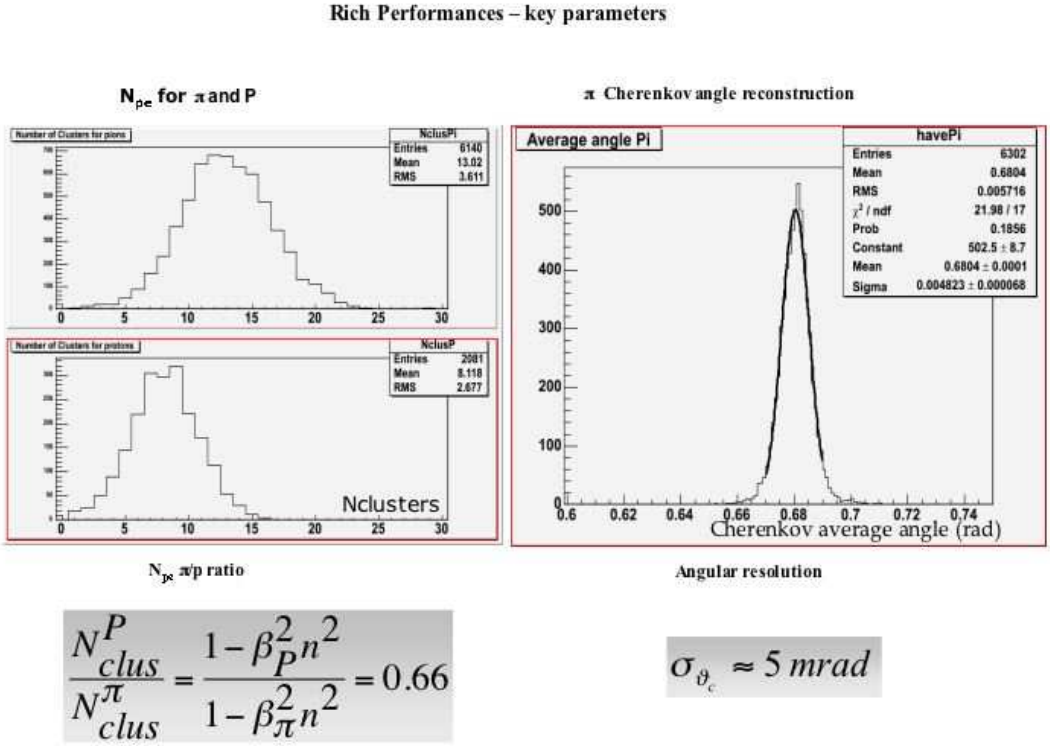

Figure 5.19: The RICH key parameters.

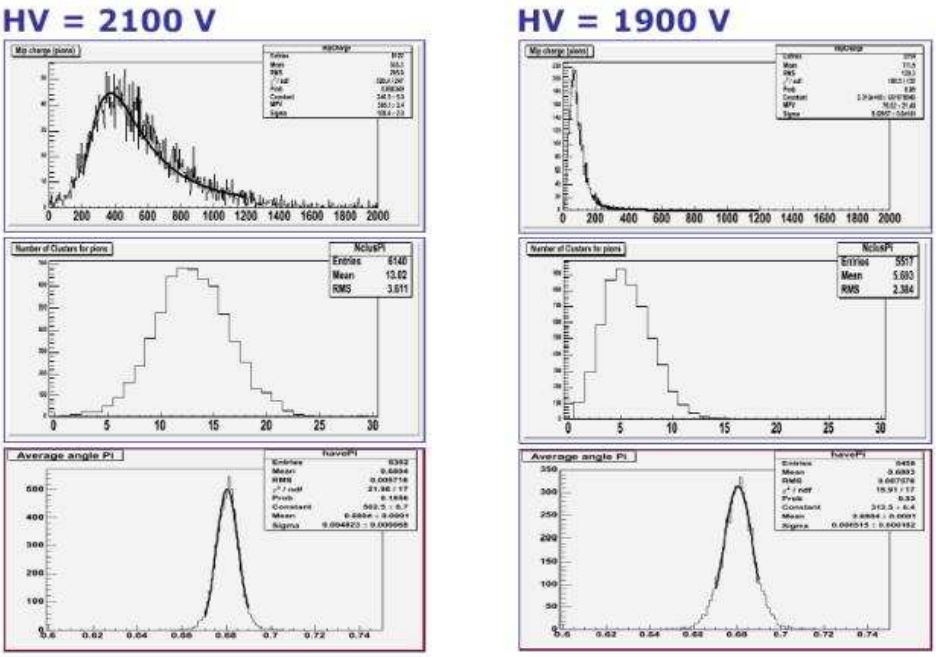

Figure 5.20: The pulse height from the ionized-particle signal, the number of resolved clusters and the angular resolution for π^+, for two different High-Voltage sets of the MWPC.

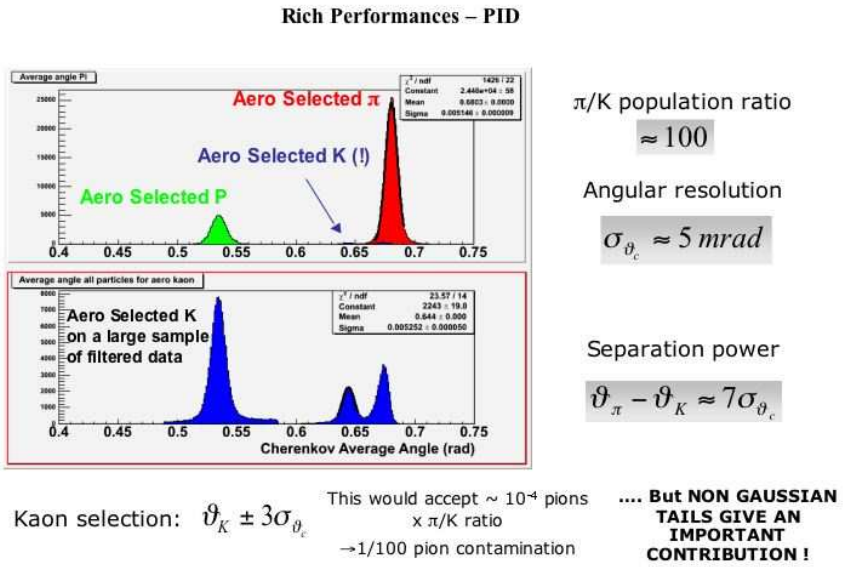

Figure 5.21: The Čerenkov angle distributions for protons ($\theta_{\text{cher}} \sim 0.54$ rad), kaons ($\theta_{\text{cher}} \sim 0.64$ rad) and pions ($\theta_{\text{cher}} \sim 0.68$ rad).

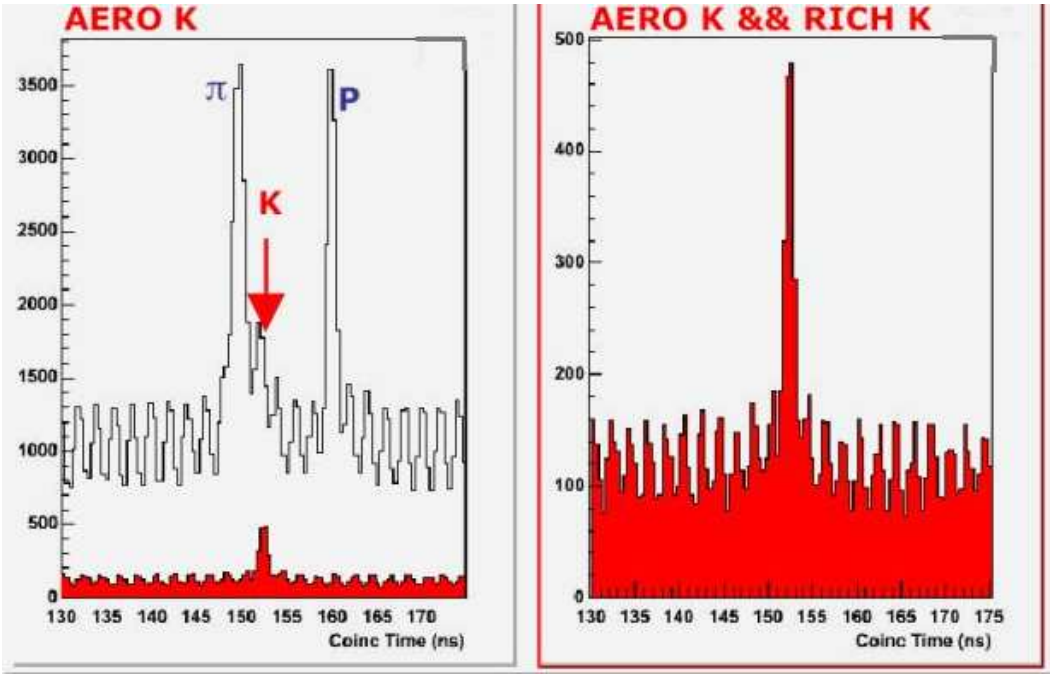

Figure 5.22: The RICH kaon selection of the TOC Spectrum. The contamination is clearly reduced to a negligible term.

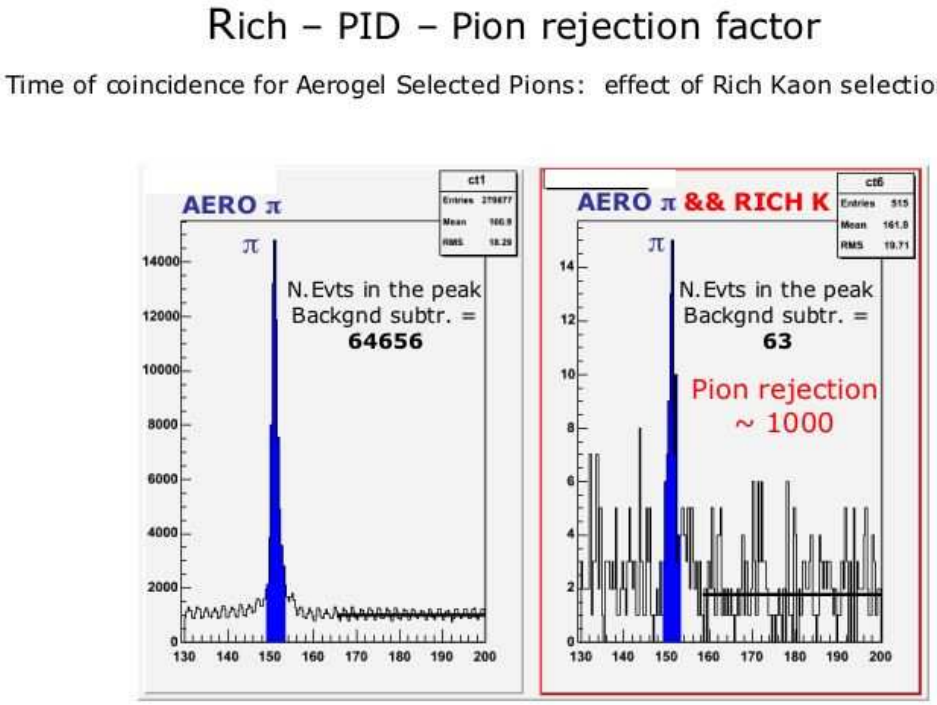

Figure 5.23: The RICH pion rejection power on the TOC spectrum.

Chapter 6

Data Analysis

6.1 Missing Energy Reconstruction

The missing energy is the key variable to determine the Excitation Energy Spectrum, the excitation energy is directly related to the missing energy, that is a calculated variable in the Analysis.
Indeed the usual definition of missing energy is

$$E_{miss} = \omega - T_K - T_x = m_K + M_x^* - M_A \tag{6.1}$$

where M_A and M_x^* are the mass of the target and the mass of the residual respectively. The missing energy is computed by

$$E_{miss} = m_K - M_A + \sqrt{(\omega + M_A - E_K)^2 - (\overrightarrow{q} - \overrightarrow{p_K})^2} \tag{6.2}$$

Considering the X system being the hypernucleus, we have for M_x^*:

$$M_x^* = M_A - m_p + \epsilon_p + m_\Lambda - \epsilon_\Lambda \tag{6.3}$$

where ϵ_p and ϵ_Λ are the (positive) binding energies for the proton removed from A and the hyperon bound in the hypernucleus, respectively. Hence for the missing energy we will have:

$$E_{miss} = m_K + M_x^* - M_A = m_K + m_\Lambda - m_p + \epsilon_p - \epsilon_\Lambda. \tag{6.4}$$

Therefore the missing energy differs from the excitation energy just for a constant. The quantity $m_K + M_\Lambda - M_p = 671\ MeV$ is subtracted in all the missing energy plots presented in this thesis (for example Fig. 6.1), thus we consider the missing energy as $\epsilon_p - \epsilon_\Lambda$ in the following.
Since the physics information is in the (e, e', K^+) real coincidences, the analysis has been performed to select these events.

6.1.1 The $(e, e'K^+)$ real-coincidence selection

Event selection on Gas Čerenkov detector

The selection of e^- is based on the Gas Čerenkov detector. Since the energy deposition in the matter from an electron is larger than the energy deposition from a pion, a cut in

the Gas Čerenkov spectrum (see Fig. 6.14), the selection corresponds to the rejection of events with smaller pulse height.
In the presented analysis the cut corresponding to the electron selection keeps only the events with pulse height higher than 200 ADC channels.
Using a cross-check with the Lead Glass counters, it has been shown that the applied selection on the Gas Čerenkov detector has a small pion contamination [47], assumed negligible for the presented state of the analysis.

Event selection on Aerogel Čerenkov detectors

In the aerogel Čerenkov detector with refractive index of 1.015 (AERO1) only pions are over the threshold for the Čerenkov effect. Therefore, AERO1 is used as veto: only the events below a desired pulse height are selected.
In the presented analysis only the events with pulse height smaller than 10 ADC channels are selected. In the aerogel Čerenkov detector with refractive index of 1.055 (AERO2) both pions and kaons are over the threshold for the Čerenkov effect, but not protons. The pions, having higher speed than kaons, generate an larger quantity of Čerenkov light, therefore the events with higher pulse height are identified as pions.
In the presented analysis only the events with pulse height larger than 20 ADC channels and smaller than 1200 ADC channels are selected.

Event selection on the RICH

Since in the analysis the kaon identification is performed using the combined response of both the RICH and the aerogel detectors, we have used a loose kaon RICH selection, in order to avoid large inefficiencies.
The event selections on the RICH detector in the presented analysis is defined as:

- $L = 25\ mrad$ (see chapt. 10),
- number of clusters higher than three,
- $\chi^2_k < 4 \times \chi^2_\pi$ (see chapt. 10),
- $0.624\ rad < \theta_{Ch} < 0.660\ rad$.

Event selection on the Coincidence Time

The Coincidence Time (CT) is the time distance between the signal on a scintillator (S1 or S2) on a spectrometer arm and the corresponding scintillator signal on the other spectrometer arm.
The CT spectrum shows peaks corresponding to the real coincidence between electrons (or π^-) and p, π^+ and k (see Fig. 5.22), while the random coincidences (accidentals) are distributed uniformly. The distribution of the accidentals is not flat, but it is evident a structure showing a series of peak with a periodic distance of $\simeq 2\ ns$ (Fig. 7.1), corresponding to the beam structure.
Due to the higher background of π^+, the peak of the real $(e, e'K^+)$ is not visible if the

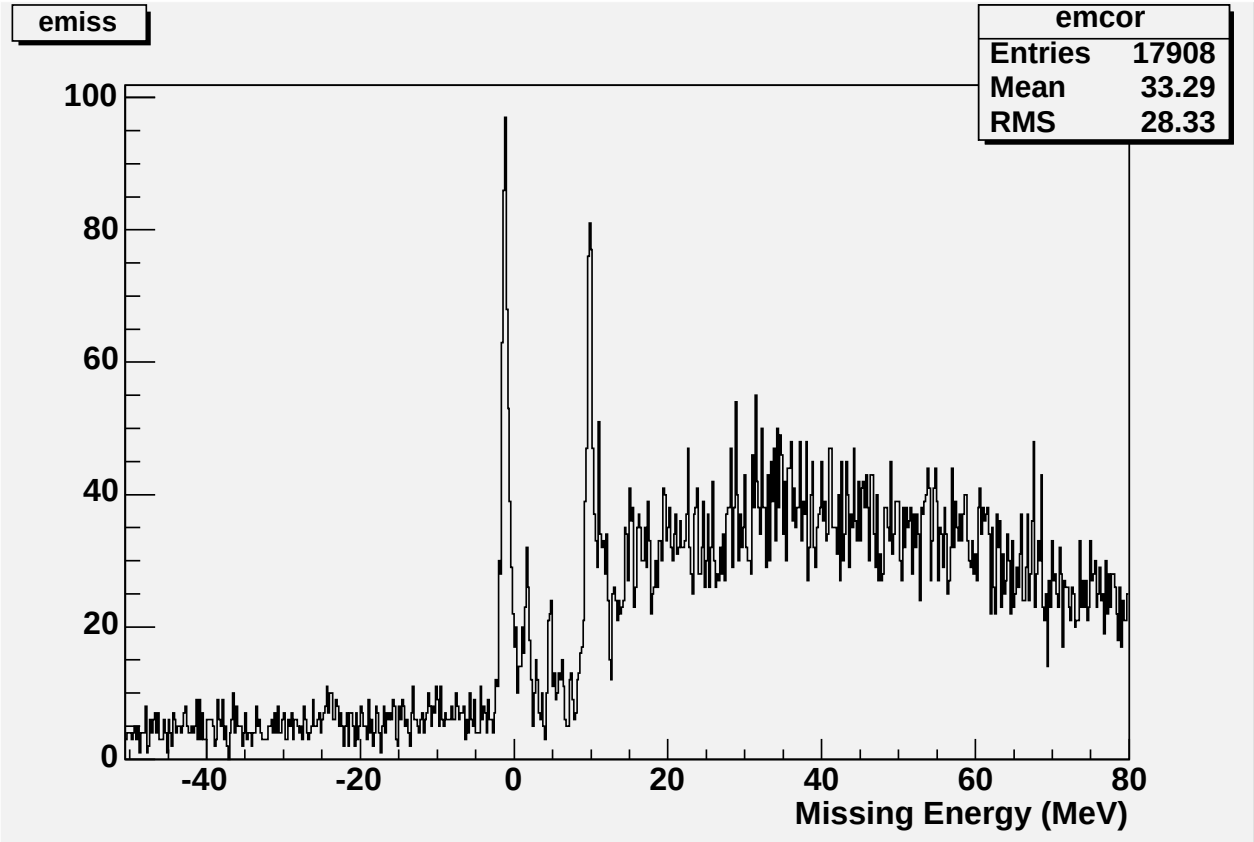

Figure 6.1: The missing energy spectrum for $(e, e'K^+)$ coincidences on Carbon target.

kaon selection on aerogel Čerenkov detectors and RICH detectors is not applied.
In the presented analysis we consider the CT as the difference between S2 on the Left Arm and S2 on the Right Arm, only the events in a time window width of ± 1.0 ns respect to the real kaon coincidence peak are selected.

The energy resolution

Since the resolution is critical for the experimental results, the best computation of all the terms involved in the calculations of the missing energy have to be as precise as possible. Therefore:

1. the optics database for both the arms of the spectrometers has to provide the best momentum resolution, possibly in an acceptance range as larger as possible,

2. the beam energy spread has been continuously monitored using OTR and SLI (see Chapt. 4), to exclude the events when the beam energy spread was not good ($\sigma_E/E > 2.5 \times 10^{-5}$).

3. the central beam energy has been continuously monitored, to compute the real energy to the incident electrons.

4. in case of rastered beam, it is used a software procedure to evaluate the real position of the incident electrons, to correctly compute the entrance position of

Contribution	Energy resolution
Beam	5.9×10^{-5} of 4 GeV $\rightarrow$ 236 keV
Electron momentum	10^{-4} of 1.8 GeV $\rightarrow$ 180 keV
Kaon momentum	10^{-4} of 2.0 GeV $\rightarrow$ 200 keV
Kaon *Straggling*	40 keV
Total	$\sim 360\ keV$

Table 6.1: The contributions to the energy resolution (FWHM).

the particles in the spectrometers and thus the momentum,

5. after applying the corrections mentioned above, a check of the residual correlation between the missing energy and the optics variables was performed.

The different contributions to the energy resolution are in Table 6.1.

6.2 ROOT/C++ Analyzer for Hall A

The raw data consist of CODA (CEBAF On-line Data Acquisition system, the standard data acquisition for the Hall A) and EPICS (Experimental and Physics Industrial Control System, the slow controls) formatted events.
The Hall A ROOT/C++ Analyzer (simply the Analyzer in the following) is the software package used for the physics analysis. It is based on ROOT/C++ [44], the analysis framework designed at CERN by R. Brun and F. Rademakers. The "standard analyzer" provides a generic event loop and analysis chain that are sufficient for most physics analysis purposes. The event loop and high-level algorithm are implemented in the method 'THaAnalyzer::Process()' of the class 'THaAnalyzer'. The standard spectrometer processing algorithm is implemented in the method 'THaSpectrometer::Reconstruct()' of the class 'THaSpectrometer'.
The desired cuts and variables are easily defined into Analyzer using proper configuration files, the output is a ROOT file containing the 'ROOT Tree', the 'tree' of the events with the requested variables and cuts). In the "ROOT Tree", all of the desired variables are available, included the missing energy. Therefore, after doing the event loop on the raw data, the final analysis is performed into the ROOT framework. This procedure has the clear advantage of being performed into a very powerful and largely known tool.

6.3 Optics Analysis

The Hall A High Resolution Spectrometers (HRS's) are an identical pair of QQDQ magnetic spectrometers with optical properties that are point-to-point in the dispersive direction.
In order to evaluate the momentum resolution of HRS, we have performed, in June 2002, a test of $(e, e'p)$ reaction on ^{12}C thin (0.51 mm thick) target. Vacuum connection between the scattering chamber and the first quadrupoles of HRS's was established, so

Contribution	Energy resolution
Beam	11.8×10^{-5} of 4.7 GeV $\rightarrow$ 554 keV
Electron momentum	9.4×10^{-4} of 3.8 GeV $\rightarrow$ 357 keV
Kaon momentum	1.4×10^{-4} of 1.4 GeV $\rightarrow$ 198 keV
Kaon *Straggling*	211 keV
Total	$\simeq 720\ keV$

Table 6.2: The contributions to the energy resolution (FWHM). from the June-2002 test.

degradation of the energy resolution from the windows is avoided. Tab. 6.2 shows the measured beam energy resolution and the deduced spectrometers momentum resolution, taking into account the used kinematics, from the energy resolution of 720 keV which has been obtained. From this result, we could easily extrapolate an energy resolution of $\sim 350\ keV$ in the kinematical conditions of our experiment.
The optics database is a set of matrix elements defining the transport tensor which links the coordinates measured at the focal plane of the spectrometers with the angular and spatial coordinates at the target and with the momentum. A detailed description of the coordinate systems used is given in [45]. The relationship between the focal plane and target coordinates can be written (in a first-order approximation) as:

$$\begin{pmatrix} \delta \\ \theta \\ y \\ \phi \end{pmatrix}_{tg} = \begin{pmatrix} <\delta|x> & <\delta|\theta> & 0 & 0 \\ <\theta|x> & <\theta|\theta> & 0 & 0 \\ 0 & 0 & <y|y> & <y|\phi> \\ 0 & 0 & <\phi|y> & <\phi|\phi> \end{pmatrix} \begin{pmatrix} x \\ \theta \\ y \\ \phi \end{pmatrix}_{fp}$$

More generally the transport tensor elements are expanded in power of the variable at the focal plane, all the polynomial coefficients represent the optics database.
Indeed, for each event, two angular coordinates (θ_{det} and ϕ_{det}) and two spatial coordinates (x_{det} and y_{det}) are measured at the focal plane. The position of the particle and the tangent of the angle made by its trajectory along the dispersive direction are given by x_{det} and θ_{det}, while y_{det} and ϕ_{det} give the position and tangent of the angle perpendicular to the dispersive direction.
These observables are used to calculate x, θ, y, ϕ, and $\delta = \Delta p/p$ (the relative variation respect to the spectrometer central momentum) for the particle at the target.
To reduce the number of unknowns at the target to four, the x_{tg} value was effectively fixed at zero during the optics calibration by requiring that the beam position on target was within 250 μm of the origin of the HCS. The Transport Tensor links the focal plane coordinates to the target coordinates.
We describe here the procedure used to determine the matrix elements of the optics database (database optimization) and the results obtained for the E94-107 setup.
The starting point for the database optimization are sets of data from elastic scattering (on thin ^{12}C targets). Several open collimator measurements (typically five) are performed at $\Delta p/p$ values varying from -4.5% and +4.5% of the spectrometer central momentum, so that the elastic peak moves across the focal plane.
To optimize the reconstruction of the angular coordinates, a particular collimator called sieve slit is used. The sieve slit is positioned behind the target, with 49 holes of different size in well-defined x_{sieve} and y_{sieve} positions (see Fig. 6.3).

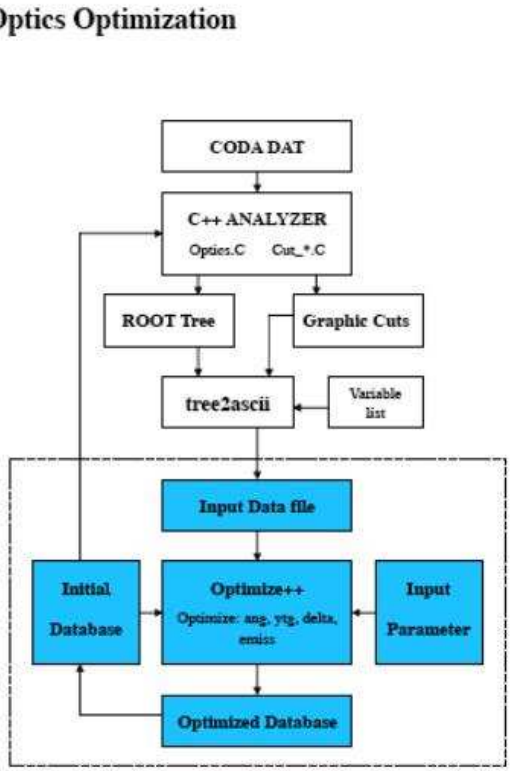

Figure 6.2: Description of the optics optimization process.

An iteration procedure, based on a specific code, is performed in order to obtain the best matrix elements for the optics database. The flow chart in fig. 6.2 shows how the optimization code works. The input data for the optimization code are supplied by Analyzer.
Optics matrix elements for both spectrometers have been optimized over the full ranges before the insertion of the septum magnets. The E94-107 setup is the first optimized setup with (both) the septum magnets. In practice, the expansion of the focal plane coordinates is performed up to the fifth order.
This optimization has been performed for the normal tune of the HRS pair. The spectrometer tune, and hence spectrometer optics, is very sensitive to the ratio of the magnetic field in the Dipole to the magnetic fields in the second and the third quadrupoles (Q2 and Q3). In order to ensure that normal tune of the spectrometer, Q2 and Q3 have to be cycled using the prescribed procedure.

For the E94-107 experiment, not only a optimization of θ and ϕ reconstruction is important, but even more important is the optimization of δ reconstruction, directly related to the momentum resolution of the spectrometers.
A optics data set was taken on December 2003 at the same spectrometer setting of the experiment. The results of the δ optimization for the E94-107 is the best ever obtained, corresponding to a momentum resolution of $\delta p/p = 1.8 \times 10^{-4}$ for the left arm (see fig. 6.5) and $\delta p/p = 1.6 \times 10^{-4}$ on the right arm. Selecting the central hole of the sieve slit, a resolution of 1.4×10^{-4} can be obtained on both arms, compatible with

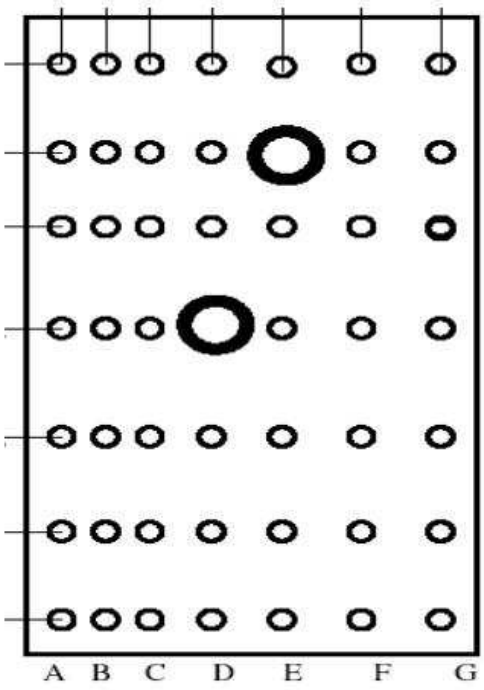

Figure 6.3: Sieve slit: The large holes allow for a unambiguous identification of the orientation of the image at the focal plane.

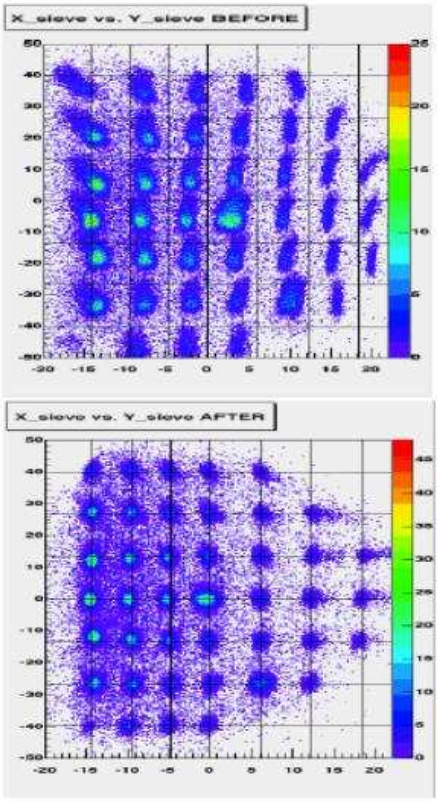

Figure 6.4: The image of the sieve slit with old database and with the new optimized database for the E94-107 setup. The presented image is reconstructed from the right arm, symmetric reconstruction is obtained from the left arm.

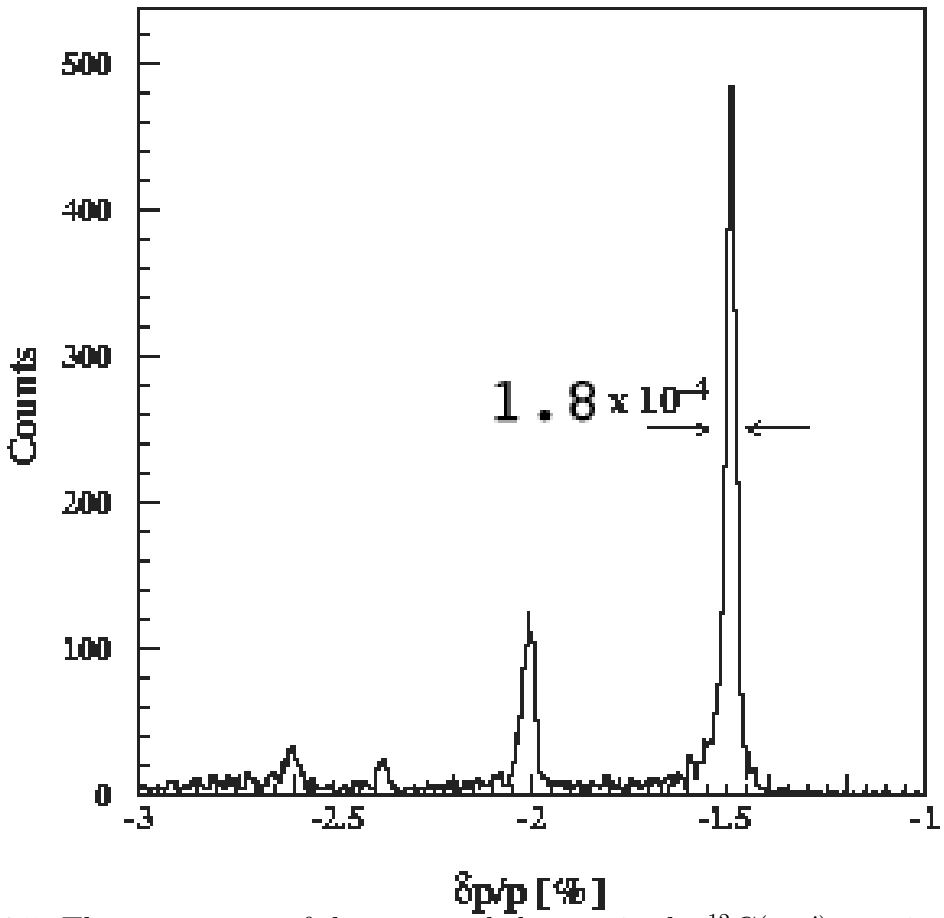

Figure 6.5: The momentum of the scattered electron in the $^{12}C(e,e')$ reaction detected on the left arm, indicating a FWHM of 1.8×10^{-4} at $\Delta p/p = -1.5\%$.

the expectations for the HRS spectrometers [39]. New optics data without the sieve slit was taken after the E94-107 data taking in April, with the specific goal of the δ optimization, still in progress.

6.4 Detector acceptances, correction factors, and normalization

At this preliminary stage of the analysis, all the efforts have been focused on the extraction of the hypernuclear excitation energy and on its energy resolution optimization. In order to give a first rough estimate of the cross section for each individual hypernuclear excitation level, the spectrometer acceptance has been computed, as well as all the correction factors accounting for the inefficiencies of the various detectors, deadtime, kaon decay probability, etc.
The estimate of the cross section, for a level i, is computed as

$$\sigma_i = \frac{N_i}{l \; surv(k)\epsilon_e\epsilon_H\epsilon_{coinc}\Delta\Omega_e\Delta\Omega_k\Delta p_e} \tag{6.5}$$

where

- N_i is the number of events in the level i corrected for the deadtime,
- l is the luminosity,
- $surv(k)$ is the kaon survival probability,
- ϵ_e and ϵ_k are the detector efficiencies for the two HRS arms,
- ϵ_{coinc} is the coincidence trigger efficiency,
- $\Delta\Omega_e$ and $\Delta\Omega_k$ are the HRS geometric acceptances for the two arms,
- Δp_e is the momentum acceptance for electrons.

Since we consider bound states, p_k and p_e are correlated and the cross section is integrated on all the range of Δp_k. The check that the whole range of Δp_k is within the spectrometer acceptance (spectrometer matching) has been checked for the $^{12}B_\Lambda$ ground state. (see par. 6.4.1).

6.4.1 Spectrometer acceptance

This experiment uses thin flat targets. Therefore the calculation of the solid angle acceptance is much easier with respect to experiments using liquid and gaseous extended targets. The spot size of the beam on target is very small, ~ 100 μm, only in the case of the Beryllium the beam was rastered in order to not damage the target. The spot size was 0.5×0.5 mm^2, small enough to give only very small geometric corrections to the solid angle acceptance.

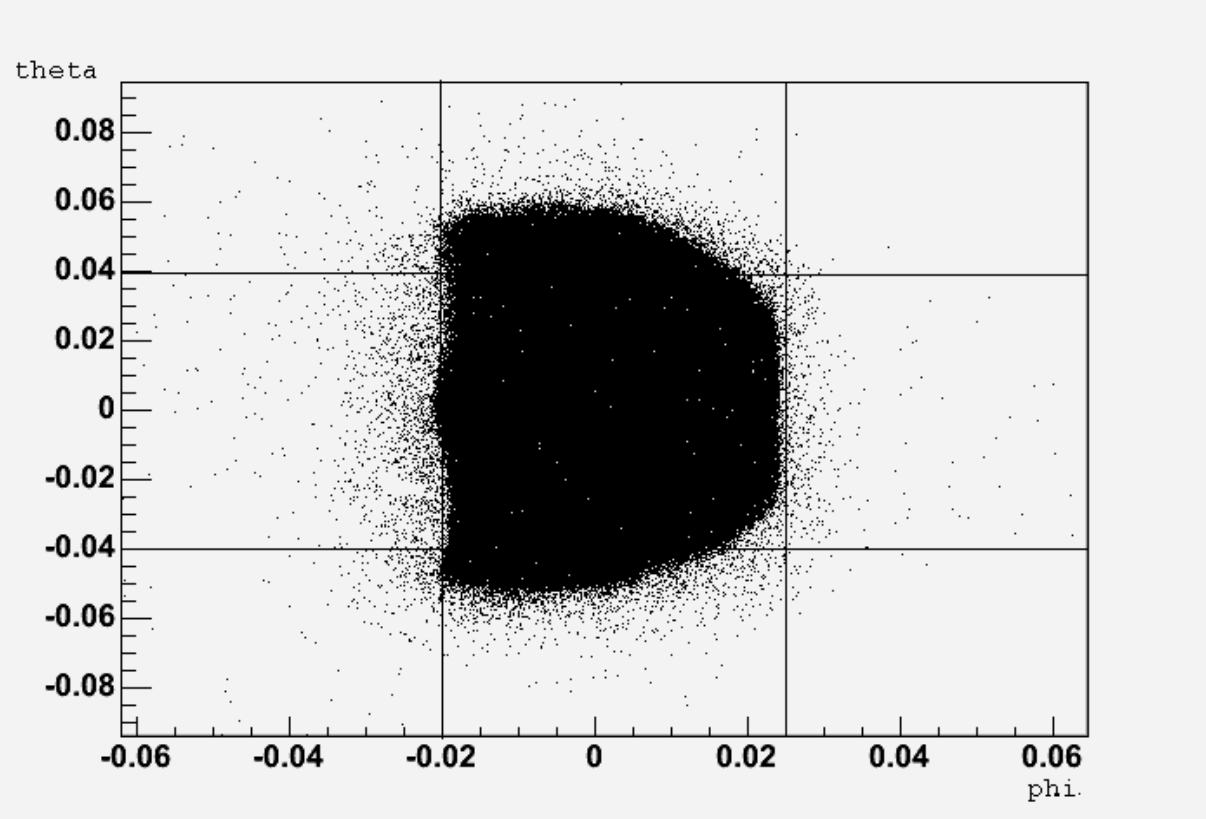

Figure 6.6: The angular acceptance in the Left Arm, θ (rad) as function of the ϕ (rad).

The evaluation of the cross sections should have to take into account the cuts on the momentum acceptance. The selected angular acceptance in the presented analysis is ± 0.03 rad for the dispersive angle θ, the selected range for the scattering angle ϕ is $-0.25 - 0.2$ on the Right Arm and $-0.2 - 0.25$ on the Right Arm. The analysis was performed with different selection on the momentum acceptance. We consider as full acceptance the range within $\pm 4\%$ of the central momentum, where only the edges are excluded from the event selection (Fig. 6.8). In this way the spectrometer matching is keeped (see Fig. 6.9).

6.4.2 Kaon decay probability

The kaon survival probability has to be taken into account. Indeed the (central) kaon momentum was 1.96 GeV/c. The path length of the central trajectory from the target to the origin of the Detector Coordinate System [45] is 24.18 m. To be correctly detected, a kaon has to reach the RICH detector (located behind the aerogel Čerenkov detectors), at a distance of 2.40 m from this point. The decay correction is given by the well-known survival probability law, in our case it correponds to a kaon survival probability of

$$P_k(x) = e^{-\frac{x}{\gamma c \tau}} = 17.5\% \tag{6.6}$$

where

- x is the kaon path length,

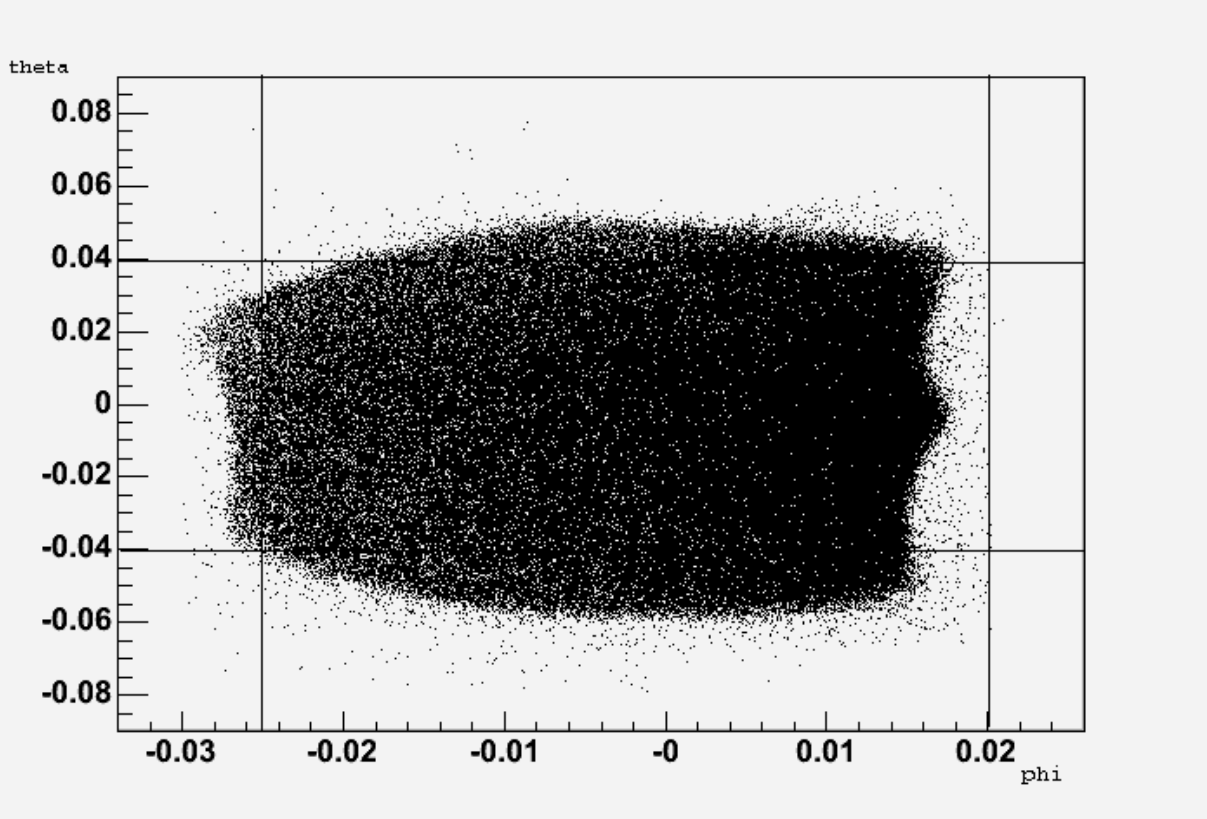

Figure 6.7: The angular acceptance in the Right Arm. Angles are in rad.

- γ is the relativistic term E/p,

- τ is the kaon life time ($c\tau = 3.71\ m$).

The path length of different trajectories to the origin of the Detector Coordinate System ranges between 23.8 m and 24.6 m (see Fig. 6.10). The distance to the RICH detector has to be added for the evaluation of the kaon survival probability. Small corrections on an event-by-event basis, due to the path lengths of the different trajectories, will be taken into account in the final analysis. Additionally, one needs an accurate estimate of the fraction of kaon events for which the decay product were still able to mimic a kaon trigger, in order to avoid overcorrections. The kaon survival probability for different trajectories ranges between 16.9% and 17.8% (fig. 6.11).

6.4.3 Deadtime correction

Two deadtime corrections have to be made: an electronic deadtime correction and a computer deadtime correction.
Electronic deadtime is due to the finite time duration (τ) of the electronic signals. If two independent pulses arrive at the electronics within a time interval shorter than τ, then only the first pulse is processed.
The computer deadtime refers to events not being recorded due to the fact that the data acquisition system can process at most one event within $\sim 200\ \mu s$. The duration of the

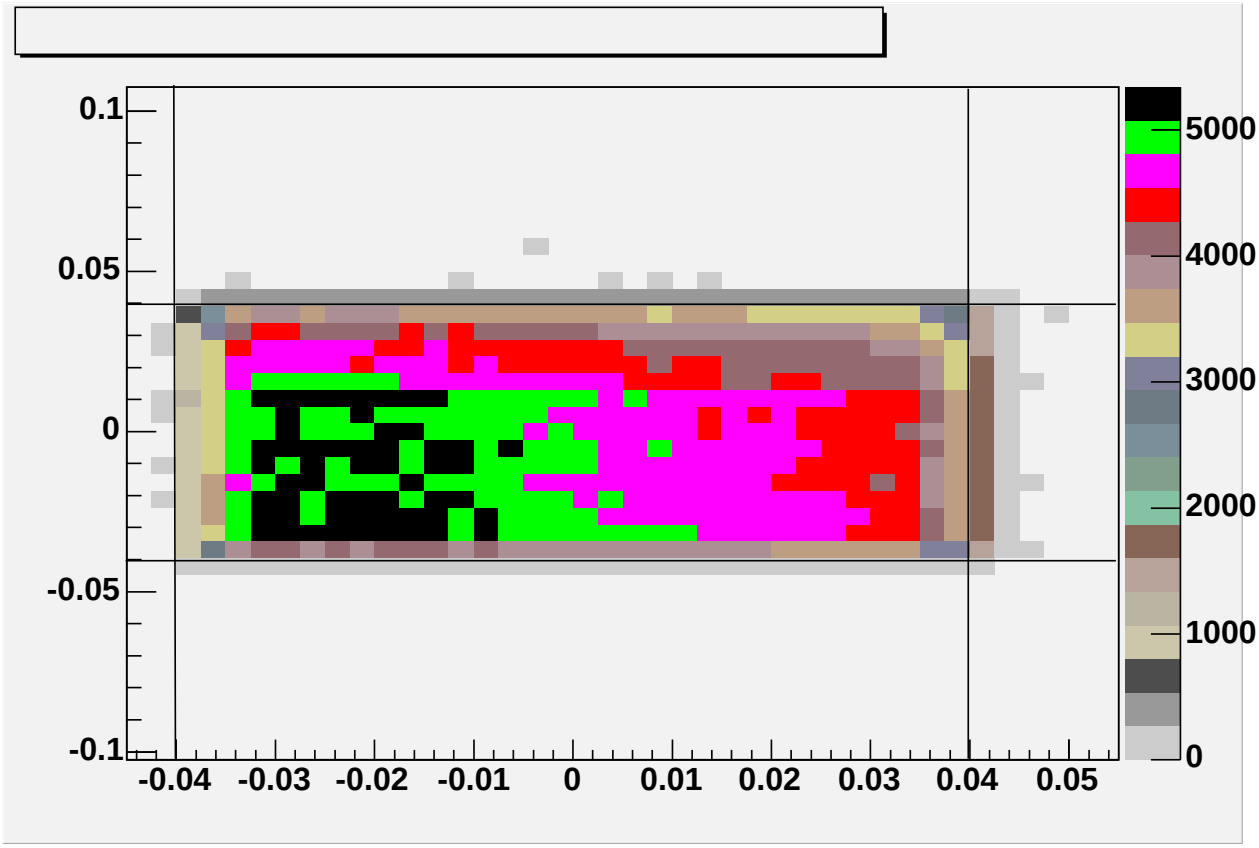

Figure 6.8: The momentum acceptance and the considered full range.

logic pulses passed to the scalers is less than 100 ns, therefore also at the maximum scaler trigger rate for this experiment ($\sim$ 200 kHz for single rate in the electron arm on ^{12}C target) the electronic deadtime can be neglected, while the computer deadtime is consistent, and the typical value for the data taking (determined using a specific class of the Analyzer, THaNormAna) was 14% on ^{12}C target and 8% on ^{9}Be at $\simeq 100\mu A$ of beam current.
This loss of events can be corrected by measuring the trigger input (scaler) and the trigger output (trigger).
For the scaler (S), a coincidence event (S_5) is also recorded as two single arm events (S_1 for the electron arm and S_3 for the hadron arm). Therefore, S_5 is included within S_1 and S_3. For the trigger output (T), a coincidence trigger (T_5) is not recorded as two single arm events (T_1 for the electron arm, T_3 for the hadron arm). Thus T_1, T_3, and T_5 are exclusive.
With the deadtime correction taken into account, the total number of single arm (e, e') events $N_{total}^{(e,e')}$ is given by

$$N_{total}^{(e,e')} = \frac{S_1 - S_5}{T_1} N_1^{(e,e')} + \frac{S5}{T5} N_5^{(e,e')} \tag{6.7}$$

where $N_1^{(e,e')}$ is the number of (e, e') events written to disk as event type 1, and $N_5^{(e,e')}$ is the number of (e, e') events written to disk as event type 5. Similarly, the total

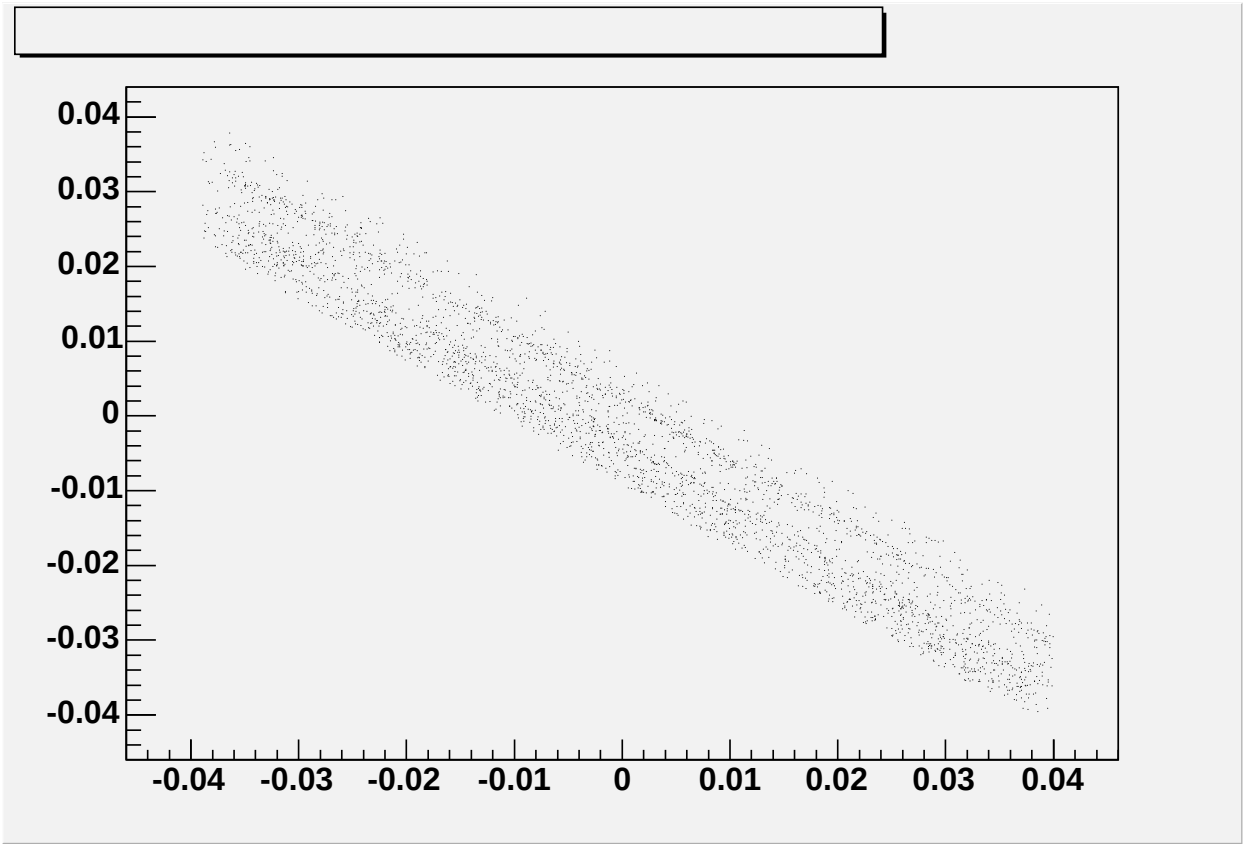

Figure 6.9: The distribution of the detected kaon momentum as function of the detected electron momentum selecting the hypernuclear states.

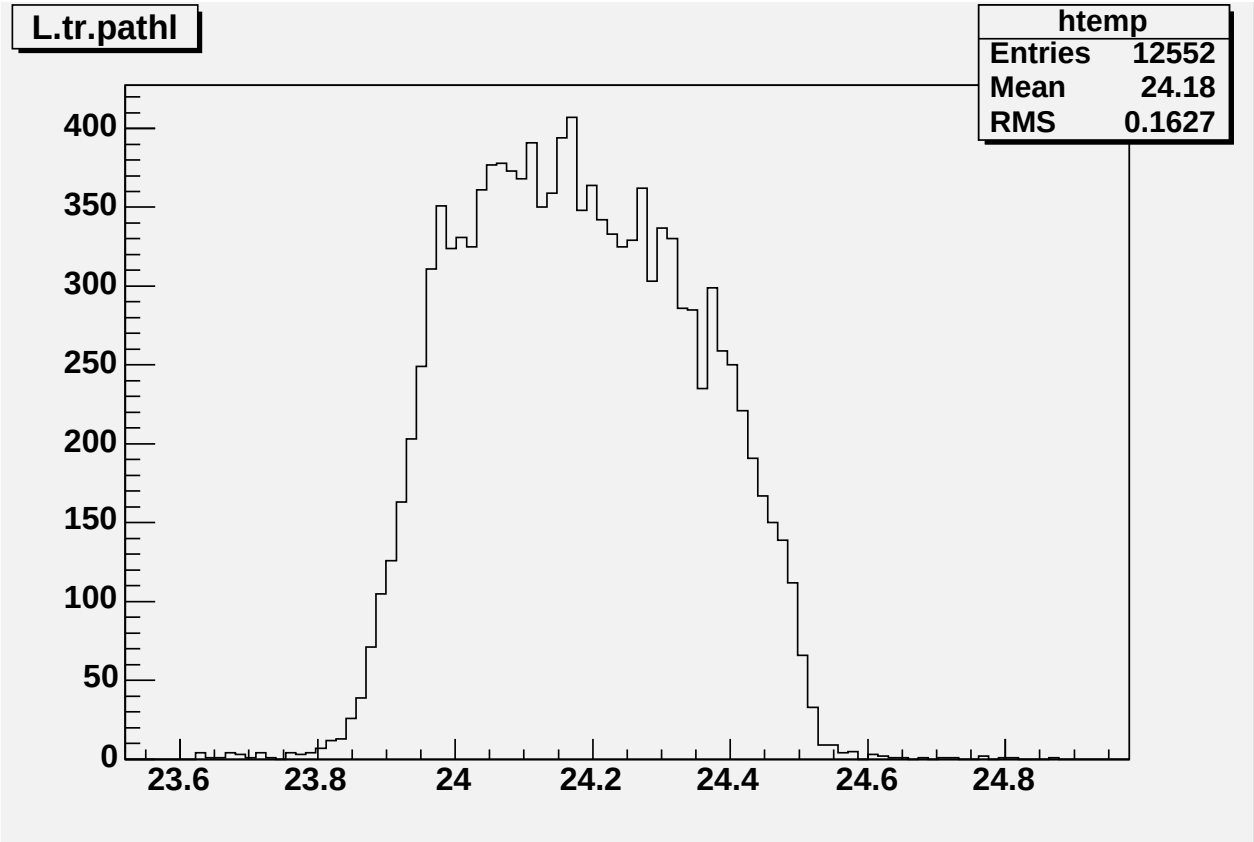

Figure 6.10: The distribution of the path length (m) in the hadron arm.

number of hadron single arm (e,h) (with $h = p, \pi^+, k^+$) event $N_{total}^{(e,h)}$ is

$$N_{total}^{(e,h)} = \frac{S_3 - S_5}{T_3} N_3^{(e,h)} + \frac{S5}{T5} N_5^{(e,h)} \tag{6.8}$$

where $N_3^{(e,h)}$ is the number of (e,h) events written to disk as event type 3, and $N_5^{(e,h)}$ is the number of (e,h) events written to disk as event type 5. For coincidence events, the deadtime correction is different. The total number of coincidence $(e,e'h)$ events after the deadtime correction is

$$N_{total}^{(e,e'h)} = \frac{S_5}{T_5} N_5^{(e,e'h)} \tag{6.9}$$

where $N_5^{(e,e'h)}$ is the number of $(e,e'h)$ events written on disk as event type 5.
Since the prescale factor (p_5) for T_5 was always set at unity, the contribution to the deadtime correction for T_5 is

$$dt5 = \dot{T}_1 \Delta t_1 + \dot{T}_3 \Delta t_3 + \dot{T}_5 \Delta t_5 \tag{6.10}$$

where Δt_3 is the time duration needed for the computer to process a T_3 event, and $\dot{T}_3$ is the rate for T_3. By combining the previous two equations and noting that S_3 is much larger than S_5, it possible to get

$$dt5 = 1 - \frac{p_3 T_3}{S_3 - S_5} + \dot{T}_3 \Delta t_3 \approx 1 - \frac{p_3 T_3}{S_3} + \dot{T}_3 \Delta t_3. \tag{6.11}$$

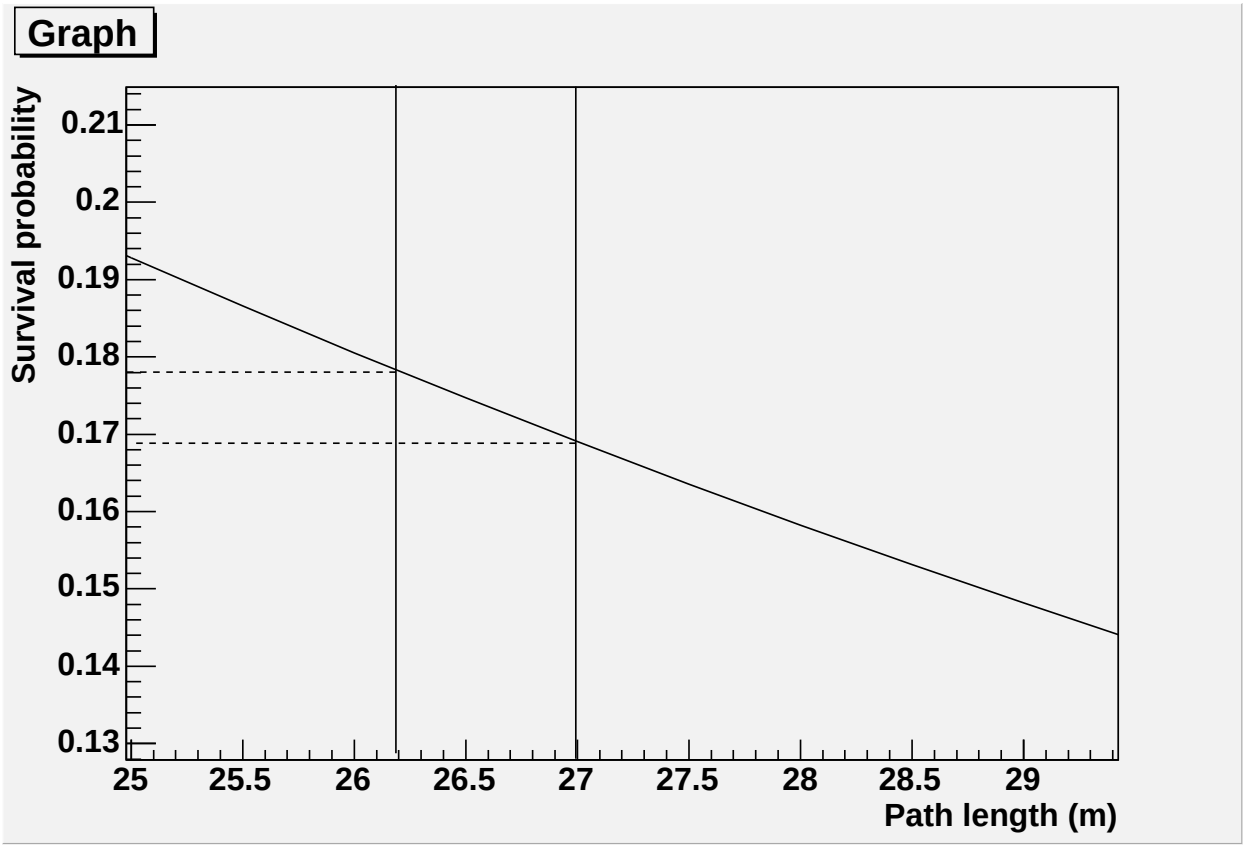

Figure 6.11: The kaon survival probability for $p_k = 1.96\ GeV/c$ as function of the path length (m).

Thus, the deadtime correction for coincidence events is

$$1/(1 - dt5) = 1/(\frac{p_3 T_3}{S_3} - \dot{T}_3 \Delta t_3). \tag{6.12}$$

The average correction factor is 1.21 for $^{12}C(e, e'K^+)^{12}B_\Lambda$ production and 1.10 for $^9Be(e, e'K^+)^9Li_\Lambda$ production.

6.4.4 Kaon detection Efficiency on aerogel and RICH detectors

We evaluate the efficiency of the counter detectors basing on the poissonian distribution, The efficiency for more than one p.e. detection is $\varepsilon = 1 - e^{-N_{p.e.}}$. As described previously, kaon identification is performed by the coincidence of the veto signal in AERO1, detecting pions, and the signal in AERO2, detecting both pions and kaons. In fig. 6.12 the spectrum of AERO1 is shown. The single photoelectron signal amplitude in ADC channels is $\simeq 92$, the average number of p.e. (for pions) is 4.9, corresponding to $\varepsilon =$ 99.3%.
The fig. 6.13 shows the spectrum of AERO2 when a kaon selection is applied on RICH and Coincidence Time. For AERO2 the single p.e. signal average amplitude is $\simeq 85$ ADC channels, therefore the average number of p.e. is $\simeq 7.2$, giving a kaon detection efficiency of 99.9%.
Since in the analysis the kaon identification is performed using the combined response of both the RICH and the aerogel detectors, we have used a loose kaon RICH selection, in order to avoid large inefficiencies. The event selections have been defined in subsection refrichselect. In this way a global kaon efficiency higher than 90% was obtained on the RICH detector.

6.4.5 Gas Čerenkov detector efficiency

Also in this case a poissonian distribution is assumed. The fig. 6.14 shows the spectrum of the gas Čerenkov detector, the average signal amplitude for a single p.e. is $\simeq 90$ ADC channels, therefore the estimated average number of p.e. for electrons is 9.2, giving an electron detection efficiency of 99.98% This number is in a good agreement with the known performance of the detector previously described in cap 4.

6.4.6 VDC efficiency

The number of track per event during the experiment is $\simeq 1.28$, the most part of the event has one track only. Therefore, even if potentially Analyzer can handle multi-track events, the presented analysis is performed selecting single-track events. In this condition the VDC software inefficiency can be characterized by the fraction of zero-track and multiple-track evets generated by non-cosmic particles.
For the hardware efficiency, at this preliminary stage of the analysis, the efficiency of the VDCs is assumed to be what is monitored using the dedicated macro of Analyzer for the detector check-out [48]. Fig. 6.15 shows the efficiency of the VDCs. The

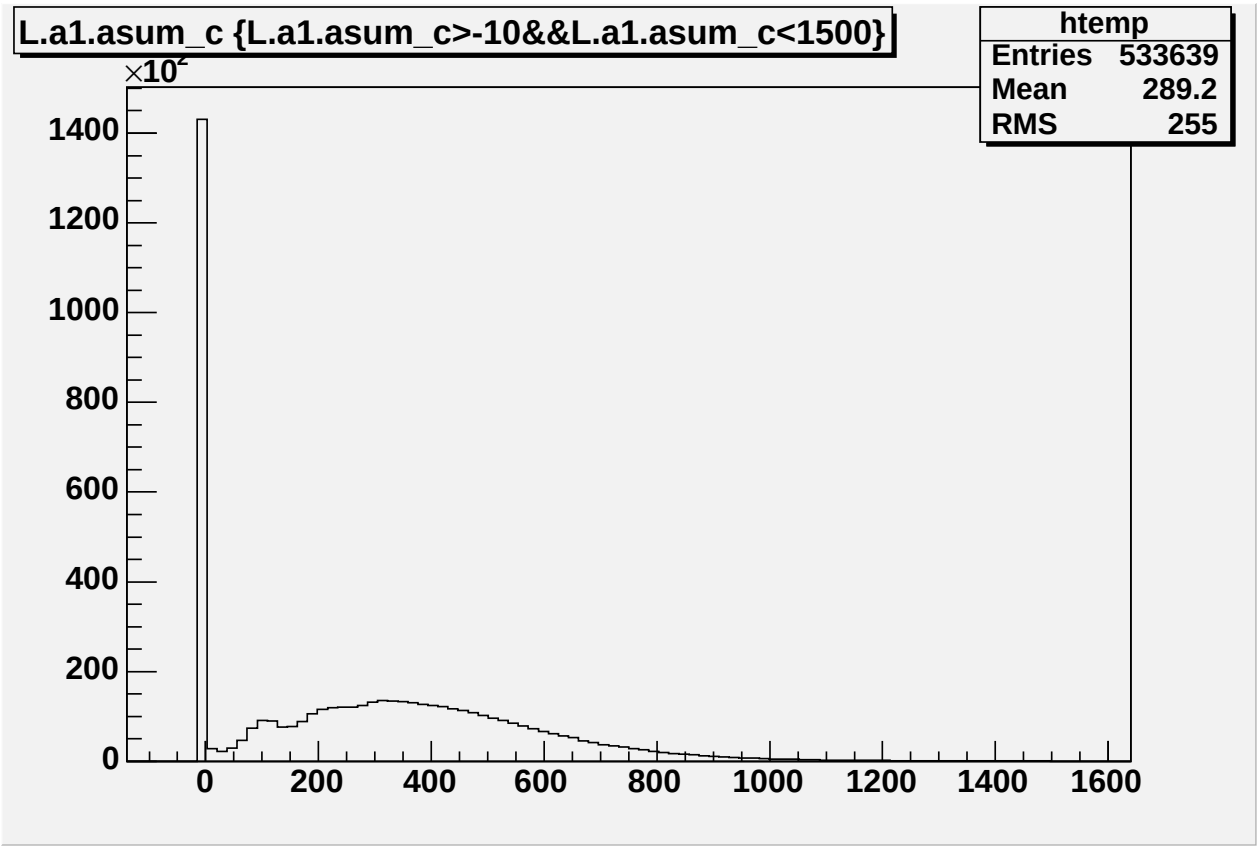

Figure 6.12: The distribution of the pulse height on AERO1.

efficiency is not uniform on all the wires of the detectors, nevertheless the average efficiency is higher than 97% and only few wires in the peripherical zone of the VDCs have efficiency smaller than 90%. An average hardware efficiency of 97% is assumed in this preliminary analysis.

6.4.7 Scintillator/Trigger efficiency

For coincidence events, a trigger is set when the scintillators S1 and S2 fire on both arms.
In principle, it is possible to evaluate the scintillator efficiency using the same criterium than for the other counter detectors, but since these detectors are related to the trigger, a specific system to measure the efficiency is used. This principle is based on the definition of two specific output triggers T_2 (electron arm) and T_4 (hadron arm). A $T_2(T_4)$ trigger is formed if one of the following conditions is satisfied:

- The N_1^{th} paddle of S1 has fired, at the same time the N_2^{th} paddle of S2 has fired, but $N_2^{th} \neq N_1^{th}$ and $N_2^{th} \neq N_1^{th} \pm 1$,

- One paddle of either S1 or S2 has fired, at the same time one PID detector (on the same arm) has fired.

$T_2(T_4)$ events are either cosmic ray events either particles rescattered off the edge of the spectrometer acceptance.

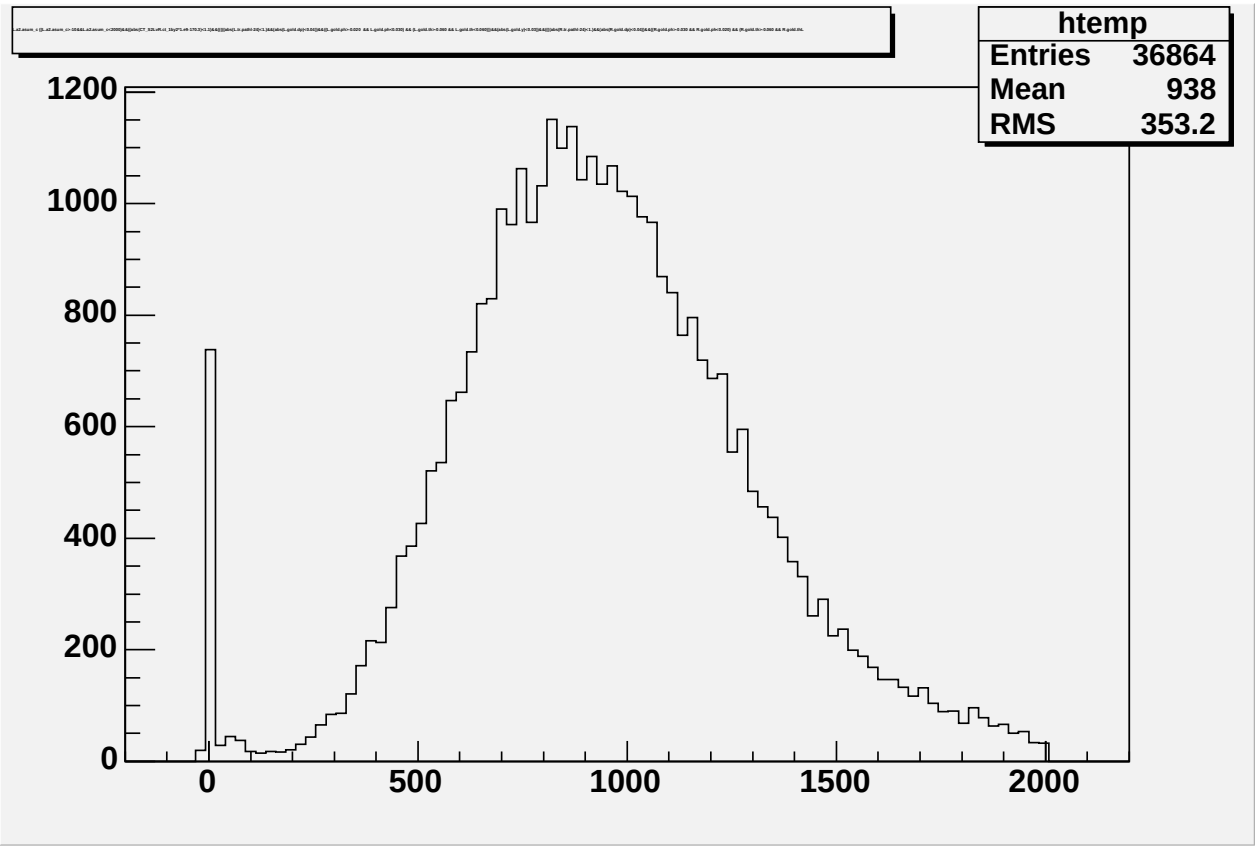

Figure 6.13: The distribution of the pulse height on AERO2 for kaon (from RICH selection).

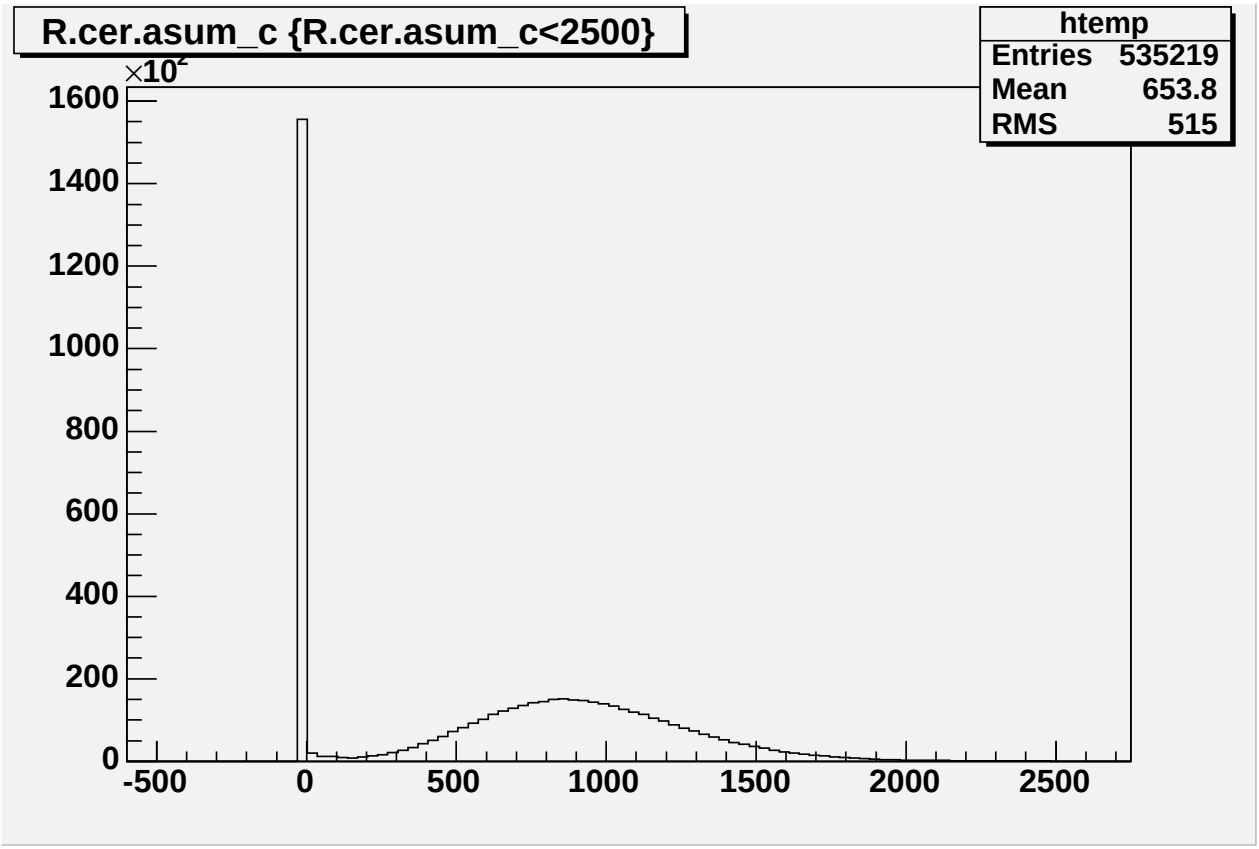

Figure 6.14: The distribution of the pulse height on Gas Čerenkov .

Using these additional triggers, the trigger efficiency is defined as

$$\varepsilon_{trig} = 1 - Inefficiency = \frac{T_{1(3)}}{T_{1(3)} + T_{2(4)}} \tag{6.13}$$

With this method the trigger efficiency for the coincidence events ($T_5 = T_1$ AND T_3) during the experiment can be evaluated as $\simeq 93.5\%$ This value is slightly worst than expected.

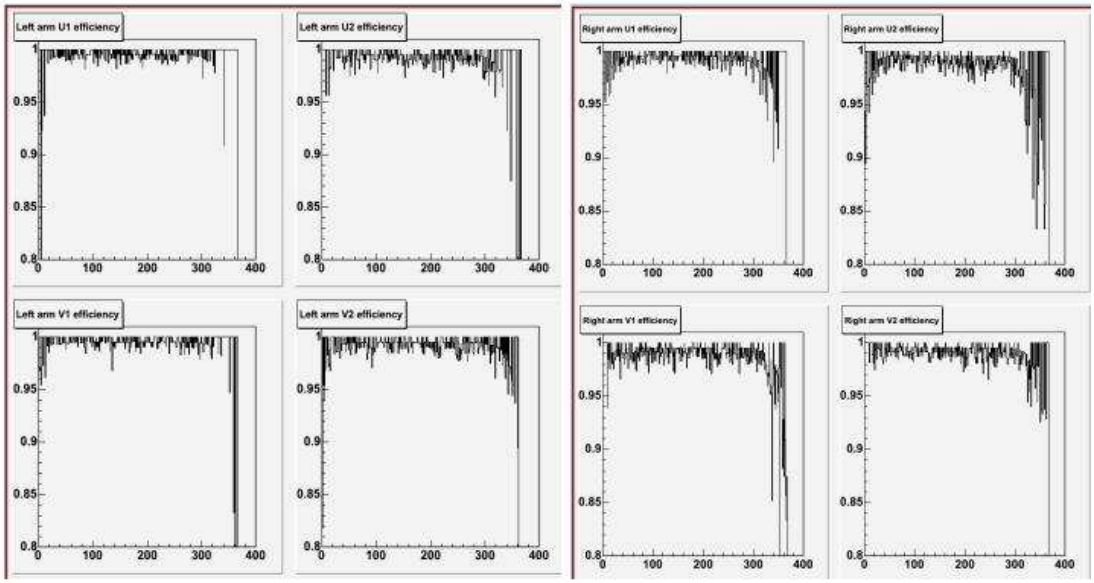

Figure 6.15: The efficiency of the two planes of VDC on the two arms.

Chapter 7

Results and Conclusions

7.1 Results

We describe here the preliminary results of hypernuclear production of $^{12}C(e,e'K^+)^{12}B_\Lambda$ and $^9Be(e,e'K^+)^9Li_\Lambda$.
As previously mentioned, the physics information that can be extracted from the spectra strongly depends on the energy resolution, determined by the beam energy spread (σ_E/E) and by the spectrometer momentum resolution, and on the capability of reducing background with PID. The beam central energy stability has to be monitored in order to correctly compute the missing energy.
The beam 'quality' was not as good as expected ($\sigma_E/E < \ 2.5 \times 10^{-5}$) during the January and part of the April data taking. In January the target was ^{12}C. The beam quality was significantly improved in May, during the $^9Be(e,e'K^+)^9Li_\Lambda$ data taking. One should note also that the optimization of the optics database is not completed yet. The analysis has shown that cuts on momentum acceptance of the spectrometer have to be applied in order to improve the missing energy resolution.

The main results of the analysis are shown in figg. 7.1- 7.10. The missing energy spectra for $^{12}C(e,e'K^+)^{12}B_\Lambda$ and ^9Be have been extracted from the data. Fig. 7.1 and 7.8 show the time of coincidence spectra for $^{12}C(e,e'K^+)^{12}B_\Lambda$ and $^9Be(e,e'K^+)^9Li_\Lambda$ with the kaon selection on aerogel detectors and RICH. Fig. 7.2 and 7.9 show the missing energy spectra with and without RICH cuts. The crucial role of the RICH in 'cleaning' the background is evident. Fig. 7.3 shows two missing energy spectra for $^{12}C(e,e'K^+)^{12}B_\Lambda$. The first spectrum, without any selection on beam or momentum acceptance, shows an energy resolution of $\sim$ 1 MeV (FHWM). Carefully selecting events with good beam energy stability (necessarily reducing statistics) one obtains a missing energy resolution of $\sim$ 550 keV. The statistics drops to $\sim$ 30% of the total, probably insufficient for peak assignments in the core-excited part of the spectrum. Fig. 7.4 shows how the energy resolution improves both selecting events with 'good' beam energy stability and careful cutting the acceptance of the spectrometers.
A missing energy resolution as good as 680 keV can be obtained with 50% of statistics, sufficient for peak identification in the core-excited part of the spectrum.

It has to be emphasized that this is the best resolution ever obtained in the hypernuclear production experiments.

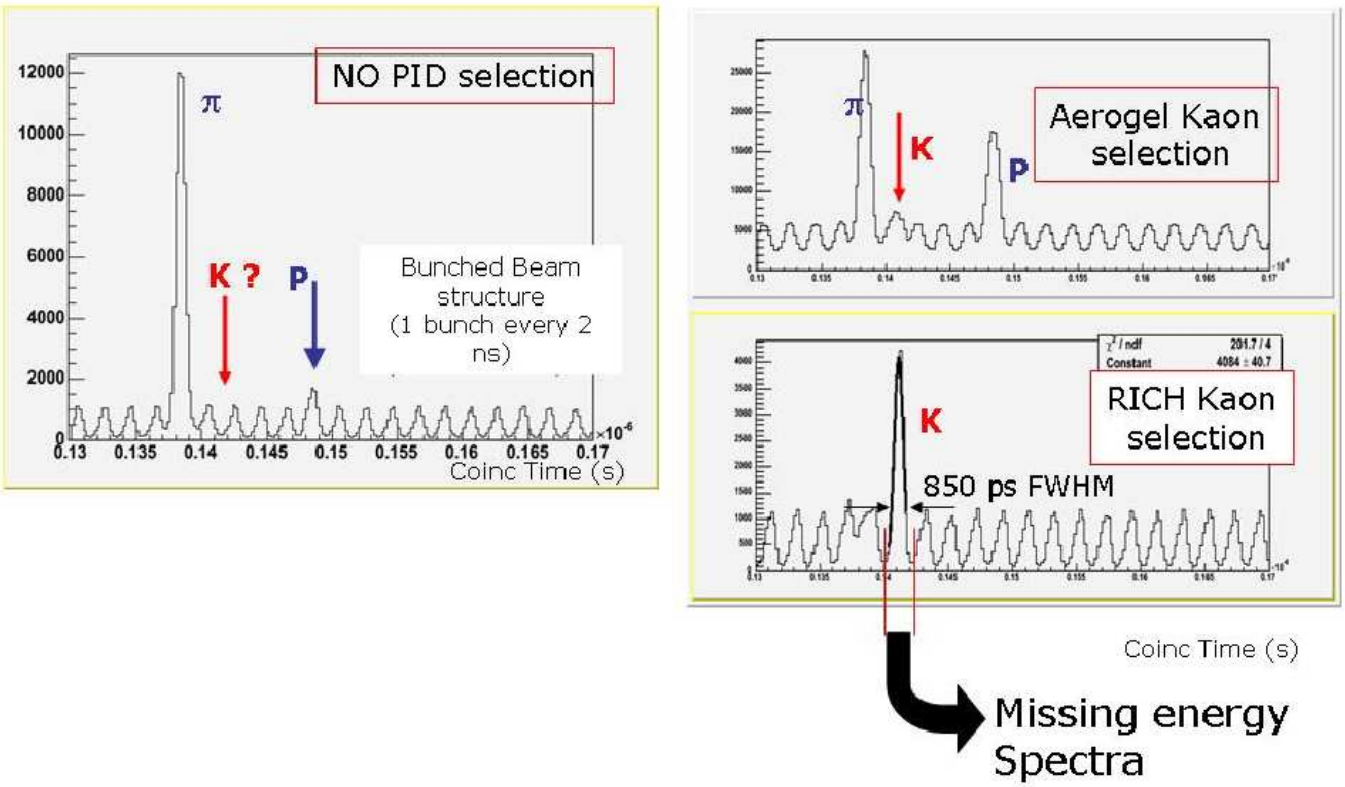

Figure 7.1: The K^+ real-coincidence identification, to select the $^{12}C(e,e'K^+)^{12}B_\Lambda$ reaction.

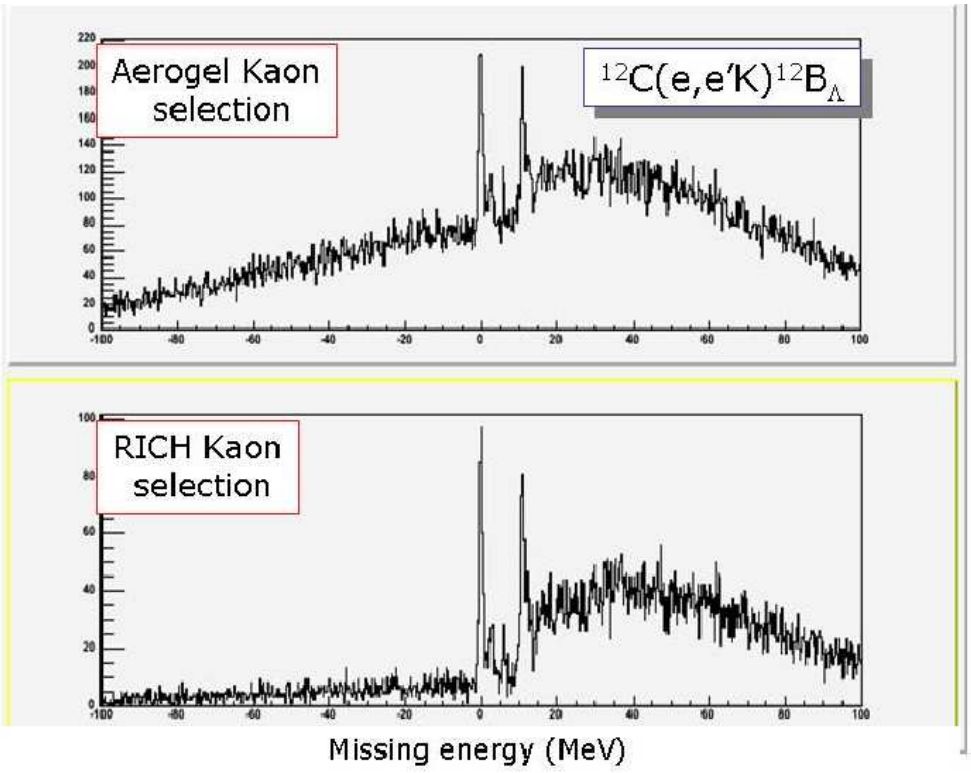

Figure 7.2: $^{12}B_\Lambda$ missing energy spectrum with and without the RICH selection.

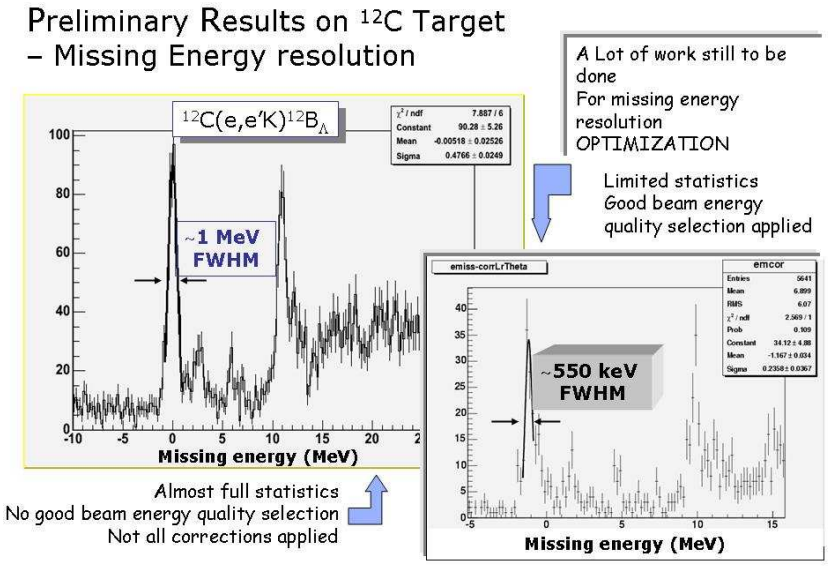

Figure 7.3: The missing energy resolution improvement by selecting events with good beam quality (OTR monitor reporting transverse beam width smaller than 300 μm).

Fig. 7.5 shows a comparison with the results of the experiment E89-009. This experiment took data at Jefferson Lab in Hall C in the spring 2000, using a 2-GeV beam and a dedicated spectrometer allowing a very forward scattering angle for the kaons [52]. Both the experiments show a resolution much better than the best obtained with hadron probes (1.5 MeV FWHM).

Fig. 7.7 shows the preliminary 'physical' analysis of the missing energy spectrum of $^{12}C(e,e'K^+)^{12}B_\Lambda$. The hypernuclear excitations where the reaction replaced a proton by a Λ in the s and p shell give a clear information about the validity of the models. The strength in the bound-state region is also evident.

To evaluate if the peaks in the core-excited region are out of the background, we calculate the Signal-to-Noise-Ratio (SNR) defined as:

$$SNR = \sum_i \frac{s_i}{\sqrt{\sum_i c_i}} = \frac{\sum_i c_i - b_i}{\sqrt{\sum_i c_i}} \tag{7.1}$$

where:

- c_i is the number of counts for the considered bin,
- b_i is the number of background counts for the considered bin,
- $s_i = c_i - b_i$ is the number of counts out of the background in the considered beam.

The background is evaluated fitting the 'not-physical' region (negative region of the missing energy spectrum), the sum defining the SNR is extended to the number of bin defined by the maximization of the SNR. The resulting values of the SNR for the two

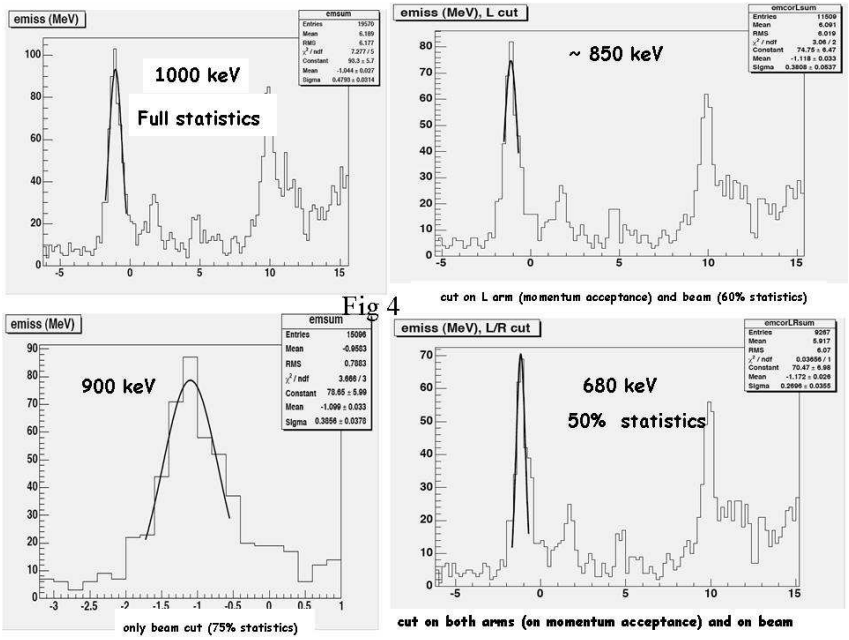

Figure 7.4: $^{12}B_\Lambda$ missing energy spectrum with different cuts.

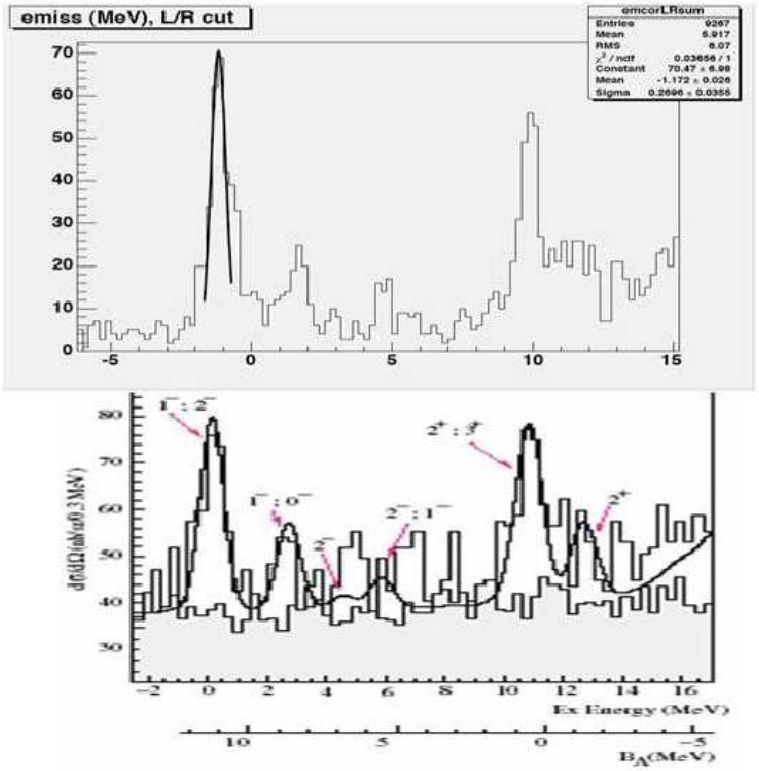

Figure 7.5: Comparison between E94-107 and E89-009 $^{12}B_\Lambda$ spectrum. The E94-107 spectrum (bottom-right on fig. 7.4) has $\simeq$ 300 counts in the ground-state peak, the resolution is $\sim$ 700 keV (FWHM), the E89-009 spectrum has $\simeq$ 165 counts in the ground-state peak, resolution is $\sim$ 900 keV (FWHM).

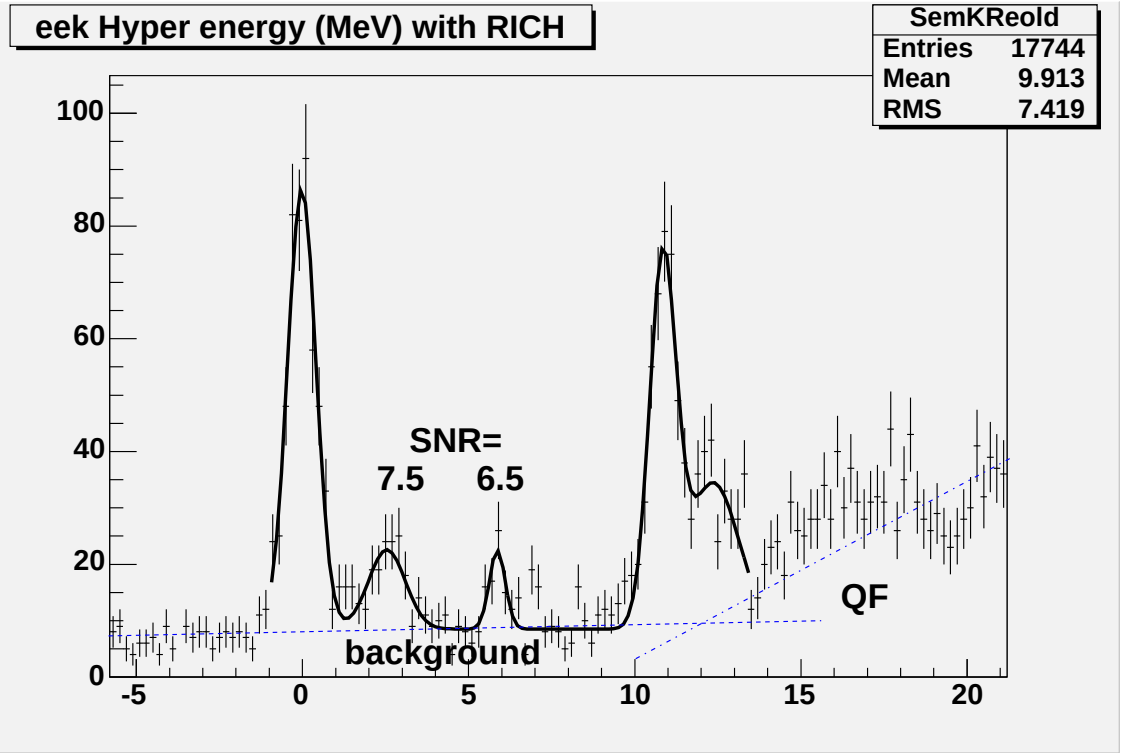

Figure 7.6: The missing energy spectrum for the Carbon target. The presence of a confirmation about the p-shell state and a new information about the core-excited states respect to the literature is clearly shown.

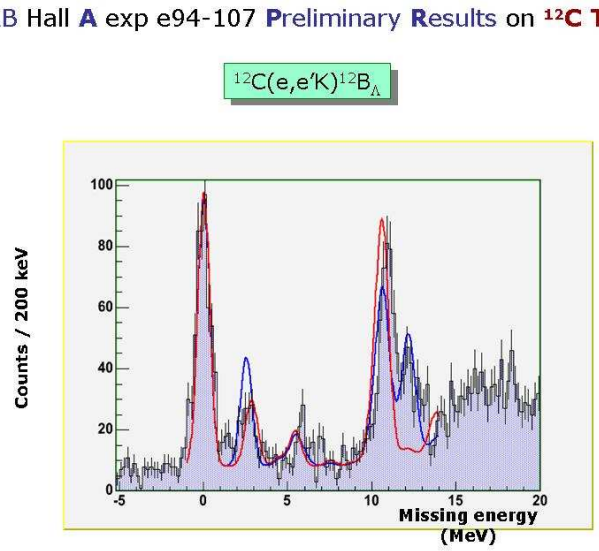

Figure 7.7: $^{12}B_{\Lambda}$ missing energy spectrum, the continuous lines represent the theoretical data (see text description).

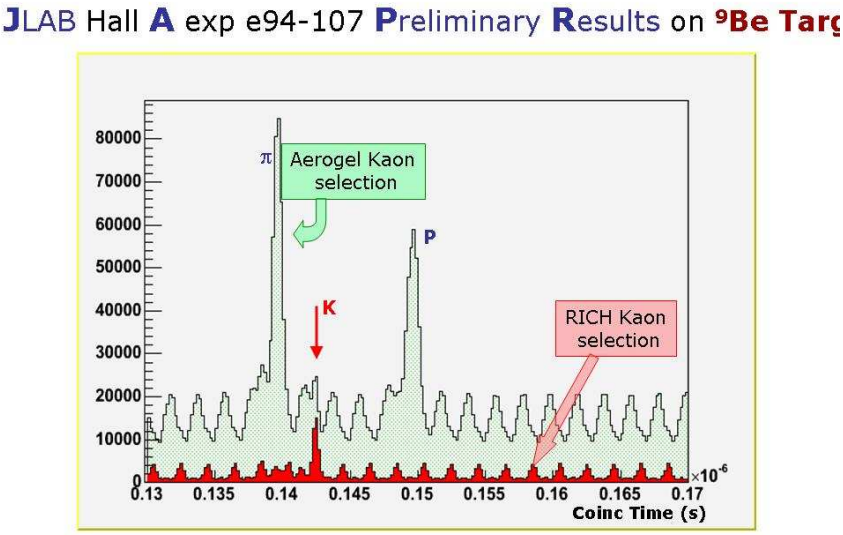

Figure 7.8: Same as Fig. 7.1 for the data on ^9Be.

identified core-excited-state peaks, reported in Fig. 7.6, are $SNR_1 = 7.5$ (at 2.6 MeV) and $SNR_2 = 6.5$ (at 5.4 MeV).
Two theoretical curves have been superimposed on the data (Fig. 7.7), differing by the model used for the elementary $K^+ - \Lambda$ production on protons. The hypernuclear wave function is the same for the two curves as computed by M. Sotona. The red line uses the model of Bennhold-Mart(K-MAID). The blue line the one by Saghai Saclay-Lyon (SLA). Both curves have been normalized to the first (ground state) experimental peak. The relative intensity (with respect to the ground state) of the first excited peak at 2.6 MeV and of the strongly populated $p - \Lambda$ state at 11 MeV seems to be better reproduced by MAID model than the SLA one. Another peak at $6 - 7$ MeV is underestimated by both models.

Following the procedure described in the chapt. 6 a first evaluation of the cross section has been extracted from the data. Considering for example the ground state of the $^{12}C(e, e'K^+)^{12}B_\Lambda$, the cross section is smaller than expected: we evaluate

$$\sigma_{g.s.}(^{12}B_\Lambda) = 3.1 \pm 0.2\ (stat) \pm 0.8\ (syst)\ \frac{nb}{(msr)^2 GeV}, \tag{7.2}$$

which should be compared with a prediction of ([37])

$$\sigma_{g.s.} \sim 5.4 \frac{nb}{(msr)^2 GeV}. \tag{7.3}$$

A possible explanation of the difference with the expectation is given by the following:

1. At our kinematics (rather small electron scattering angle) virtual photons are almost "real", so, in first approximation, we can simply look at the process as photo-production by real photons.

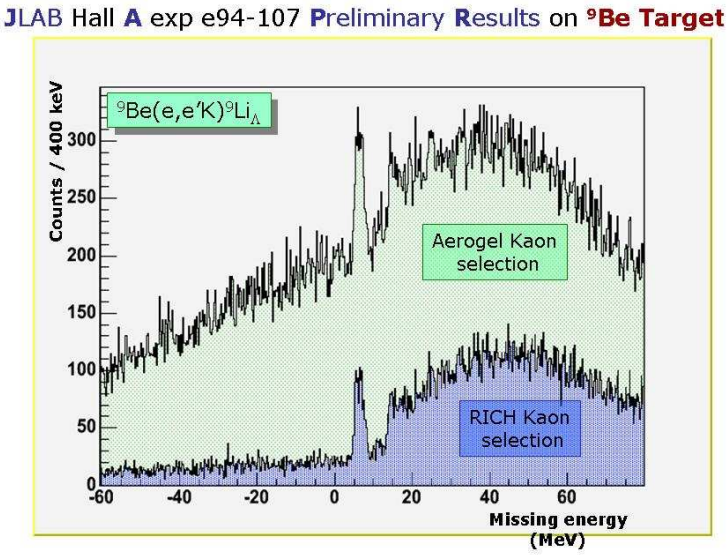

Figure 7.9: Same as Fig. 7.2 for the $^{9}Li_{\Lambda}$.

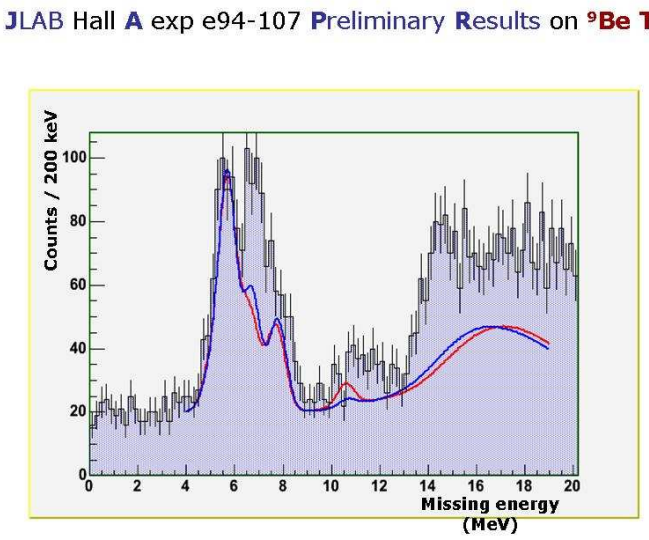

Figure 7.10: Same as Fig. 7.7 for $^{9}Li_{\Lambda}$.

2. Our measurements were done at practically zero kaon scattering angle (with respect to the virtual photon momentum). Our estimates of the hypernuclear cross section were done in DWIA (distorted wave impulse approximation). One can show easily (looking at relevant formulae) that at zero kaon scattering angle the cross section for elementary process and for hypernuclear production are proportional to the same combination of the elementary amplitudes. They differ only by some kinematical factor. For hypernuclear production there is an additional factor that takes into account the many-particle structure of the target nucleus and produced hypernuclear state. Simply speaking, if the elementary cross section at zero kaon scattering angle is small then also all hypernuclear cross section will be small.

3. At the time of the proposal (1994) only the old models of the photo/electroproduction of kaons (such as Adelsek-Bennhold, Adelsek-Saghai, Williams etc) were available. All these models predict almost constant forward cross section up to the photon energy 2.2 GeV. The same is valid for the more modern Saclay-Lyon model. The cross sections (and counting rate) calculation was based on these models. The recent K-MAID model by Bennhold-Mart shows quite different behavior.

Figs. 7.11-7.14 show, for old models AB1 (Adelsek-Bennhold), WJC1 (Williams-Ji-Cotanch), for SLA (Saclay-Lyon) and for K-MAID (Bennhold-Mart) the cross section of the elementary process compared with very recent data (2004) by SAPHIR and by CLASS collaborations. At small photon energy (1.425 GeV) forward cross section (that is $cos\ \theta \simeq 1$) predicted by different models are not too different. However with increasing energy (1.825 GeV, 2.025 GeV, 2.225 GeV) forward cross sections predicted by old models and by Saclay-Lyon are very similar and almost constant ($\approx 0.4 mkb/sr$) but the K-MAID model predicts a forward "dip" and this "dip" is more and more pronounced as photon energy increases. At photon energy 1.825 GeV the forward K-MAID cross section is suppressed (in comparison with other models) by a factor 3, at 2.025 this is a factor approx. 10 and at approx, our energy 2.225 GeV this is even more.

The forward K-MAID cross section for energies approaching the experimental kinematics is significantly suppressed respect to the other models, up to a factor of four. Nevertheless, at the moment it is hard to select the "best" model. In fact:

(i) there is some discrepancy between CLAS and SAPHIR data, especially just at forward kaon angles,

(ii) CLAS collaboration was not able to take data at small Kaon angles.

Nevertheless, one should note that if the predictions of the K-MAID model are correct then hypernuclear production at virtual photon energy of the order 2 GeV is suppressed.

The analysis and the interpretation of the measured missing mass spectra is still at a preliminary stage and not ready for final conclusions. Fig. 7.10 shows the missing energy spectrum of $^9Be(e,e'K^+)^9Li_\Lambda$. Also here the red line uses the model by Bennhold-Mart (K-MAID) for the elementary $K^+ - \Lambda$ production on protons and the blue line the Sagay Saclay-Lyon (SLA) model. Both curves have been normalized to the first experimental peak.

It has been previuosly mentioned that during the $^9Be(e,e'K^+)^9Li_\Lambda$ data taking rastered beam was used. The raster correction has still to be properly applied (chapt. 6). The

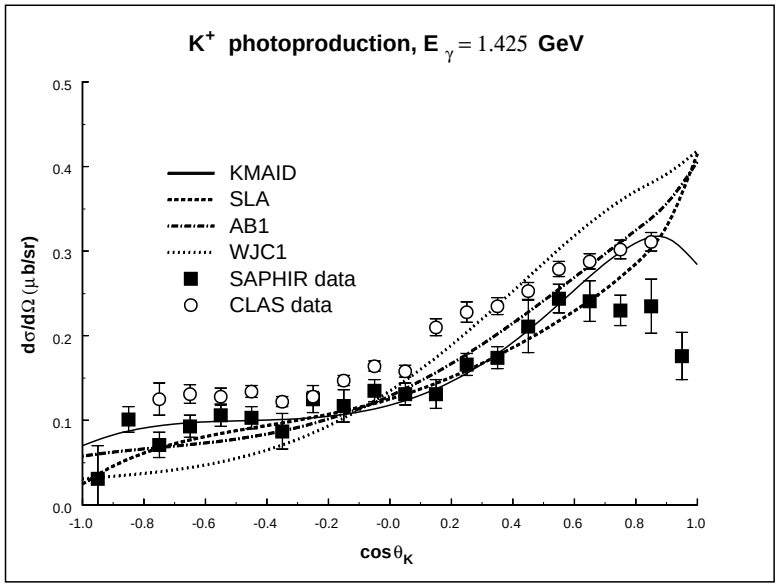

Figure 7.11: Data from photoproduction at 1.425 GeV.

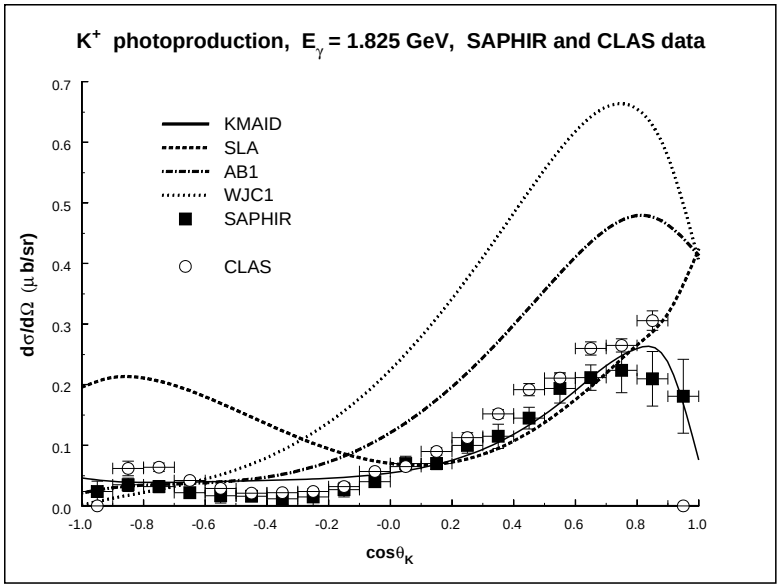

Figure 7.12: Data from photoproduction at 1.825 GeV.

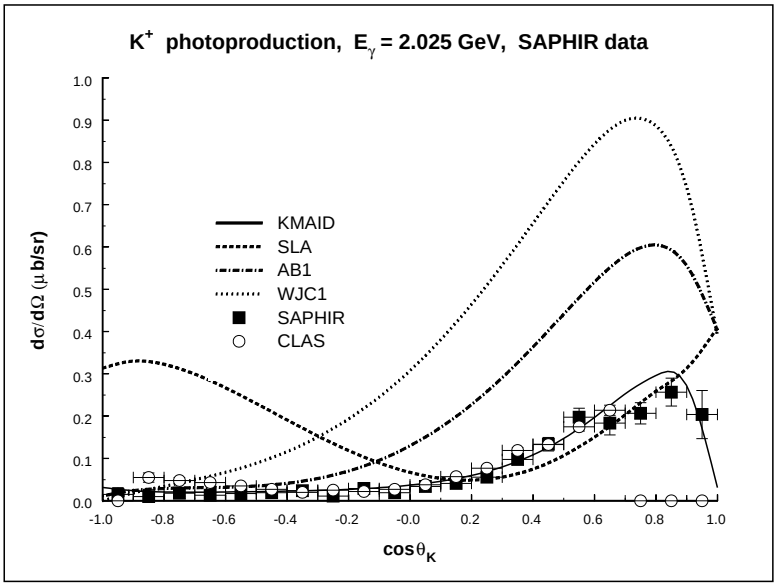

Figure 7.13: Data from photoproduction at 2.025 GeV.

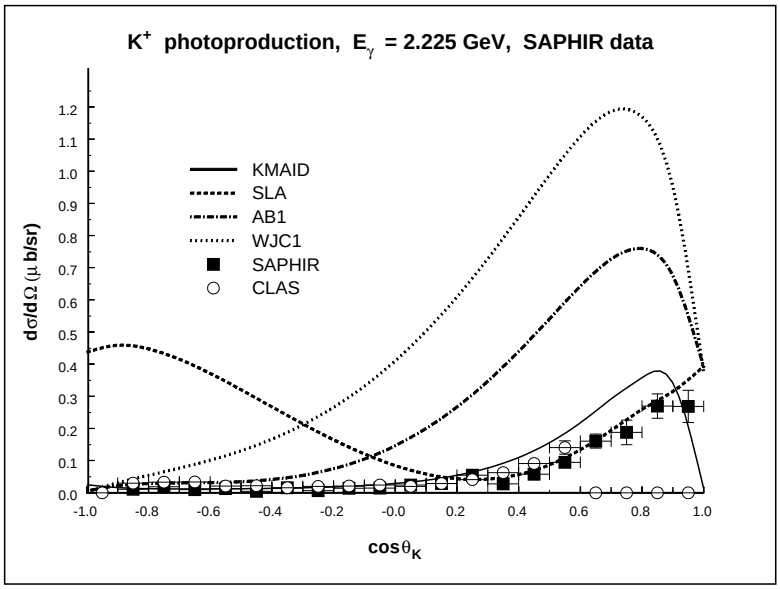

Figure 7.14: Data from photoproduction at 2.225 GeV.

analysis is still very preliminary.

7.2 Conclusion

The experiment E94-107 at Jefferson Lab, Hall A, is designed to perform hypernuclear spectroscopy of light hypernuclei. Data on ^{12}C and ^{9}Be targets have been taken from January to May 2004. The new experimental devices (septum magnets and RICH detector) have proven to be very effective. The RICH detector provided excellent kaon identification and a clean kaon signal over a large pion and proton background. The energy resolution is the best obtained so far for hypernuclear production experiments. Further work is needed to attain a missing energy resolution of the order of $\sim$ 500 keV or less. The optics database optimization is not yet completed. Moreover the optimization of event selection for the beam energy stability, as well as the acceptance cuts, requires further work. Finally, there will be the chance to take further data on a new target (^{16}O) and to increase the statistics on ^{9}Be and if need on ^{12}C during the June-2005 run.
The first 'systematic' study of $1p$ shell hypernuclei with electromagnetic probe has started.

Chapter 8

Appendix A: Short Overview of Hall A Coordinate System

only a short overview of the Hall A coordinate systems is presented here. A detailed description could be found in [45].
All coordinate systems presented are Cartesian.

- Hall Coordinate System (HCS): The origin of the HCS is at the center of the hall, which is defined by the intersection of the electron beam and the vertical symmetry axis of the target system. $\overrightarrow{z}$ is along the beam line and points in the direction of the beam dump, and $\overrightarrow{y}$ is vertically up.

- Target Coordinate System (TCS): Each of the two spectrometers has its own TCS. A line perpendicular to the sieve slit surface of the spectrometer and going through the midpoint of the central sieve slit hole defines the z axis of the TCS for a given spectrometer. $\overrightarrow{z_{tg}}$ points away from the target. In the ideal case where the spectrometer is pointing directly at the hall center and the sieve slit is perfectly centered on the spectrometer, the z_{tg} axis passes through the hall center. For this case, the distance from the hall center to the midpoint of the central sieve slit hole is defined to be the constant Z_0 for the spectrometer. The origin of the TCS is defined to be the point on the z_{tg} axis at a distance Z_0 from the sieve surface (described in the following). In the ideal case, the origin of the TCS coincides with the hall center. The x_{tg} axis is parallel to the sieve slit surface with xtg pointing vertically down. The out-of-plane angle (θ_{tg}) and the in-plane angle (ϕ_{tg}) are given by dx_{tg}/Z_0 and dy_{tg}/Z_0 respectively.

- Detector Coordinate System (DCS): The intersection of wire 184 of the VDC1 U1 plane and the perpendicular projection of wire 184 in the VDC1 V1 plane onto the VDC1 U1 plane defines the origin of the DCS. $\overrightarrow{y}$ is parallel to the short symmetry axis of the lower VDC, $\overrightarrow{z}$ is perpendicular to the VDC U1 plane pointing vertically up, and $\overrightarrow{x}$ is along the other symmetry axis of the lower VDC pointing away from the center of curvature of the dipole.

- Transport Coordinate System (TRCS) at the focal plane: The TRCS at the focal plane is generated by rotating the DCS clockwise around its y-axis by 45°. Ideally, the $\overrightarrow{z}$ of the TRCS coincides with the central ray of the spectrometer.

- Focal plane Coordinate System (FCS): The focal plane coordinate system chosen for the HRS analysis is a rotated coordinate system. This coordinate system is obtained by rotating the DCS around its y-axis by an angle ρ, where ρ is the angle between the local central ray and the $\overrightarrow{z}$ axis of the DCS. As a result, the $\overrightarrow{z}$ axis of the FCS rotates as a function of the relative momentum $\Delta p/p$. In this rotated coordinate system the dispersive angle θ is small for all points across the focal plane. As a result, the expressions for the reconstructed vertex converge faster during optics calibrations.

Chapter 9

Appendix B: Layout and Optics for the Septum Magnets

only a short overview is presented here. All coordinate systems presented are Cartesian.

- Hall Coordinate System (HCS): The origin of the HCS is at the center of the hall, which is defined by the intersection of the electron beam and the vertical symmetry axis of the target system. $\overrightarrow{z}$ is along the beam line and points in the direction of the beam dump, and $\overrightarrow{y}$ is vertically up.

- Target Coordinate System (TCS): Each of the two spectrometers has its own TCS. A line perpendicular to the sieve slit surface of the spectrometer and going through the midpoint of the central sieve slit hole defines the z axis of the TCS for a given spectrometer. $\overrightarrow{z_{tg}}$ points away from the target. In the ideal case where the spectrometer is pointing directly at the hall center and the sieve slit is perfectly centered on the spectrometer, the z_{tg} axis passes through the hall center. For this case, the distance from the hall center to the midpoint of the central sieve slit hole is defined to be the constant Z_0 for the spectrometer. The origin of the TCS is defined to be the point on the z_{tg} axis at a distance Z_0 from the sieve surface (described in the following). In the ideal case, the origin of the TCS coincides with the hall center. The x_{tg} axis is parallel to the sieve slit surface with xtg pointing vertically down. The out-of-plane angle (θ_{tg}) and the in-plane angle (ϕ_{tg}) are given by dx_{tg}/Z_0 and dy_{tg}/Z_0 respectively.

- Detector Coordinate System (DCS): The intersection of wire 184 of the VDC1 U1 plane and the perpendicular projection of wire 184 in the VDC1 V1 plane onto the VDC1 U1 plane defines the origin of the DCS. $\overrightarrow{y}$ is parallel to the short symmetry axis of the lower VDC, $\overrightarrow{z}$ is perpendicular to the VDC U1 plane pointing vertically up, and $\overrightarrow{x}$ is along the other symmetry axis of the lower VDC pointing away from the center of curvature of the dipole.

- Transport Coordinate System (TRCS) at the focal plane: The TRCS at the focal plane is generated by rotating the DCS clockwise around its y-axis by 45°.

Ideally, the $\overrightarrow{z}$ of the TRCS coincides with the central ray of the spectrometer.

- Focal plane Coordinate System (FCS): The focal plane coordinate system chosen for the HRS analysis is a rotated coordinate system. This coordinate system is obtained by rotating the DCS around its y-axis by an angle ρ, where ρ is the angle between the local central ray and the $\overrightarrow{z}$ axis of the DCS. As a result, the $\overrightarrow{z}$ axis of the FCS rotates as a function of the relative momentum $\Delta p/p$. In this rotated coordinate system the dispersive angle θ is small for all points across the focal plane. As a result, the expressions for the reconstructed vertex converge faster during optics calibrations.

Chapter 10

Appendix C: RICH analysis procedure

We describe here the procedure used for the analysis of the RICH data. The first step of the analysis is to identify the clusters in the RICH pad plane. A cluster is defined as a 'spot' made up by contiguous pads fired in the cathode planes (a cluster can include only one pad or several ones). In this first step, is assumed that, without any noise, each cluster but one corresponds to a photon generated in the radiator by the particle crossing the RICH (in the following, unless otherwise specified we will use the terms "cluster" and "photon" as synonyms, despite their great conceptual difference). The exception is the cluster that is generated by the particle itself. This cluster (in the following the 'MIP') has typically the biggest side and the biggest charge, since the charge ionized from the MIP in the gap of the MWPC is $\approx 20\ e^-$.
The positions of the points where the photons and the particle hit the pad plane are identified by the center of gravity of the charge making up the cluster. That is:

$$X(Y)_{clus} = \frac{\sum_i x(y)_i \times Q_i}{\sum_i Q_i} \tag{10.1}$$

where x_i, y_i is the pad position and Q_i the charge collected on the pad.
The MIP is identified calculating the interception point between the particle track and the RICH pad plane. The maximum charge cluster inside a defined radius R around this point is assumed to be the MIP. The length of R is a free parameter in the RICH database used by ROOT/C++ Analyzer (parameter "maxdist" in the RICH database). It is possible, changing the parameter "MIP through interception" in the RICH database, to "force" the MIP to be just in the position the particle track hits the RICH pad plane. According to the value of MIP through interception parameter, this option can be applied for every event, only for events in which no cluster is found inside the radius R or just for the events the particle track hits the RICH in a no sensible zone. Because the failure of the MIP search around the expected point is usually connected with a not negligible multiple scattering of the particle to be identified, all the options quoted above must be handled with care, due to the uncertainties on particle entrance angles in the RICH that occur in these cases. It could happen that one or more clusters are not generated either by a photon or by the particle but are "noise". The RICH

particle identification algorithm will try to get rid of these not desired clusters.
In the second step of the analysis the clusters are "resolved", to identify in a single cluster the presence of more photons that (partially) overlap. If the number of occurrences of these "not elementary" clusters is high, the algorithm of identification of the particle could be affected by a not negligible error. For this reason all the not elementary clusters are split ("resolved") into the original clusters whose overlapping has made them up.
Usually a not elementary cluster can be identified because it has a charge distribution with several relative maximums. The number of the maximums is equal to the number of the original clusters.
There are different methods to resolve clusters. Some of them are relatively simple. The method used presently in the RICH algorithm, for example, assigns to each elementary cluster, that make up a not resolved one, a charge proportional to the charge of the corresponding relative maximum. (the algorithm is actually slightly more complicated and will be described in more detail elsewhere). Other resolving cluster methods could be pretty sophisticated (for example the Mathieuson algorithm). The resolving cluster algorithm presently in Analyzer will be eventually improved. In any case its modification is not expected to vary substantially the result, due to the low cluster density in the pad plane and the consequent low number of overlapping clusters.
After the resolving algorithm has been applied a new set of cluster arouses. This set is made up by the clusters created by resolving not elementary clusters plus those clusters that did not need any resolving algorithm because generated only by one photon. We call this set as "resolved clusters".
Each variables concerning the "resolved clusters" are called in the Analyzer Tree as: L.rich.rclus.VariableName. For instance: L.rich.rclus.chrg (the total charge of the resolved cluster); L.rich.rclus.x and L.rich.rclus.y (the x and y coordinates of the resolved cluster). For the on-line analysis, the resolving algorithm resulted too time consuming considering the PID efficiency improvements it gives, therefore a flag in the Analyzer RICH module database was used to give the possibility to switch the resolving cluster algorithm off (option do resolve = 0 in db L.rich.dat).
Knowing the relative position of the clusters (including the MIP) in the RICH pad plane and the direction of the particle track with respect to the normal to the RICH (given by Analyzer track reconstruction algorithm angles θ and ϕ [variables L.rich.mip.theta and L.rich.mip.phi respectively]), one can get, for each cluster, the Čerenkov emission angle of the corresponding photon. The algorithm, based on a geometrical back-tracing, was briefly described in 5.2.1, a well-detailed description is in [46]. The variables L.rich.clus.theta and L.rich.clus.phi (L.rich.rclus.theta and L.rich.rclus.phi for the resolved clusters) are the photon polar angles used in the algorithm.
The Čerenkov angle for the single photons calculated in this way are stored in the variables L.rich.clus.angle (L.rich.rclus.angle for resolved photon). Ideally, all the Čerenkov angles should be equal (we are dealing with events with only one particle). The uncertainty on the position of the photon emission point in the radiator, the error in the calculation of the distance "Photon Cluster MIP Cluster" and the fact that the Čerenkov photons are not monocromathic, however, cause the Čerenkov photon angles to be spread around the expected value according a gaussian distribution. As already

mentioned before 5.2.1, expected values are about (the exact value depending on the momentum of the particle to be identified): 0.55 rad for protons. 0.65 rad for kaons. 0.68 rad for pions.
Also looking at the single-photon distribution, two peaks would be clearly distinguishable: one is relative to the photons generated by the pions and the other to the photons generated by the protons. The kaon peak is instead hidden under the pion one due to the angular resolution of the RICH, (that is the resolutions of the distribution of the single Čerenkov photon angles around the expected values) and to the fact the number of kaons is much smaller than the number of pions for the hypernuclear spectra experiment. The two visible peaks (as the hidden kaon peak) can be fitted with gaussians. The photons not belonging to the peaks are of course noise.
The standard method calculates, for each event, the averages of the single Čerenkov photon angles inside three "fiducial zones". The fiducial zones are defined as:

$$\theta_{p/k/\pi} - L < \theta_{clus} < \theta_{p/k/\pi} + L \tag{10.2}$$

where:

- $\theta_{p/k/\pi}$ are the expected Čerenkov angles (one for each hypothesis on the particle),

- θ_{clus} ia the measured Čerenkov angle for the considered cluster,

- L is a free parameter, defining the amplitude of the fiducial zones.

Although L is usually set equal to 3 σ_θ, with σ_θ the standard deviation, experimentally determined by fits, of the single photon distribution around the expected values, no restriction at all is made on its value.
If σ_θ is the standard deviation of the single photon distribution around the expected value, the standard deviation of the distribution of the averages is $\sigma/\sqrt{N}$, where N is the average number of Čerenkov p.e. in one event. In this way the mean Čerenkov angle distribution should clearly show up three peaks corresponding to the three kind of particles (Fig. 5.21).
Before proceeding in this way, however, we prefer to make some confidence test on the hypothesis on the particle to be identified. Because the single photon angles are, in absence of noise, distributed in a gaussian way around the expected value, the sum:

$$\sum_i \frac{(\theta_i - \theta_{p/k/\pi})^2}{\sigma^2} \tag{10.3}$$

where

- θ_i is the single photon Čerenkov angle

- $\theta_{p/k/\pi}$ are the expected Čerenkov angles for the three particles,

- σ is the standard deviation of the single photon distribution,

is expected to follow the χ^2 distribution. The sum 10.3 is extended to the OR of the three defined fiducial zones. σ is a free parameter, called "cluster distribution sigma" in the Analyzer RICH database. With the 10.3 one tries to analyze the whole single photon distribution and not only its mean as the case of a method simply employing the mean Čerenkov angle. For the same reason, the sum 10.3 is extended to the OR of the three fiducial zones, just not to loose any piece of information "a priori" and to try to select the most likelihood hypothesis on the particle to identify.
Using the 10.3 one obtain three χ^2 values, one for each hypothesis on the particle to identify. Therefore it is possible to evaluate for which hypothesis on the particle the χ^2 value is acceptable. The three values of 10.3 could be affected however by clusters generated by the noise that could make none of them acceptable with a reasonable confidence level. Therefore the combination of the Average Čerenkov angle calculation and the use of Čerenkov detector response in term of χ^2 is used to identify completely the particle. Starting from the single-photon angle distribution, one can try to apply the traditional methods to identify completely the kaons (with the average angle distribution for example). We skip the details because already described in literature [46] and the results are shown in the following.
When the RICH cuts only are applied, a pion contamination exists. This is due to the fact that the number of π^+ is much bigger than the number of the K^+. It could happen consequently that a relatively poor number of pions (but still not negligible when being confronted with the kaon number) produces a photon angle distribution statistically equal with the one produced by kaons. Because the photon angle distributions of these pions are statistically identical to the kaon ones, there is no way to distinguish them with the RICH information only (neither comparing the average angles, that are the averages of two identical distributions, nor checking the number of photons generated, pretty close for pions and kaons).
When considering Čerenkov threshold aerogel counters together with the RICH, however, the pion contamination in the kaon sample disappear below any detectable evidence.

Bibliography

[1] G. D. Rochester and C. C. Butler, Nature, 160 (1947), 855.

[2] R. A. Adelseck and B. Saghai, Phys Rev C 42 (1990), 105.

[3] M. Iodice et al., CEBAF Experimental Proposal PR-98-108 (1998).

[4] J. Adam, J. Mares, O. Richter, M. Sotona and S. Frullani, Czech J Phys 42 (1992), 1167.

[5] S. R. Cotanch and S. S. Hsiao, Nucl Phys A 450 (1986), 419c.

[6] H. Thom, Phys Rev 151 (1966), 1322.

[7]

[8] R. A. Williams, Chueng-Ryong Ji and C. R. Cotanch, Phys Rev D 41 (1990), 1149.

[9] R. A. Williams, Chueng-Ryong Ji and C. R. Cotanch, Phys Rev C 43 (1991), 452.

[10] R. L. Workman, Phys Rev C 44 (1991), 552.

[11] H. Bando, T. Motoba, M. Sotona and J. Zofka, Phys Rev C 39 (1989), 587.

[12] M. Akei et al., Nucl Phys A 534 (1991), 478.

[13] T. Hasegawa et al., Core excited states of 12CΛ hypernuclei formed in the (π^+, K^+) reaction, INS-Rep.-1037 (1994), University of Tokyo.

[14] J. Pniewski et al., Nucl Phys A 443 (1985), 685.

[15] G. M. Urciuoli et al., Nucl Phys A 691 (1-2)(2001), 43-50.

[16] W. Bertozzi et al, Nucl Instr Meth A 191 (1977), p.957.

[17] P. Bydzovsky, nucl-th/0408039.

[18] J. W. Lightbody Jr., J. S. O'Connel, Comp in Physics, May/June 1988, 57.

[19] N. Liyanage, Ph. D. Thesis, Massachusetts Institute of Technology, Cambridge, Massachusetts.

[20] F. Cusanno et al., Nucl Instr Meth A 502 (2003), 251-255.

[21] F. Garibaldi et al., Nucl Instr Meth A 502 (2003), 117-122.

[22] F. Cusanno et al., Nucl Instr Meth A 525 (2004), xxx-xxx.

[23] F. Garibaldi et al., Nucl Instr Meth A 496 (2003), 305-314

[24] K. S. Krane, Introduction to Nuclear Physics, J. Wiley and Sons (1998).

[25] J. Adam et al., J Phys 42 (1962), 1167.

[26] A. G. M. van Hees and P. W. M. Glaudemans, Z Phys A 314 (1983), 323.

[27] A. D. Martin, Nucl Phys B 94 (1975), 413.

[28] R. A. Williams, Chueng-Ryong Ji and C. R. Cotanch, Phys Rev C 46 (1992), 1617.

[29] R. A. Adelseck and L. E. Wright, Phys Rev C38 (1988), 1965.

[30] R. A. Adelseck and B. Saghai, Phys Rev C42 (1990), 108.

[31] H. Bando, T. Motoba and J. Zofka, International Journal of Modern Physics A5 (1990), 4021.

[32] D. J. Millener et al., Phys Rev C31 (1985), 499.

[33] V. N. Fetisov et al., Z Phys A 39 (1991) 399.

[34] Y. Yamamoto and H. Bando, Prog Theor Phys Suppl 81 (1985), 9.

[35] O. Richter, M. Sotona and J. Zofka, Phys Rev C43 (1992), 2753.

[36] R. H. Dalitz and A. Gal, Ann Phys 116 (1978), 167.

[37] F. Garibaldi et al, CEBAF Experimental Proposal PR-94-107, High Resolution Hypernuclear 1p Shell Spectroscopy (1994).

[38] F. Garibaldi et al., Nucl Instr Meth A 314 (1992), p.1.

[39] J. Alcorn et al., Nucl Instr Meth A 522 (2004), p.294-346.

[40] L. Alexa et al., ...

[41] L. Lagamba et al., Nucl Instr Meth A 471 (2001), p.325-332.

[42] R. Perrino et al., Nucl Instr Meth A 457 (2001), p. 571-580.

[43] R. De Leo et al., Nucl Instr Meth A 401 (1997), p. 187-205.

[44] http://root.cern.ch/

[45] Jefferson Lab Hall A ESPACE User Guide, http://wwww.jlab.org/espace/docs.hmtl.

[46] CERN/LHCC 98-19, ALICE TDR 1, 14 August 1998.

[47] S. Marrone, private communication.

[48] http://hallaweb.jlab.org/data_reduc/AnaWork2003/bryan.pdf.

[49] http://hallaweb.jlab.org/equipment/daq/trigger_coinc.html.

[50] Y.-C. Chao et al., http://www1.jlab.org/U1/publications/documents/ACF1B27.pdf.

[51] P. Chevtsov et al., Synchrotron Light Interferometer at Jefferson Lab, Proceeding of the 2003 PAC, http://accelconf.web.cern.ch/accelconf/p03/PAPERS/WPPB068.PDF.

[52] T. Miyoshi et al., Phys Rev Lett 90 (2003), 232502.